



National Library  
of Canada

Acquisitions and  
Bibliographic Services Branch

395 Wellington Street  
Ottawa, Ontario  
K1A 0N4

Bibliothèque nationale  
du Canada

Direction des acquisitions et  
des services bibliographiques

395, rue Wellington  
Ottawa (Ontario)  
K1A 0N4

Trouver - Your reference

Chercher - Your reference

## NOTICE

The quality of this microform is heavily dependent upon the quality of the original thesis submitted for microfilming. Every effort has been made to ensure the highest quality of reproduction possible.

If pages are missing, contact the university which granted the degree.

Some pages may have indistinct print especially if the original pages were typed with a poor typewriter ribbon or if the university sent us an inferior photocopy.

Reproduction in full or in part of this microform is governed by the Canadian Copyright Act, R.S.C. 1970, c. C-30, and subsequent amendments.

## AVIS

La qualité de cette microforme dépend grandement de la qualité de la thèse soumise au microfilmage. Nous avons tout fait pour assurer une qualité supérieure de reproduction.

S'il manque des pages, veuillez communiquer avec l'université qui a conféré le grade.

La qualité d'impression de certaines pages peut laisser à désirer, surtout si les pages originales ont été dactylographiées à l'aide d'un ruban usé ou si l'université nous a fait parvenir une photocopie de qualité inférieure.

La reproduction, même partielle, de cette microforme est soumise à la Loi canadienne sur le droit d'auteur, SRC 1970, c. C-30, et ses amendements subséquents.

University of Alberta

**CLIPPING-INDUCED IMPULSIVE NOISE IN DIRECTLY MODULATED  
FIBER OPTIC CATV TRANSMISSION SYSTEMS**

by

**STEPHEN WILLIAM LAI**



A thesis submitted to the Faculty of Graduate Studies and Research in partial fulfillment of  
the requirements for the degree of **Master of Science**.

Department of Electrical Engineering

Edmonton, Alberta

**SPRING, 1996**



National Library  
of Canada

Acquisitions and  
Bibliographic Services Branch

395 Wellington Street  
Ottawa, Ontario  
K1A 0N4

Bibliothèque nationale  
du Canada

Direction des acquisitions et  
des services bibliographiques

395, rue Wellington  
Ottawa (Ontario)  
K1A 0N4

*Your title - Votre référence n°*

*Your title - Votre référence n°*

**The author has granted an irrevocable non-exclusive licence allowing the National Library of Canada to reproduce, loan, distribute or sell copies of his/her thesis by any means and in any form or format, making this thesis available to interested persons.**

**L'auteur a accordé une licence irrévocable et non exclusive permettant à la Bibliothèque nationale du Canada de reproduire, prêter, distribuer ou vendre des copies de sa thèse de quelque manière et sous quelque forme que ce soit pour mettre des exemplaires de cette thèse à la disposition des personnes intéressées.**

**The author retains ownership of the copyright in his/her thesis. Neither the thesis nor substantial extracts from it may be printed or otherwise reproduced without his/her permission.**

**L'auteur conserve la propriété du droit d'auteur qui protège sa thèse. Ni la thèse ni des extraits substantiels de celle-ci ne doivent être imprimés ou autrement reproduits sans son autorisation.**

ISBN 0-612-10725-6

University Of Alberta

Library Release Form

**Name of Author:** Stephen William Lai

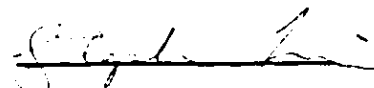
**Title of Thesis:** Clipping-Induced Impulsive Noise in Directly Modulated  
Fiber Optic CATV Transmission Systems

**Degree:** Master of Science

**Year This Degree Granted:** 1996

Permission is hereby granted to the University of Alberta Library to reproduce single copies of this thesis and to lend or sell such copies for private, scholarly or scientific research purposes only.

The author reserves all other publication and other rights in association with the copyright in the thesis, and except as hereinbefore provided neither the thesis nor any substantial portion thereof may be printed or otherwise reproduced in any material form whatever without the author's prior written permission.



52 Willow Way

Edmonton, Alberta, Canada

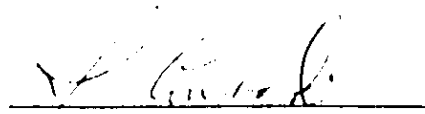
T5T 1C8

**DATE:** Nov 5, 1995

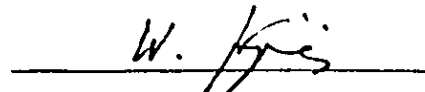
University of Alberta

Faculty of Graduate Studies And Research

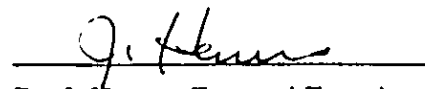
The undersigned certify that they have read, and recommend to the Faculty of Graduate Studies and Research for acceptance, a thesis entitled **CLIPPING-INDUCED IMPULSIVE NOISE IN DIRECTLY MODULATED FIBER OPTIC CATV TRANSMISSION SYSTEMS** submitted by **STEPHEN WILLIAM LAI** in partial fulfillment of the requirements for the degree of **MASTER OF SCIENCE** in Electrical Engineering.



Dr. J. Conradi, Supervisor



Dr. W. Krzymien, Internal Examiner



Dr. J. Harms, External Examiner

DATE: Oct 31, 1995

## **Dedication**

*To my parents, William and Vivien Lai.*

*Their love, encouragement, and support over the years  
have made this achievement possible.*

## **Abstract**

In an optical CATV transmission system, clipping-induced impulsive noise is generated when the signal current falls below the threshold current of the laser diode in the transmitter. This thesis contains a theoretical and experimental study of the clipping mechanism in a direct modulation optical transmitter and the resulting impulsive noise that is observed in the optical receiver.

A theoretical time-based shot noise model is developed to mathematically represent the clipping process. The clipping events are modeled as a Poisson sequence of short-duration pulses having random areas. Analysis of the receiver response to the clipping process, results in theoretical expressions for the characteristic function of clipping-induced impulsive noise and the Bit Error Ratio (BER) of a digital signal in the presence of combined Gaussian and impulsive noise in a hybrid analog/digital lightwave system.

Experiments on low-pass filtered and down-converted impulsive noise reveal that the amplitude probability density of clipping-induced impulsive noise has a Gaussian-shaped central region and very pronounced tail regions. It is also observed that consecutive clipping events have a high probability of occurring 167 ns, 1.5  $\mu$ s, or 4  $\mu$ s apart in an NTSC CATV system with unmodulated carriers.

## **Acknowledgments**

I would first of all like to thank my supervisor, Dr. Jan Conradi, for the guidance and excellent facilities that were provided during my thesis work. In addition, I would like to thank the members of my examining committee, Dr. Jan Conradi, Dr. Janelle Harms, and Dr. Witek Krzymien, for reviewing this thesis.

I would also like to acknowledge the technical guidance and support of David Clegg, Tim Friesen, Jason Lamont, and Jim Slevinsky in the design and construction of the Threshold Detector used in my experiments. I would also like to thank Dean Michaels for helping me with the computer-related problems that I encountered.

I would like to thank my colleagues, Ben Chan, David Moore, Sheldon Walklin, Ping Wan, and Tom Young, for many interesting and stimulating discussions. They along with the rest of the students and staff at TRLabs have created an excellent research environment.

I wish to acknowledge the Natural Sciences and Engineering Research Council, TRLabs, and the University of Alberta for the generous financial support during the course of this work.

Finally, I would like to thank my family and friends for their encouragement and support that made this work possible.

This work was supported by the Natural Sciences and Engineering Research Council of Canada, Bell-Northern Research, and TRLabs through the NSERC/BNR/TRLabs Industrial Research Chair in Fiber Optic Communications at the University of Alberta.



## Table of Contents

1. Introduction.....	1
1.1 Historical Perspective .....	2
1.1.1 Evolution From Copper to Fiber in CATV Systems .....	2
1.1.2 The Introduction of Digital Video Transmission.....	4
1.1.3 Clipping-Induced Impulsive Noise.....	5
1.2 Research Objectives and Organization of Thesis.....	8
2. Transmission of Analog Video Signals over Optical Fiber.....	9
2.1 Transmission Methods.....	9
2.1.1 Subcarrier Multiplexing.....	9
2.1.2 Amplitude Modulation: Vestigial Sideband (AM-VSB).....	11
2.2 Measuring System Performance .....	13
2.2.1 Modulation Index.....	14
2.2.2 Gaussian Noise .....	17
2.2.2.1 Front-End Thermal Noise.....	18
2.2.2.2 Shot Noise .....	18
2.2.2.3 RIN Noise .....	19
2.2.2.4 Carrier-to-Noise Ratio (CNR).....	19
2.2.3 Nonlinear Distortion.....	20
3. A Model for Clipping-Induced Impulsive Noise .....	25
3.1 Laser Characteristics .....	25
3.2 Frequency Domain Analysis .....	27
3.2.1 Modeling the SCM Signal as a Gaussian Process .....	28
3.2.2 The Spectrum of a Clipped SCM Signal.....	30
3.3 Time Domain Analysis.....	33
3.3.1 The Clipped Signal as a Sum of Two Signals.....	34
3.3.2 Asymptotic Clipping .....	35
3.3.3 Filtering the Clipped SCM Signal .....	38
3.3.3.1 Qualitative Analysis: Bandlimiting Effect of a Bandpass Filter	39

3.3.3.2 Quantitative Analysis: The Response at the Filter Output.....	42
3.3.4 The Impact of Clipping on the Bit Error Ratio of an ASK Channel in a Hybrid AM-VSB/ASK System.....	46
3.3.4.1 System Model .....	47
3.3.4.2 Receiver Noise Analysis .....	50
3.3.4.3 The Gaussian Noise Component.....	52
3.3.4.4 The Impulsive Noise Component.....	52
3.3.4.5 Probability of Symbol and Bit Error.....	55
3.3.4.6 Extending the Results to M-ary QAM .....	56
3.3.4.7 The Case of Rectangular Pulses.....	57
4. Implementation of a Fiber-Optic AM-VSB System .....	58
4.1 Analog Channel Modulators.....	59
4.2 Analog Optical Transmitter .....	59
4.3 Analog Optical Receiver .....	61
4.4 Low-Pass Filter Circuit .....	64
4.5 Threshold Detector .....	67
4.6 Down-Converter.....	68
4.7 System Characterization .....	70
4.7.1 Modulation Index Calibration .....	70
4.7.2 System CNR .....	73
5. Experiments on Clipping-Induced Impulsive Noise .....	76
5.1 Low-Pass Filter Experiments .....	76
5.1.1 Amplitude Distribution.....	79
5.1.2 Impulse Rate .....	87
5.1.3 Time Distribution .....	92
5.2 Down-Converter Experiments .....	97
5.2.1 Qualitative Nature of Down-Converted Impulsive Noise.....	98
5.2.2 Amplitude Distribution.....	100
5.3 Broadening of the Main Lobe in the Amplitude Distributions of Low-Pass Filtered and Down-Converted Impulsive Noise.....	106
5.4 BER Impairment in an AM-VSB/64-QAM Hybrid System .....	107

6. Conclusions.....	111
6.1 Summary of Conclusions.....	111
6.2 Recommendations for Further Research.....	112
REFERENCES.....	114
Appendix A: CATV Channel Frequencies.....	119
Appendix B: Modeling the Parabolic Pulses as Impulses .....	121
Appendix C: Deriving the Area Probability Density of the Parabolic Pulses.....	123
Appendix D: Approximating the Probability Density of Excursion Amplitudes with Threshold Crossing Rate Data .....	126
Appendix E: Explanation for the Dominant 167 ns and 1.5 $\mu$ s Time Interval Between Clipping Events.....	129
Appendix F: Computer Program Listings .....	134
Appendix G: Threshold Detector Design .....	145

## List of Tables

Table 4.1: Down-Converter Component Model Numbers.....	70
Table 5.1: Standard Deviations for Low-Pass Filtered Impulsive Noise .....	86
Table 5.2: Standard Deviations for Down-Converted Impulsive Noise. $f_c = 549$ MHz and $f_{IF} = 70$ MHz.....	101
Table 5.3: Standard Deviations for Down-Converted Impulsive Noise. $f_c = 549$ MHz and $f_{IF} = 0$ MHz.....	102

## List of Figures

Figure 1.1: Typical Copper-Based CATV Distribution Network.....	3
Figure 1.2: Hybrid Fiber/Coax Distribution Network .....	4
Figure 1.3: Laser Threshold Clipping.....	6
Figure 1.4: Impulsive Noise Waveform .....	7
Figure 2.1: Block Diagram of a Subcarrier Multiplexed System.....	10
Figure 2.2: Frequency Spectrum of the SCM Signal at the Receiver.....	10
Figure 2.3: Example Spectrum of a VSB Modulated Signal and its Equivalent DSB Spectrum .....	12
Figure 2.4: Spectrum of an NTSC Television Channel.....	13
Figure 2.5: Analog Signal Modulation of a Laser Diode.....	15
Figure 2.6: Noise Equivalent Circuit for an Optical Receiver .....	18
Figure 2.7: A System with Input $x(t)$ and Output $y(t)$ .....	20
Figure 2.8: System Transfer Function .....	21
Figure 2.9: Intermodulation Products in the CATV Frequency Band.....	23
Figure 2.10: CSO, CTB and Other Intermodulation Products in a CATV Channel .....	24
Figure 3.1: L-I Curve for a Typical CATV Laser.....	26
Figure 3.2: L-I Curve for an Ideal CATV Laser .....	27
Figure 3.3: Physical Representation of the Gaussian Approximation.....	29
Figure 3.4: The Function $g(x)$ .....	32
Figure 3.5: The Clipped Signal as a Sum of Two Signals.....	34
Figure 3.6: Downcrossing Rate vs. Modulation Index for a 42 Channel System .....	36
Figure 3.7: Mean Excursion Duration vs. Modulation Index for a 42 Channel System ...	37
Figure 3.8: Probability Density of Excursion Duration for $m=0.04$ .....	38
Figure 3.9: The Error Process .....	38
Figure 3.10: System Model of Clipped and Filtered Signal .....	39
Figure 3.11: SCM Spectrum and BPF Passband.....	40
Figure 3.12: Response of the BPF to the Clipped Signal.....	41
Figure 3.13: Response of the BPF to the Error Signal.....	42
Figure 3.14: Filtered Error Process .....	43
Figure 3.15: Impulse Response of an Ideal BPF .....	46
Figure 3.16: Typical AM-VSB/ASK Hybrid System .....	47
Figure 3.17: Unclipped Case.....	48
Figure 3.18: Modified Model .....	49

Figure 3.19: Down-converter and Demodulator .....	51
Figure 4.1: Block Diagram of Experimental AM-VSB Optical Transmitter and Analysis System.....	58
Figure 4.2: Optical Power vs. Bias Current for Fujitsu CATV Laser.....	60
Figure 4.3: Threshold Region of Optical Power vs. Bias Current Curve.....	61
Figure 4.4: Setup for Determining Receiver Frequency Response .....	63
Figure 4.5: Frequency Response of the Ipittek Receiver .....	63
Figure 4.6: Low Frequency Response of the Ipittek Receiver.....	64
Figure 4.7: Low-Pass Filter Circuit .....	65
Figure 4.8: Magnitude of Low-Pass Filter Frequency Response.....	66
Figure 4.9: Low-Pass Filter Impulse Response .....	66
Figure 4.10: Sample Waveforms of Comparator Input and Output .....	67
Figure 4.11: Block Diagram of the Threshold Detector.....	68
Figure 4.12: Block Diagram of Down-Converter.....	69
Figure 4.13: Modulation Index Calibration Setup .....	71
Figure 4.14: Carrier Power vs. Bias Current for Channel 21 (163.25 MHz).....	73
Figure 4.15: Experimental Setup for Measuring CNR.....	74
Figure 4.16: Measured and Calculated System CNR Performance.....	75
Figure 5.1: Generating Low-Pass Filtered Impulsive Noise .....	77
Figure 5.2: Spectrum of Low-Pass Filtered and Amplified Impulsive Noise .....	78
Figure 5.3: Low-Pass Filtered Impulsive Noise Sample Waveform .....	79
Figure 5.4: Setup for Amplitude Distribution Experiment.....	80
Figure 5.5: Probability Density of Low-Pass Filtered Impulsive Noise.....	81
Figure 5.6: Probability Density of Low-Pass Filtered Impulsive Noise for $m = 0.02$ ....	83
Figure 5.7: Probability Density of Low-Pass Filtered Impulsive Noise for $m = 0.05$ ....	83
Figure 5.8: Probability Density of Low-Pass Filtered Impulsive Noise for $m = 0.055$ ...	84
Figure 5.9: Probability Density of Low-Pass Filtered Impulsive Noise for $m = 0.062$ ...	84
Figure 5.10: Setup for Impulse Rate Experiment.....	87
Figure 5.11: Threshold Upcrossing Rate vs. Threshold Voltage.....	88
Figure 5.12: Probability Density of Excursion Amplitudes for Low-Pass Filtered Impulsive Noise .....	90
Figure 5.13: Comparing Probability Densities of Experimental Noise Excursion Amplitude to Theoretical Impulse Area .....	91
Figure 5.14: Setup for Time Distribution Experiment.....	92
Figure 5.15: Time Interval Histogram for 0.2 V Threshold. Sample Size = 5000, Multi-Counter Rate = 1.1 MHz, and $m = 0.05$ . .....	93

Figure 5.16: Time Interval Histogram for 0.24 V Threshold. Sample Size = 5000, Multi-Counter Rate = 670 kHz, and $m = 0.05$ .....	94
Figure 5.17: Time Interval Histogram for 0.4 V Threshold. Sample Size = 5000, Multi-Counter Rate = 95 kHz, and $m = 0.05$ . ....	94
Figure 5.18: Time Interval Histogram for 1.0 V Threshold. Sample Size = 5000, Multi-Counter Rate = 582 kHz, and $m = 0.062$ . ....	95
Figure 5.19: Time Interval Probability Density for a Poisson Process with $1/\lambda = 2.97 \mu s$	96
Figure 5.20: Setup for Down-Converter Experiment .....	98
Figure 5.21: Sample Waveform of Down-Converted Impulsive Noise. 500 ns/div, $f_c = 417$ MHz, $f_{IF} = 44$ MHz, and $m = 0.05$ . ....	99
Figure 5.22: Sample Waveform of Down-Converted Impulsive Noise. 200 ns/div, $f_c = 417$ MHz, $f_{IF} = 44$ MHz, and $m = 0.05$ . ....	99
Figure 5.23: Sample Waveform of Down-Converted Impulsive Noise. 20 ns/div, $f_c = 417$ MHz, $f_{IF} = 44$ MHz, and $m = 0.05$ .....	100
Figure 5.24: Probability Density of Down-Converted Impulsive Noise. $f_c = 549$ MHz and $f_{IF} = 70$ MHz. ....	101
Figure 5.25: Probability Density of Down-Converted Impulsive Noise. $f_c = 549$ MHz and $f_{IF} = 0$ MHz.....	102
Figure 5.26: Effect of Intermediate Frequency on Probability Density $m = 0.062$ .....	103
Figure 5.27: Theoretical and Experimental Probability Density $m = 0.062$ .....	105
Figure 5.28: Adjusted Theoretical and Experimental Probability Density $m = 0.062$ ....	106
Figure 5.29: Experimental AM-VSB/64-QAM Hybrid System.....	107
Figure 5.30: BER vs. QAM Modulation Index in a Hybrid System .....	108
Figure 5.31: Predicted BER for 64-QAM versus AM rms Modulation Index.....	110
Figure C.1: Parabolic Pulse .....	123
Figure D.1: Definition of Excursion Amplitude.....	126
Figure D.2: One Excursion Being Detected as Two Excursions.....	127
Figure D.3: Deriving Excursion Amplitude Probability Density from Crossing Rate Data	128
Figure G.1: Counter Controller State Diagram.....	146

## **List of Abbreviations**

<b>AM-VSB</b>	<b>Vestigial Sideband Amplitude Modulation</b>
<b>ASE</b>	<b>Amplified Spontaneous Emission</b>
<b>ASK</b>	<b>Amplitude-Shift Keying</b>
<b>BPF</b>	<b>Bandpass Filter</b>
<b>BER</b>	<b>Bit Error Ratio</b>
<b>CATV</b>	<b>Community Antenna Television</b>
<b>coax</b>	<b>Coaxial Cable</b>
<b>CNR</b>	<b>Carrier-to-Noise Ratio</b>
<b>CSO</b>	<b>Composite Second Order</b>
<b>CTB</b>	<b>Composite Triple Beat</b>
<b>dB</b>	<b>Decibel</b>
<b>DFB</b>	<b>Distributed Feedback</b>
<b>DSB</b>	<b>Double Sideband</b>
<b>EDFA</b>	<b>Erbium Doped Fiber Amplifier</b>
<b>FAST</b>	<b>National Semiconductor High-Speed TTL Logic Family</b>
<b>FCC</b>	<b>Federal Communications Commission</b>
<b>FDM</b>	<b>Frequency Division Multiplexing</b>
<b>HDTV</b>	<b>High-Definition Television</b>
<b>HP</b>	<b>Hewlett Packard</b>
<b>HP-IB</b>	<b>Hewlett-Packard Interface Bus</b>
<b>IC</b>	<b>Integrated Circuit</b>
<b>IF</b>	<b>Intermediate Frequency</b>
<b>ISI</b>	<b>Intersymbol Inteference</b>
<b>L-I</b>	<b>Light Power versus Current</b>
<b>LED</b>	<b>Light-Emitting Diode</b>
<b>LNA</b>	<b>Low Noise Amplifier</b>
<b>LO</b>	<b>Local Oscillator</b>
<b>LPF</b>	<b>Low-Pass Filter</b>
<b>MPEG</b>	<b>Moving Picture Experts Group</b>
<b>N-VSB</b>	<b>Vestigial Sideband Digital Modulation</b>
<b>NCTA</b>	<b>National Cable Television Association</b>
<b>NTSC</b>	<b>National Television Systems Committee</b>
<b>QAM</b>	<b>Quadrature Amplitude Modulation</b>



<b>RF</b>	<b>Radio Frequency</b>
<b>RIN</b>	<b>Relative Intensity Noise</b>
<b>rms</b>	<b>Root-Mean-Square</b>
<b>SCM</b>	<b>Subcarrier Multiplexed</b>
<b>SNR</b>	<b>Signal-to-Noise Ratio</b>
<b>SSB</b>	<b>Single Sideband</b>
<b>TDM</b>	<b>Time Division Multiplexing</b>
<b>TRLabs</b>	<b>Telecommunication Research Laboratories</b>
<b>TTL</b>	<b>Transistor-Transistor Logic</b>
<b>TV</b>	<b>Television</b>
<b>VOA</b>	<b>Variable Optical Attenuator</b>
<b>WDM</b>	<b>Wavelength Division Multiplexing</b>

## List of Symbols

$\langle \quad \rangle$	denotes time-average
$A$	area of parabolic pulses in error process
$\overline{A^2}$	mean square value of $A$
$B$	effective noise bandwidth of receiver
$c$	constant used in definition of $p(A)$
$c_1, c_2, c_3, c_h$	generic constants
$c(t)$	clipped signal waveform
$CDF_A$	cumulative distribution of $A$
$CDF_{\tau_p}$	cumulative distribution of $\tau_p$
$d(t)$	desired signal waveform
$\delta(\quad)$	Dirac impulse function
$e(t)$	error signal waveform
$e_m(t)$	uncorrelated error signal waveform
$e_{out}(t)$	error signal at output of narrowband filter
$e_i(t)$	error signal at input to decision circuit
$f_a$	carrier frequency of lowest channel
$f_b$	carrier frequency of highest channel
$f_c$	channel or filter center frequency
$\Delta f_{BW}$	bandpass filter bandwidth
$f_{CR}$	carrier frequency
$f_i$	carrier frequency of $i^{\text{th}}$ channel
$f_{IF}$	intermediate frequency
$F$	preamplifier noise factor in receiver
$F[ \quad ]$	denotes the Fourier Transform
$F^{-1}[ \quad ]$	denotes the Inverse Fourier Transform

$F_{\theta}$	random variable representing multiplication with oscillator tone
$h(t)$	impulse response
$h_{bb}(t)$	impulse response of baseband filter in a digital demodulator
$h_{BPF}(t)$	impulse response of bandpass filter
$H_k( )$	$k^{\text{th}}$ order Hermite function
$H_{BPF}(\omega)$	transfer function of a bandpass filter
$\langle i_{RIN}^2 \rangle$	time-averaged square of RIN noise current
$\langle i_{sh}^2 \rangle$	time-averaged square of shot noise current
$\langle i_{sig}^2 \rangle$	time-averaged square of AM-VSB carrier current
$\langle i_t^2 \rangle$	time-averaged square of thermal noise current
$i_{th}^2$	front-end noise current spectral density (in $A^2/Hz$ )
$I_c$	100% modulation bias current
$I_{bias}$	laser bias current
$I_{peak}$	amplitude of sinusoidal signal in terms of modulating current
$I_{th}$	laser threshold current
$I_{in}(t)$	modulating portion of laser drive current
$I_{tot}(t)$	total laser drive current
$J_0( )$	0 <sup>th</sup> order Bessel function of the first kind
$k$	Boltzmann's constant ( $1.38 \cdot 10^{-23}$ J/K)
$K_{1/6}( )$	1/6 <sup>th</sup> order modified Bessel function of the second kind
$K_{2\nu}$	second order power product count at frequency $\nu$
$K_{3\nu}$	third order power product count at frequency $\nu$
$\lambda$	average rate of clipping events
$m$	peak modulation index
$m_i$	peak modulation index of $i^{\text{th}}$ channel
$m_{rms,i}$	rms modulation index of $i^{\text{th}}$ channel
$m(t)$	modulating portion of signal

$M_G(j\nu)$	characteristic function of Gaussian noise
$M_I(j\nu)$	characteristic function of impulsive noise
$M_T(j\nu)$	characteristic function of Gaussian and impulsive noise
$\mu$	total rms modulation index
$n_G(t)$	sample function of Gaussian noise current
$n_I(t)$	sample function of impulsive noise current
$N$	number of CATV channels
$N_G$	random amplitude of Gaussian noise at input to decision circuit
$N_I$	random amplitude of impulsive noise at input to decision circuit
$N_T$	random amplitude of Gaussian and impulsive noise at input to decision circuit
$p(A)$	probability density of $A$
$p(\tau_p)$	probability density of $\tau_p$
$p_s(x)$	amplitude probability density of $s(t)$
$P(t)$	transmitted optical power waveform
$P_{bias}$	corresponding optical power at bias current $I_{bias}$
$P_{prsk}$	amplitude of sinusoidal signal in terms of optical power
$P_o$	average received optical power
$q$	electronic charge ( $1.602 \times 10^{-19}$ C)
$\mathfrak{R}$	photodetector responsivity
$R_{eq}$	equivalent resistance of photodiode load
$R_{in}(\tau)$	autocorrelation function of input modulating current
$R_o(\tau)$	autocorrelation function of output of laser output
$s(t)$	zero-mean Gaussian random process
$s_m(t)$	$m^{\text{th}}$ transmitted symbol waveform of an ASK signal
$\sigma_G^2$	variance of Gaussian noise in terms of $A^2$
$\sigma_I^2$	variance of impulsive noise in terms of $A^2$

$\sigma_{in}^2$	sum of all carrier variances in terms of current
$\sigma_i^2$	variance of $s(t)$
$\sigma_g$	standard deviation of Gaussian noise in experiment
$\sigma_i$	standard deviation of impulsive noise in experiment
$\sigma_{tot}$	standard deviation of total noise in experiment
$T$	absolute temperature
$[-T_u, T_u]$	time interval for which $u(t)$ has a non-zero value
$\theta_i$	phase of $i^{\text{th}}$ channel carrier
$\tau_p$	time duration of a clipping event
$\overline{\tau_p}$	average time duration of a clipping event
$\omega_{ASK}$	center frequency of ASK channel
$u(t)$	digital symbol pulse shape
$V_{c_{p,p}}$	voltage amplitude of input sinusoidal signal causing 100% modulation at transmitter
$V_{in_{p,p}}$	voltage amplitude of input sinusoidal signal to transmitter
$x_p(t)$	parabolic pulse
$\gamma$	clipping index

## 1. Introduction

The use of fiber optics in modern communication networks has become widespread over the past several years. The maturity of lightwave technology and the reduction of optical component costs have progressed sufficiently that, for many communication links, it has become viable to exploit the inherent advantages of optical fiber transmission. Optical fiber transmission offers the advantages of high bandwidth, low loss, immunity to electrical interference, and insensitivity to temperature changes. In some communication systems, it is economically feasible to replace the existing copper-based transmission medium with optical fiber in the interest of increasing the system noise performance, increasing the system bandwidth, or reducing the system operating costs.

Although the most extensive use of fiber optics has been for long-distance trunking applications in the telephone industry, there has also been substantial growth in the area of Community Antenna Television (CATV) broadcasting. The vision of a broadband network delivering integrated voice, data, and video services to the home [1] has been aggressively marketed towards consumers in the form of an “information superhighway”. As a result, multichannel lightwave video transmission has been a very active research area as engineers and scientists strive to understand the performance characteristics of future CATV systems. One of the main performance limitations that have been identified in recent studies is clipping-induced impulsive noise, which is the basis of the work in this thesis.

In this introductory chapter, a brief historical perspective of CATV distribution is given leading up to the subject of clipping-induced impulsive noise as a fundamental performance limitation. This is followed by a section presenting the research objectives and organization of this thesis.

## **1.1 Historical Perspective**

In this section, the evolution of the CATV network from a fully copper-based structure to a fully-fiber based structure is discussed. The recent progress towards digital video transmission is subsequently described. Finally, the problem of clipping-induced impulsive noise is presented.

### **1.1.1 Evolution From Copper to Fiber in CATV Systems**

The purpose of the first CATV systems was to receive off-the-air broadcast signals and to distribute them, via coaxial cable, to areas where the reception of TV signals using conventional TV antennas was poor or non-existent. These areas were typically far from TV broadcast antennas situated in other cities. The high signal quality and variety of channels offered by CATV systems resulted in its increased popularity even in areas where the reception of airborne TV signals was adequate. As a result of the large demand for CATV services, CATV networks have been extensively deployed in many urban areas in North America.

The typical structure of a copper-based CATV distribution network is shown in Figure 1.1 [2]. The television signals are distributed to subscribers with a tree-branch type network. The head end facility receives high quality video signals from satellites, off-air broadcasts, and distant-feeds. These video signals are combined, and transmitted over supertrunks to regional distribution sites called hubs. At each hub, the CATV signals are distributed to subscribers with amplifiers, splitters, and taps. The amplifiers in the system are used to compensate for the power loss due to coaxial cable attenuation and signal branching. Current coaxial trunks may contain up to 30 electronic amplifiers in cascade [2], each of which contributes to the degradation of the TV signal as it progresses towards the subscriber termination. A high number of cascaded amplifiers may result in unacceptable levels of distortion and noise. The use of optical fiber for supertrunking pushes the high quality signals available at the head end closer to each subscriber.

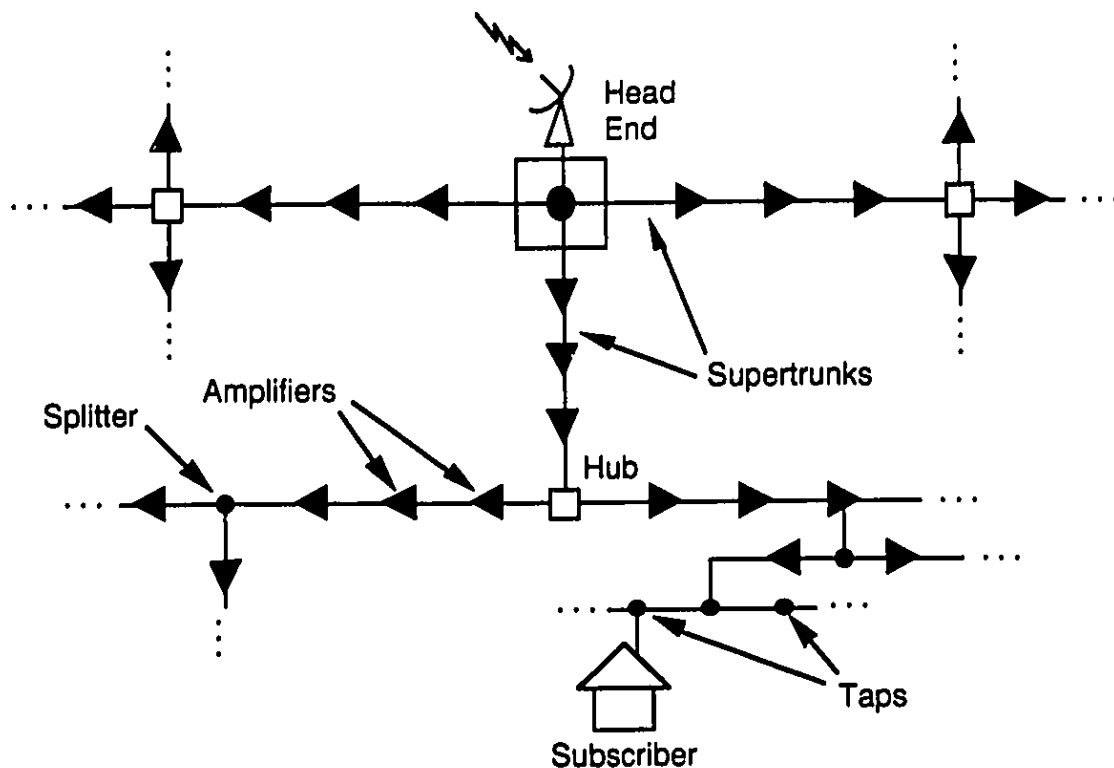


**Figure 1.1: Typical Copper-Based CATV Distribution Network**

Hybrid fiber/coax networks are one of the leading architectural choices for the delivery of current and future video services [3]-[5]. One hybrid fiber/coax technique, dubbed the “fiber backbone”, is illustrated in Figure 1.2 [6]. In this scheme, the network is divided into smaller service zones, each of which is fed by an optical link from the head end. Conversion nodes in each service zone are used to convert the optical signal to an electrical signal that is distributed with the existing electrical local network. The popularity of the fiber backbone structure stems from the economic advantage of reusing the existing electronic equipment and the improvement in reliability and performance realized by replacing the lengthy cascades of amplifiers with optical supertrunks.



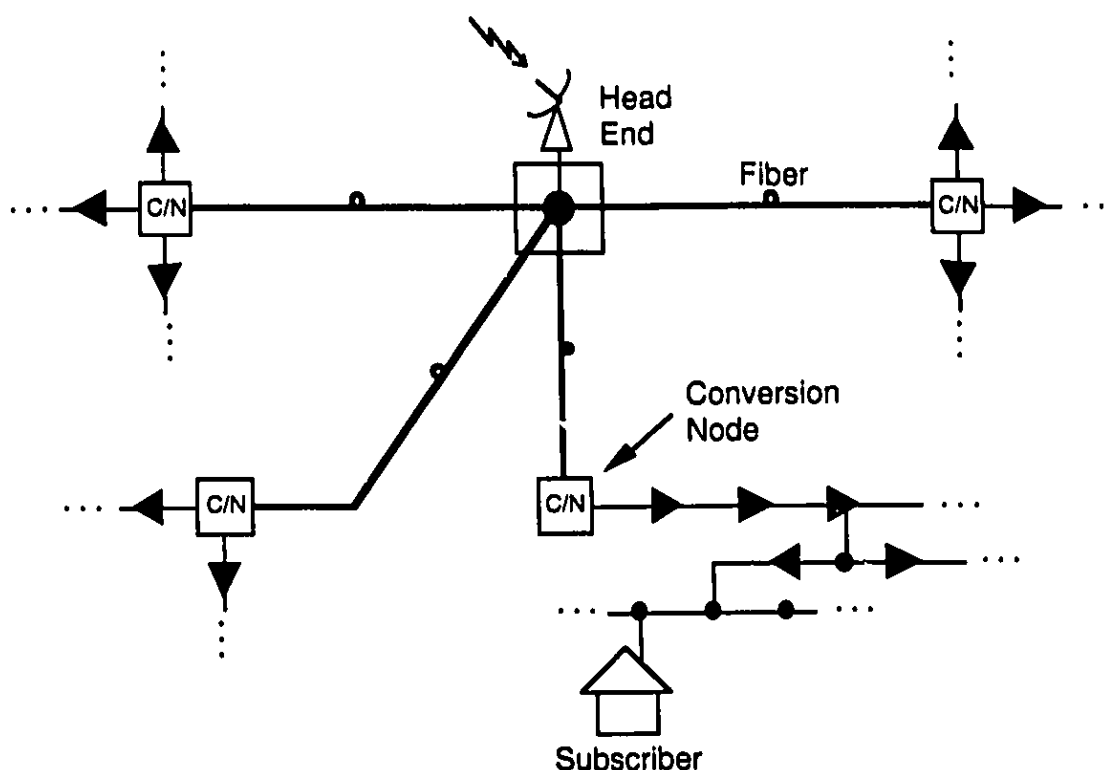


**Figure 1.2: Hybrid Fiber/Coax Distribution Network**

One might suggest that the continuing evolution of CATV networks may eventually lead to an all fiber network. There has been a great deal of discussion both in favor and against the need for extending the fiber plant into individual residences. Presently, the concept of an all fiber system is generally considered to be economically unfeasible because of the low demand for the additional services that fiber can provide and the high cost associated with rewiring subscriber's homes and replacing existing receiver circuitry with optical equivalents [6].

### **1.1.2 The Introduction of Digital Video Transmission**

In early optical video systems, subcarrier multiplexing employing the analog Vestigial Sideband Amplitude Modulation (AM-VSB) format was used because of its low cost, ease of implementation, and compatibility with existing TV sets. These advantages

are offset by the strict noise and distortion requirements for multichannel AM-VSB transmission [2]. Advances in the theory and application of digital information processing and transmission have led to rapid progress in the area of digital video transmission.

Digital video transmission offers the advantages of robustness, flexibility, and compatibility with the anticipated broadband digital network of the future. The introduction of digital video in commercial broadcasting has been ensured by recent proceedings of the Federal Communications Commission (FCC) which is seeking to standardize the format for the next-generation high-definition television (HDTV) [7]. The FCC is working with a consortium of communications equipment manufacturers and academic institutions, dubbed the Grand Alliance, to optimize the transmission format for future HDTV broadcasting. The format currently under consideration uses a digital modulation technique called N-VSB which was developed by Zenith. The video information is digitized and highly compressed using the MPEG-2 protocol resulting in a proposed digital symbol rate of 10.76 MHz [8].

In the evolution from an all-analog to an all-digital video network, there will be a transition period when digital channels are transmitted with existing analog channels simultaneously. The physical implementation of this transport scheme using fiber optics is called the analog/digital hybrid lightwave system. Analog/digital hybrid systems have been the subject of many recent studies [9]-[21] and have resulted in the identification of clipping-induced impulsive noise as a significant performance impairment of the digital channels.

### **1.1.3 Clipping-Induced Impulsive Noise**

In directly modulated systems, clipping of the optical signal is a consequence of the input current-to-output optical power transfer characteristic of the laser in the transmitter. As shown in Figure 1.3, when the laser drive current is higher than the threshold current  $I_{th}$ , the laser transmits an optical equivalent of the input modulating current. However,

when the modulating current falls below threshold, the output optical power stays near zero. The result is a clipped optical signal.

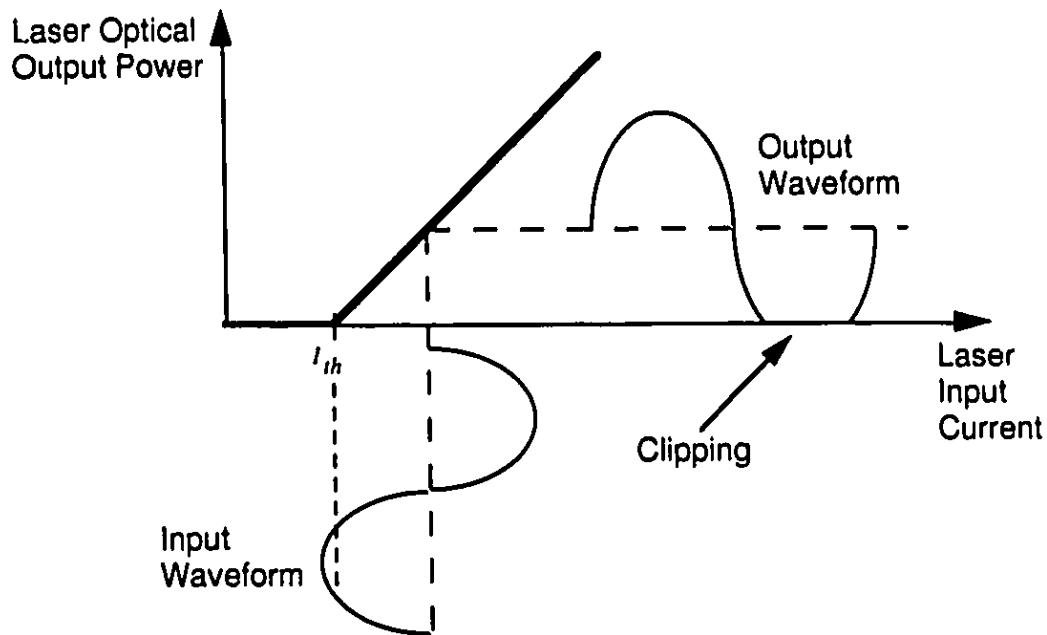


**Figure 1.3: Laser Threshold Clipping**

It has been observed that clipping imposes limits on the minimum attainable Bit Error Ratio (BER) of a digital channel in a hybrid system [10]. In recent experiments, the time domain response of clipping noise in a digital channel has been investigated by turning the digital signal off and connecting an oscilloscope to the channel output at the receiver [9], [10], [13]. It has been revealed that the noise in the channel consists of large amplitude, randomly occurring excursions called impulses. An example of this impulsive noise waveform is shown in Figure 1.4.

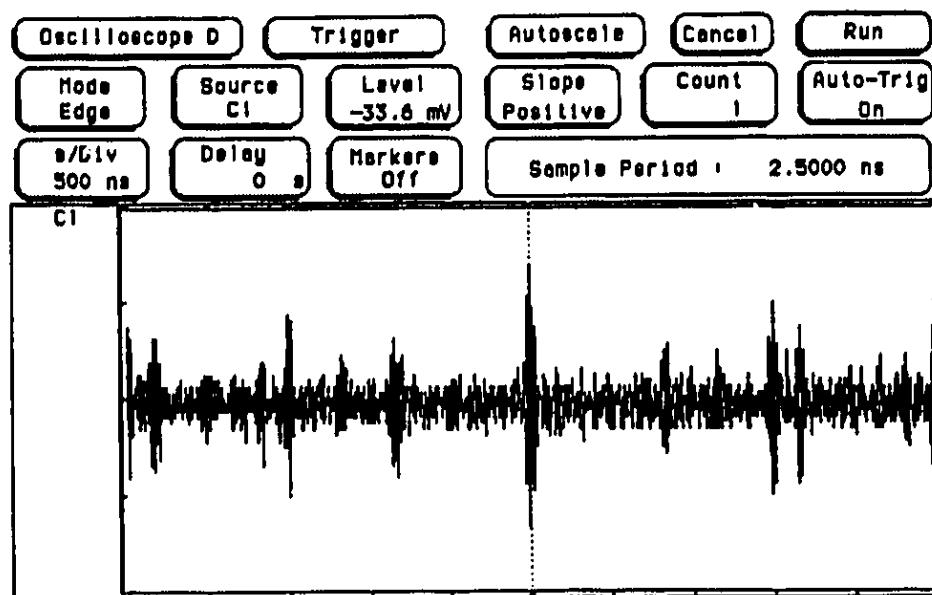


**Figure 1.4: Impulsive Noise Waveform**

To minimize the effect of clipping, one might suggest that the amplitude swing of the laser modulating current be reduced such that clips do not occur. Although this approach does eliminate the degradation due to clipping, the reduced amplitude of the optical signal also results in a decreased signal-to-noise (SNR) power ratio at the receiver. For subcarrier multiplexed AM-VSB/digital systems, the reduction of modulation amplitude to eliminate clipping can result in an unacceptably low SNR or insufficient channel capacity. The design of a practical hybrid AM-VSB/digital optical system involves design trade-offs where a balance is sought between the analog channel requirement of high SNR and the digital channel requirement of low BER [11]. The final design solution usually results in an amplitude modulation level that guarantees some degree of clipping in the system.

## **1.2 Research Objectives and Organization of Thesis**

Based on the current status of hybrid analog/digital optical CATV systems and the limited extent to which clipping-induced impulsive noise is currently understood, the author has established the following research objectives for this thesis:

- 1) Qualitatively determine how impulsive noise is generated from the clipping process.
- 2) Develop a mathematical model to predict the behavior of clipping-induced impulsive noise.
- 3) Experimentally characterize the amplitude and time domain statistics of clipping-induced impulsive noise.

This thesis is organized in the following manner. Chapter 2 contains a brief summary of the transmission methods of a subcarrier multiplexed AM-VSB lightwave system as well as the relevant system impairments. In Chapter 3, a review of the frequency domain analysis of laser diode clipping is followed by the development of a time domain model. The results of the model include the characteristic function of the impulsive noise process and an expression for the BER of an Amplitude-Shift Keyed (ASK) or Quadrature Amplitude Modulated (QAM) digital channel in a hybrid system. The implementation of an experimental fiber optic CATV system is discussed in Chapter 4. In Chapter 5, the results of experiments on clipping-induced impulsive noise are given and discussed. Finally, the conclusions of this study are given in Chapter 6.

## **2. Transmission of Analog Video Signals over Optical Fiber**

### **2.1 Transmission Methods**

This section introduces the theoretical principles of a Subcarrier Multiplexed (SCM), Vestigial Sideband Amplitude Modulated (AM-VSB) optical transmission system. This technique of transmitting several video signals simultaneously, which is applicable to many media including coaxial cable, optical fiber, and free space, is chosen for study because it is compatible with the current North American standard for transmitting analog television channels. This standard is called the National Television Systems Committee (NTSC) format and was first authorized in the United States by the FCC in 1953 [22].

#### **2.1.1 Subcarrier Multiplexing**

There are many multiplexing methods that can be used to transmit several television channels simultaneously down a single fiber optic communication link. Some of these methods include Time Division Multiplexing (TDM), Wavelength Division Multiplexing (WDM), and Subcarrier Multiplexing (SCM). SCM offers the advantages of flexibility and upgradability when it is utilized in broadband networks [23]. Another advantage is that an optical subcarrier multiplexed signal can be converted, with minimal receiver hardware complexity, to an electrical signal that is compatible with the NTSC format. The block diagram of a typical AM-VSB subcarrier multiplexed system is shown in Figure 2.1, and the corresponding frequency spectrum of the electrical signal at the receiver is shown in Figure 2.2.

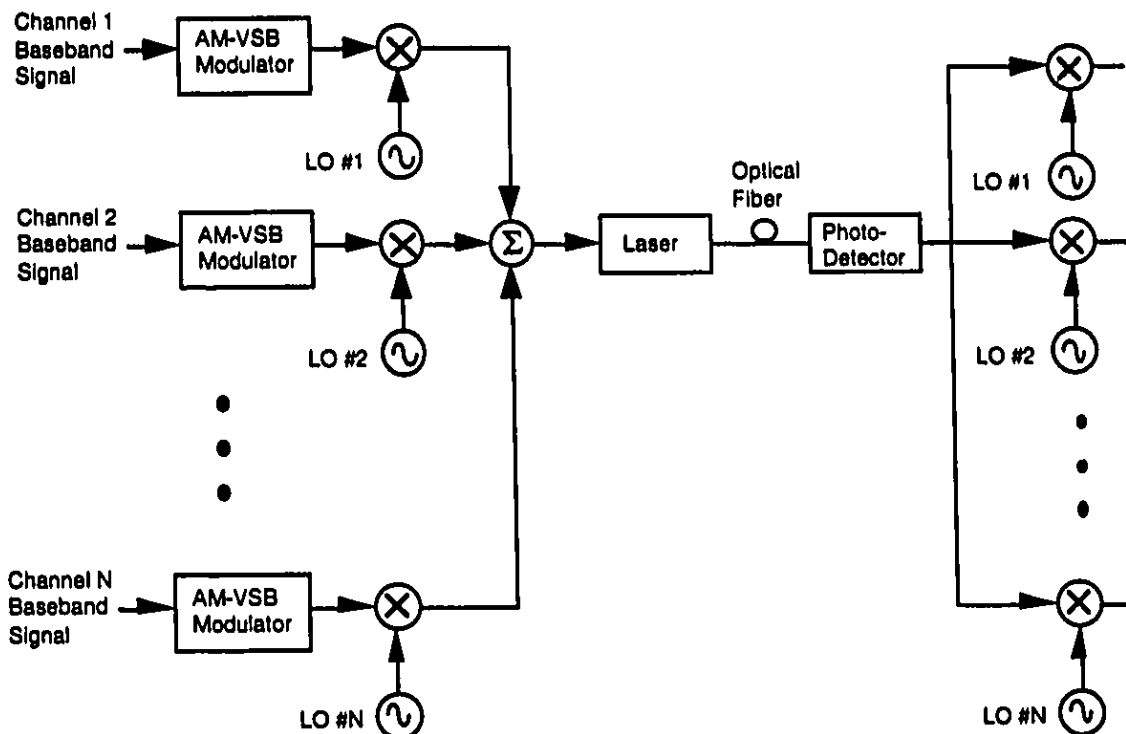


**Figure 2.1: Block Diagram of a Subcarrier Multiplexed System**

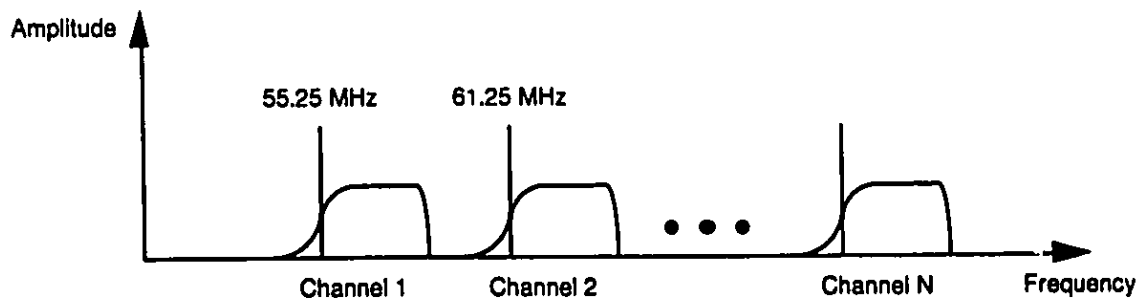


**Figure 2.2: Frequency Spectrum of the SCM Signal at the Receiver**

The subcarrier multiplexing technique is based on a mode of transmission called Frequency Division Multiplexing (FDM). In FDM, the signal spectra for different channels are positioned in frequency such that each signal spectrum can be separated out from the others by frequency filtering. In Figure 2.1, the baseband signal for each channel is used to amplitude modulate a series of carriers which are then frequency division multiplexed by

using local oscillators (LO's) at different frequencies. The modulated sinusoidal carriers are then combined to modulate the output optical intensity of the laser. Because the optical frequency of the laser is considered to be the main carrier frequency, the LO frequencies are called *subcarriers* to distinguish them from the main optical frequency. The subcarrier multiplexed output of the laser is coupled into the optical fiber and is then detected with a photodetector at the receiver. The photodetector converts the optical signal back to an electrical signal which can then be demultiplexed to derive the original baseband signals. The baseband signal for any channel can be obtained at the receiver by tuning a local oscillator to the channel frequency and performing AM-VSB demodulation.

### **2.1.2 Amplitude Modulation: Vestigial Sideband (AM-VSB)**

The techniques that could be used to amplitude modulate a CATV signal include Single Sideband (SSB), Double Sideband (DSB), and Vestigial Sideband (VSB) modulation. In the context of analog television broadcasting, the SSB modulation technique is too expensive to implement, and the DSB technique requires too much bandwidth [24]. Because AM-VSB modulation offers a compromise between SSB and DSB, it is chosen as the standard technique used for modulating analog television signals in North America.

In AM-VSB, one sideband is partially suppressed such that the demodulation process reproduces the original signal, but the required transmission bandwidth is reduced. Figure 2.3 shows an example spectrum of a VSB signal and the spectrum of an equivalent DSB signal. If a large carrier is also transmitted with the VSB modulated signal, a simple envelope detector circuit can be used to recover the baseband signal. If no carrier is sent, synchronous detection must be employed to recover the original modulating signal.



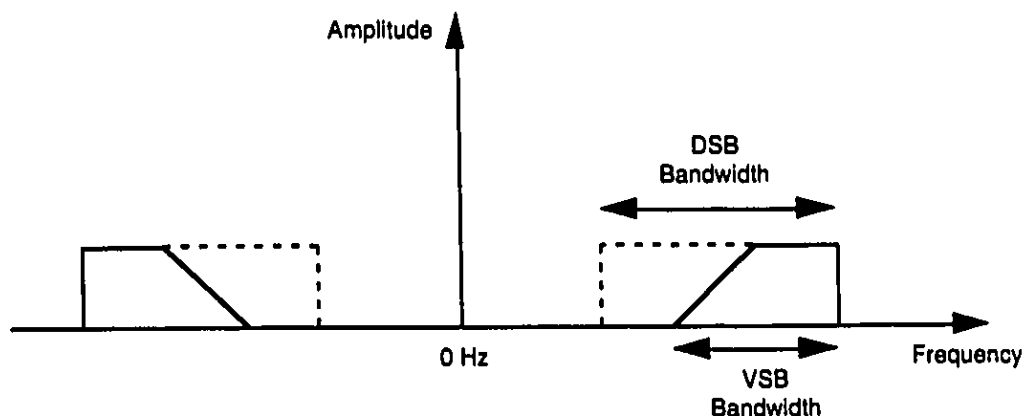


**Figure 2.3: Example Spectrum of a VSB Modulated Signal and its Equivalent DSB Spectrum**

The spectrum of a television channel which follows the NTSC AM-VSB format is shown in Figure 2.4 [22]. An NTSC television channel is allocated 6 MHz of bandwidth, and the major frequency components of the channel, in addition to the picture itself, include the video carrier, the sound carrier, and the color subcarrier. The video carrier is 1.25 MHz above the low frequency boundary, and the color subcarrier and audio carrier are 3.579545 MHz and 4.5 MHz above the video carrier, respectively, as shown in Figure 2.4. Because the video carrier is the most dominant frequency component in the 6 MHz channel, the performance of experimental CATV AM-VSB systems is often evaluated using only the video carrier of each television channel [25]. To simplify analysis and reduce hardware complexity, the theoretical and experimental work in this thesis follows this common practice to predict the characteristics of impulsive noise in practical CATV AM-VSB systems. A listing of the carrier frequencies and the allocated bandwidth for the first 42 channels of the NSTC frequency plan are given in Appendix A.

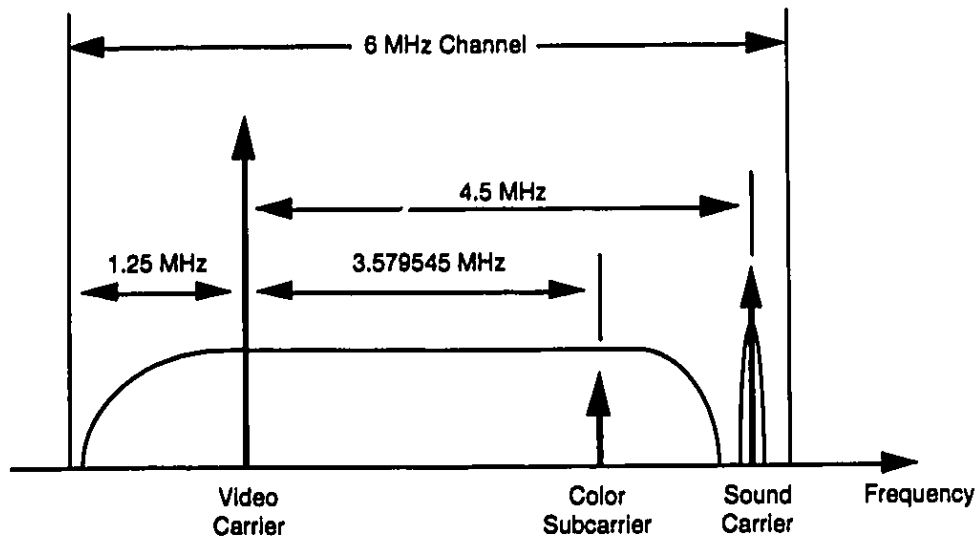


**Figure 2.4: Spectrum of an NTSC Television Channel**

## 2.2 Measuring System Performance

Because of the fragility of the analog television signals with respect to noise and distortion, AM-VSB transmission of CATV signals over optical fiber was not technically and financially feasible until the last 10 years [25]. The noise performance requirement of an analog CATV system is more stringent than an equivalent digital CATV system that carries the same channels. In fact, because of the robust nature of digital transmission, digital systems can withstand about 100 times more noise power than analog systems to deliver the same quality video signal [26]. However, the main disadvantage of using digital transmission for the distribution of existing TV channels are the high costs associated with converting the received signal into the required AM-VSB format.

To properly assess the performance of a CATV optical transmission system, the contribution that each component in the transmission chain makes to the noise and distortion in the CATV signal must be examined. In the following sections, we examine and define mathematically the two main impairments in an optical CATV system: noise and nonlinear distortion. Because the term "noise" is sometimes used quite generally, we further define this impairment as *Gaussian noise* to include only the sources of noise that

can be accurately characterized by a Gaussian probability distribution. The three dominant sources of Gaussian noise are receiver front-end thermal noise, shot noise, and relative intensity noise (RIN) [26]. Nonlinear distortion is a result of the nonlinear transfer function between the original electrical signal in the transmitter and the electric signal in the receiver and is caused by device imperfections and dynamic effects in the electrical and optical components in the system.

### 2.2.1 Modulation Index

The modulation index is used as a measure of the signal power relative to the total transmitted power in analog fiber optic systems. Because the modulation index is a critical parameter in the performance assessment of optical CATV systems and in the theory of clipping-induced impulsive noise, it is important that its definition be unambiguous. This section contains the definition for modulation index as it applies to a directly modulated laser diode optical source.

A typical drive-current-to-optical-intensity transfer characteristic of a CATV laser diode is shown in Figure 2.5 [27]. When the diode current is below the threshold current ( $I_{th}$ ), the laser emits minimal optical power. However, when the current is above threshold, the output optical power is significantly increased and has a linear relationship with the input current. If the laser is biased at a certain fixed current ( $I_{bias}$ ) and intensity modulated about  $I_{bias}$ , the optical output power will consist of a fixed bias power ( $P_{bias}$ ) and a time-varying component which varies linearly with the modulating current.

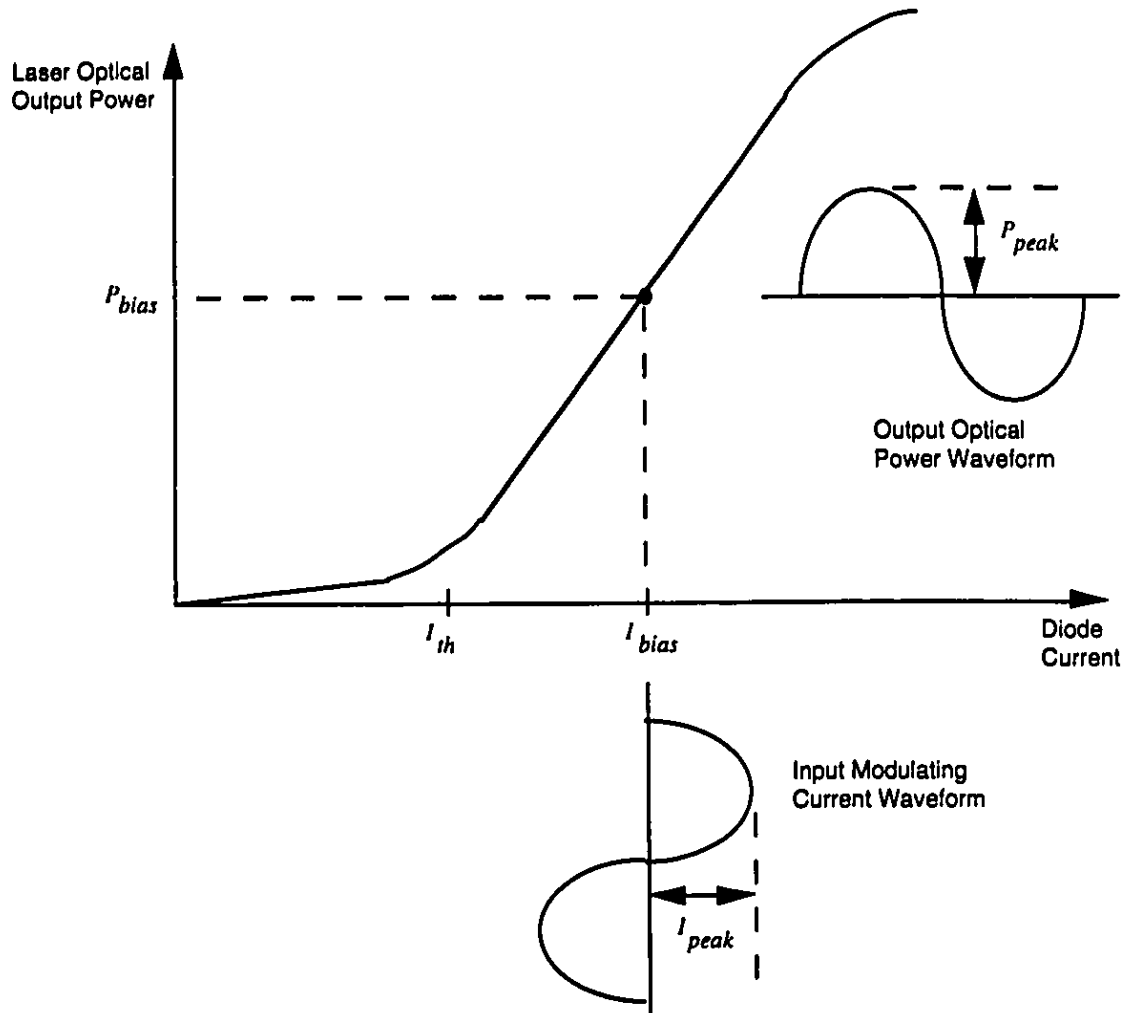


**Figure 2.5: Analog Signal Modulation of a Laser Diode**

The transmitted optical power can be represented by

$$P(t) = P_{bias}(1 + m(t)) \quad (2.1)$$

where  $P_{bias}$  corresponds to the optical power at the bias current ( $I_{bias}$ ) and  $m(t)$  is the modulating signal. It should be noted that if  $m(t)$  has an average value of zero over time, then  $P_{bias}$  is also the average transmitted optical power.

In analyzing the performance of AM-VSB SCM systems, it is usually assumed that the carrier for each channel is unmodulated (see Section 2.1.2), therefore, the modulating signal in a single channel system can be represented by

$$m(t) = m \cdot \cos(2\pi f_{CR}t) \quad (2.2)$$

where  $m$  is the peak modulation index and  $f_{CR}$  is the carrier frequency.

The peak modulation index is given by

$$m = \frac{P_{peak}}{P_{bias}} \quad (2.3)$$

where  $P_{peak}$  and  $P_{bias}$  are defined in Figure 2.5.

If the transfer characteristic of the laser is assumed to be linear, and if the current at threshold translates to negligible optical power, the peak modulation can also be defined in terms of current by

$$m = \frac{I_{peak}}{I_{bias} - I_{th}} \quad (2.4)$$

where  $I_{peak}$ ,  $I_{bias}$ , and  $I_{th}$  are defined in Figure 2.5.

In the case of a multichannel CATV system, the modulating signal consists of a sum of carriers at different frequencies, and the transmitted optical signal can be represented by [28]

$$P(t) = P_{bias} \left( 1 + \sum_{i=1}^N m_i \cdot \cos(2\pi f_i t + \theta_i) \right) \quad (2.5)$$

where  $N$  is the number of channels,  $m_i$  is the peak modulation of the  $i^{\text{th}}$  channel,  $f_i$  is the frequency of the  $i^{\text{th}}$  carrier, and  $\theta_i$  is the phase of the  $i^{\text{th}}$  carrier.

The root mean square (rms) modulation index for a channel can be defined as

$$m_{\text{rms},i} = \frac{m_i}{\sqrt{2}} \quad (2.6)$$

and the total rms modulation index  $\mu$  can be written as [28]

$$\mu^2 = \sum_{i=1}^N m_{\text{rms},i}^2 = \sum_{i=1}^N \frac{m_i^2}{2} \quad (2.7)$$

In the case where the peak modulation index  $m_i$  is the same for all channels, the total rms modulation index becomes

$$\mu = \sqrt{\frac{Nm^2}{2}} \quad (2.8)$$

where  $m = m_i$ .

### 2.2.2 Gaussian Noise

In single-laser lightwave SCM systems that do not employ optical amplifiers, there are three main sources of Gaussian noise [29]: front-end thermal noise, shot noise, and relative intensity noise (RIN). The qualitative analysis of these types of noise can be performed in terms of equivalent currents at the output of the photodetector in the receiver. The equivalent circuit for an optical receiver is shown in Figure 2.6, and includes another current source to represent the signal current that is generated by the PIN photodetector. The signal and noise current sources have an additive relationship as shown in the circuit diagram.

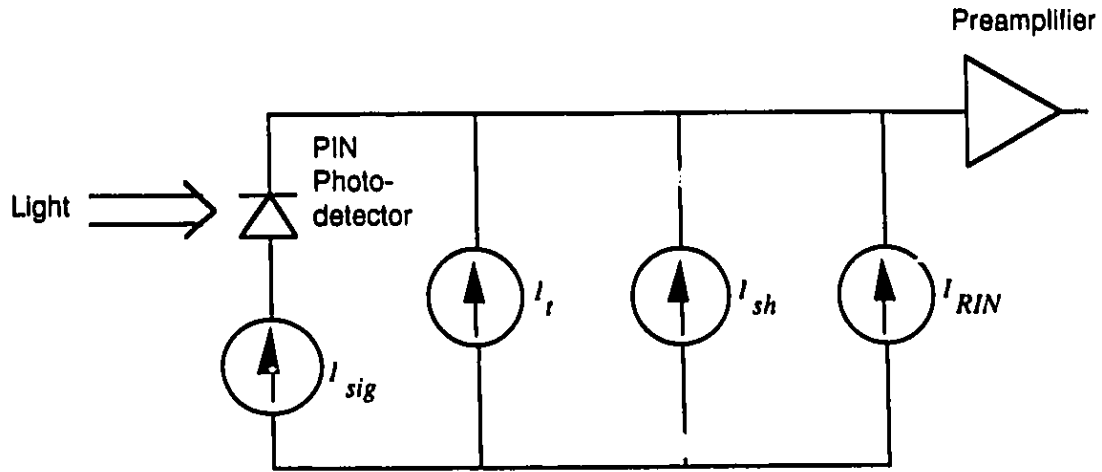


Figure 2.6: Noise Equivalent Circuit for an Optical Receiver

#### 2.2.2.1 Front-End Thermal Noise

Thermal noise generated in the receiver front-end by a preamplifier can be converted to an equivalent mean square input current expressed in  $A^2$  [29]:

$$\langle i_t^2 \rangle = \frac{4kTFB}{R_{eq}} \quad (2.9)$$

where  $k$  is Boltzmann's constant,  $T$  is the absolute temperature,  $F$  is the noise factor of the preamplifier,  $B$  is the receiver effective bandwidth, and  $R_{eq}$  is the equivalent resistance of the photodiode load.

#### 2.2.2.2 Shot Noise

Shot noise results from the quantum nature of light and can be represented by the following mean square current [29]:

$$\langle i_{sh}^2 \rangle = 2q\mathcal{R}P_oB \quad (2.10)$$

where  $q$  is the electronic charge,  $\mathcal{R}$  is the detector responsivity (in Amps/Watt), and  $P_o$  is the average received optical power.

### 2.2.2.3 RIN Noise

Even at a constant bias current, the output light of any semiconductor laser will exhibit intensity and phase fluctuations which are classified generally as relative intensity noise (RIN). The equivalent mean square photocurrent of RIN noise at the photodetector in the receiver can be represented by [29]

$$\langle i_{RIN}^2 \rangle = RIN(\mathcal{R}P_o)^2 B \quad (2.11)$$

where RIN is defined by [27]

$$RIN = \frac{\langle \Delta P_L^2 \rangle}{P_L^2} \quad (2.12)$$

where  $\langle \Delta P_L^2 \rangle$  is the mean square fluctuation of the laser output intensity and  $\overline{P_L^2}$  is the average intensity.

### 2.2.2.4 Carrier-to-Noise Ratio (CNR)

The performance of analog systems with respect to sources of Gaussian noise is measured by the ratio of the rms carrier power to rms noise power [27]. The Carrier-to-Noise Ratio (CNR) is given by

$$CNR = \frac{\langle i_{sig}^2 \rangle}{\langle i_i^2 \rangle + \langle i_{sh}^2 \rangle + \langle i_{RIN}^2 \rangle} \quad (2.13)$$



where  $\langle i_{sig}^2 \rangle$  is the mean square signal current and, for the case of an AM-VSB carrier, is expressed as

$$\langle i_{sig}^2 \rangle = \frac{1}{2} (m_i \mathcal{R} P_o)^2 \quad (2.14)$$

Substituting equations (2.9), (2.10), (2.11), and (2.14) into equation (2.13), we can express the CNR as

$$CNR = \frac{\frac{1}{2} (m_i \mathcal{R} P_o)^2}{\frac{4kTFB}{R_{eq}} + 2q\mathcal{R} P_o B + RIN (\mathcal{R} P_o)^2 B} \quad (2.15)$$

### 2.2.3 Nonlinear Distortion

The concept of nonlinear distortion can be illustrated by considering a system which accepts an input signal,  $x(t)$ , and generates an output signal,  $y(t)$ , as shown in Figure 2.7. In a practical communication system, the output is usually a function of the input:

$$y(t) = f(x(t)) \quad (2.16)$$

where  $f(\bullet)$  is the transfer function of the system as shown in Figure 2.8.



**Figure 2.7: A System with Input  $x(t)$  and Output  $y(t)$**

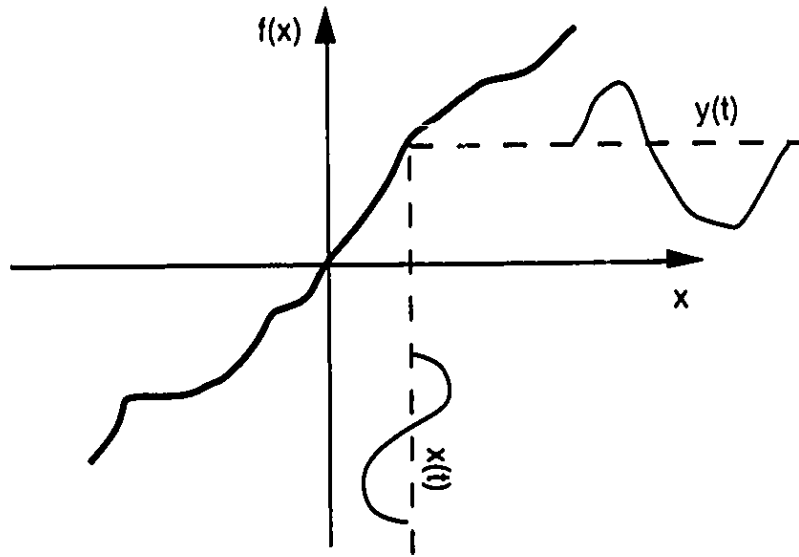


**Figure 2.8: System Transfer Function**

By using a Taylor series expansion, the output signal can be expressed in terms of powers of the input signal by expanding the system transfer function about the bias point. For example, if the system input was biased at  $x = 0$ , the output could be represented by [29], [30]

$$y(t) = \sum_{n=0}^{\infty} \frac{d^n f(0)}{dx^n} \frac{x^n(t)}{n!} = f(0) + \frac{df(0)}{dx} x(t) + \frac{1}{2!} \frac{d^2 f(0)}{dx^2} x^2(t) + \dots \quad (2.17)$$

In an ideal AM-VSB system, the signal produced at the receiver,  $y(t)$ , would have a linear relationship with the original signal at the transmitter,  $x(t)$ , such that

$$y(t) = c_1 + c_2 \cdot x(t) \quad (2.18)$$

where  $c_1$  and  $c_2$  are constants. It can be seen by comparing equations (2.17) and (2.18) that a deviation from linearity can result when the higher order terms in the expansion of the

system transfer function are non-zero. Nonlinear distortion can also be caused by a dynamic behavior of the transfer function  $f(\bullet)$  if it changes over time.

In a practical system, the departure from linearity is caused by many factors including nonideal performance of the RF circuitry in the transmitter and receiver, fiber transmission nonlinearities, and laser diode nonlinearities. Nonlinearities in fiber transmission are principally due to reflections in the optical link and the effects of fiber dispersion [26]. Laser diode nonlinearities originate from the dynamic response and static characteristics of semiconductor lasers [23]. The dynamic response is governed by the photon-electron interaction mechanism inside the laser cavity and can be evaluated by the laser rate equations which are intrinsically nonlinear. Sources of distortion due to the static characteristics of semiconductor lasers include small departures from linearity in the region above the threshold current on the laser power-versus-current curve. The laser threshold characteristic is also a source of nonlinearity, and is the focus of this study.

When multiple carrier frequencies pass through a nonlinear system, signal products other than the original frequencies can be produced. These undesirable signals are referred to as *intermodulation products* and can severely impact the quality of CATV channels [27]. In many experimental CATV systems, the intermodulation products are observed to spread over the entire CATV frequency band as shown in Figure 2.9 [9]. Intermodulation distortion arises from the interaction between two or more different subcarrier frequencies, and the most dominant types are second order and third order distortion. Intermodulation between two different frequencies  $f_1$  and  $f_2$  results in second order distortion products appearing in the frequency domain at  $|f_1 \pm f_2|$  and two tone third order products at  $|2f_1 \pm f_2|$  and  $|2f_2 \pm f_1|$ . Intermodulation between three different frequencies  $f_1$ ,  $f_2$ , and  $f_3$  results in third order distortion products at  $|f_1 \pm f_2 \pm f_3|$ .

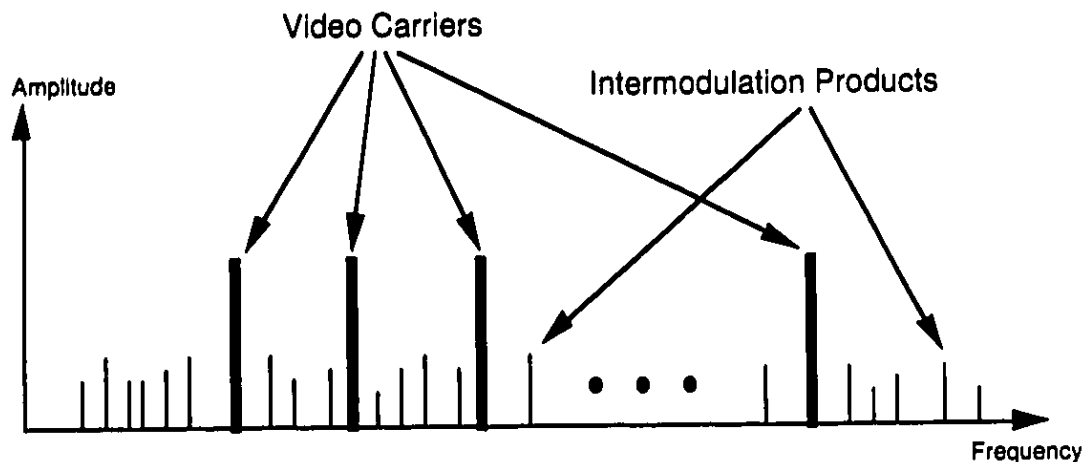


**Figure 2.9: Intermodulation Products in the CATV Frequency Band**

If the original SCM signal contains a large number of equally spaced carriers, several of the intermodulation products will land at or near the same frequency and will be additive on a power basis. This effect is referred to as *beat stacking* and results in distinct frequencies within each 6 MHz CATV channel bandwidth at which second order and third order distortion dominate. The Composite-Second-Order (CSO) distortion is defined as the ratio of carrier power to the total power of the largest second order beat stack within a particular channel [31]. Similarly, the Composite-Triple-Beat (CTB) distortion is defined as the ratio of carrier power to the total power of the largest third order beat stack. CSO and CTB are used as a measure of the performance of multichannel AM links and are specified in terms of dBc. For NTSC channel allocations, the CSO products land 1.25 MHz above or below the video carrier of a channel, and the CTB products land on the video carrier itself. Figure 2.10 shows an example of CSO, CTB, and other intermodulation beat stacks in a 6 MHz bandwidth [9].

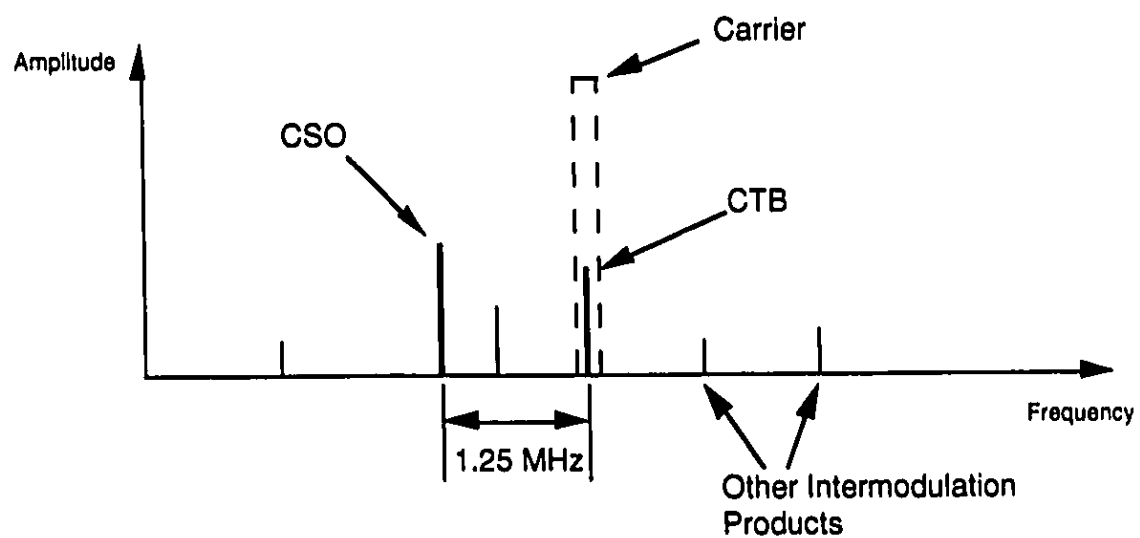


**Figure 2.10: CSO, CTB and Other Intermodulation Products in a CATV Channel**

### 3. A Model for Clipping-Induced Impulsive Noise

#### 3.1 Laser Characteristics

The technological progress of optical CATV systems has been quite rapid recently and has resulted in the development of lasers that are designed to meet the stringent linearity requirements of analog transmission. The noise and distortion requirements of directly-modulated AM-VSB systems have resulted in the preference of distributed feedback (DFB) lasers which have the important qualities of extremely low RIN noise, high output power, a highly linear power-current characteristic, and stable analog performance during aging [25], [32], [33]. The power-current characteristic, sometimes referred to as the *L-I curve*, for a typical CATV DFB laser is shown in Figure 3.1 [32], [34]. The L-I curve is shown to have three operating regions: the LED region, the linear lasing region, and the saturation region. When the drive current is below threshold, the spontaneous emission of photons occurs inside the laser cavity, and the laser acts as an edge-emitting light-emitting diode (LED). Stimulated emission is achieved when the input current is raised above threshold at which point the slope efficiency is significantly increased as the diode operates in the linear lasing region. Power saturation occurs at high output levels and is characterized by a downward curving section of the function.

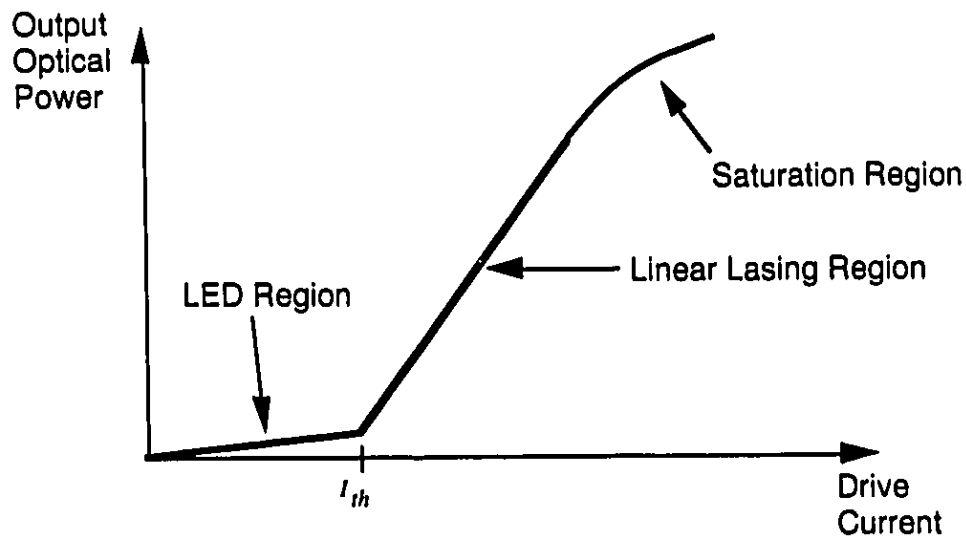


**Figure 3.1: L-I Curve for a Typical CATV Laser**

The analysis of nonlinear distortion generated by a CATV laser can become quite involved if one wishes to closely model the relationship between input current and output optical power of an actual laser. The dynamic effects of photon-electron interaction when the laser is modulated can be accounted for by using the semiconductor laser rate equations as the basis for analysis [35]. In the interest of minimizing the mathematical complexity of the theoretical development in this thesis, the model for clipping-induced impulsive noise developed in this chapter is based on the assumption of an idealized CATV laser transfer characteristic as shown in Figure 3.2. The transfer function is static and assumed not to vary with time. This characteristic contains a flat region below the threshold current where no optical power is transmitted. When the drive current is above threshold, the laser output is assumed to be perfectly linear with the input. The effect of output saturation at the top of the curve is neglected as it is assumed that the bias current is sufficiently low and the rms modulation index of the SCM signal is small enough that the total drive current never reaches the saturation region.

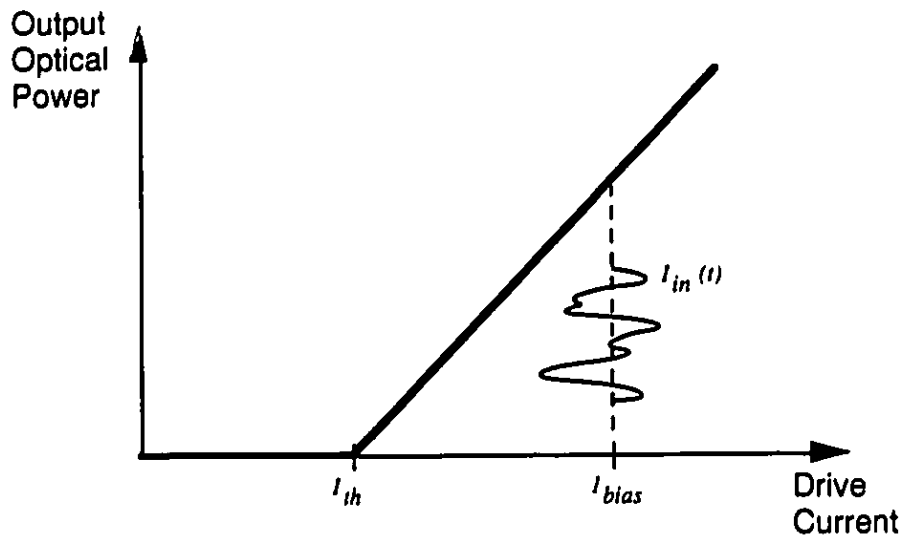


Figure 3.2: L-I Curve for an Ideal CATV Laser

### 3.2 Frequency Domain Analysis

In the past 6 years, many papers have been published with detailed analysis, including computer simulation and mathematical models, to predict the intermodulation distortion due to the laser threshold characteristic [28], [36]-[49]. An understanding of the relationship between the clipping mechanism and the CSO and CTB performance of an optical AM-VSB system is helpful in designing the system such that the highest possible modulating signal power is transmitted while meeting the nonlinear distortion requirements of the system. The nonlinear distortion requirements for a specific CATV system are usually specified by the maximum allowed CSO and CTB. In this section, a model for predicting the CSO and CTB, which was published by Shi *et al.* [43], is presented. The theory in this section is not new, but it is included in this thesis to provide a comparison with a novel time-based approach which is developed in Section 3.3.



### 3.2.1 Modeling the SCM Signal as a Gaussian Process

For an N-channel AM-VSB system, the total laser drive current  $I_{tot}(t)$  can be written as

$$I_{tot}(t) = I_{bias} + I_{in}(t) \quad (3.1)$$

where, as shown in Figure 3.2,  $I_{bias}$  is the constant bias current and  $I_{in}(t)$  is the modulating portion of the drive current and can be written as

$$I_{in}(t) = \sum_{i=1}^N I_{peak} \cos(2\pi f_i t + \theta_i) = \sum_{i=1}^N m(I_{bias} - I_{th}) \cos(2\pi f_i t + \theta_i) \quad (3.2)$$

where  $\theta_i$  is a random variable uniformly distributed over the interval  $[0, 2\pi]$ , and  $I_{peak}$  is the peak amplitude of each carrier expressed in terms of current. In the equation above, it is assumed that all carriers have the same peak modulation index  $m$ . In the clipping condition, the total drive current  $I_{tot}(t)$  can fall below the threshold current  $I_{th}$ . This can only occur if  $N \cdot I_{peak} > (I_{bias} - I_{th})$  or, equivalently,  $Nm > 1$ .

When the number of channels  $N$  becomes large and tends to infinity, the individual carriers can be modeled as statistically independent random processes having zero mean and a variance of  $I_{peak}^2/2$ . Because  $I_{in}(t)$  represents a sum of these random processes, it can be modeled as a Gaussian random process by the Central Limit Theorem [28]. The mean of this process is zero, and its variance  $\sigma_{in}^2$  is the sum of the variances of the individual carriers:

$$\sigma_{in}^2 = N \frac{I_{peak}^2}{2} = N \frac{(m(I_{bias} - I_{th}))^2}{2} = \mu^2 (I_{bias} - I_{th})^2 \quad (3.3)$$

where  $\mu$  is the total rms modulation index previously defined in equation (2.8).

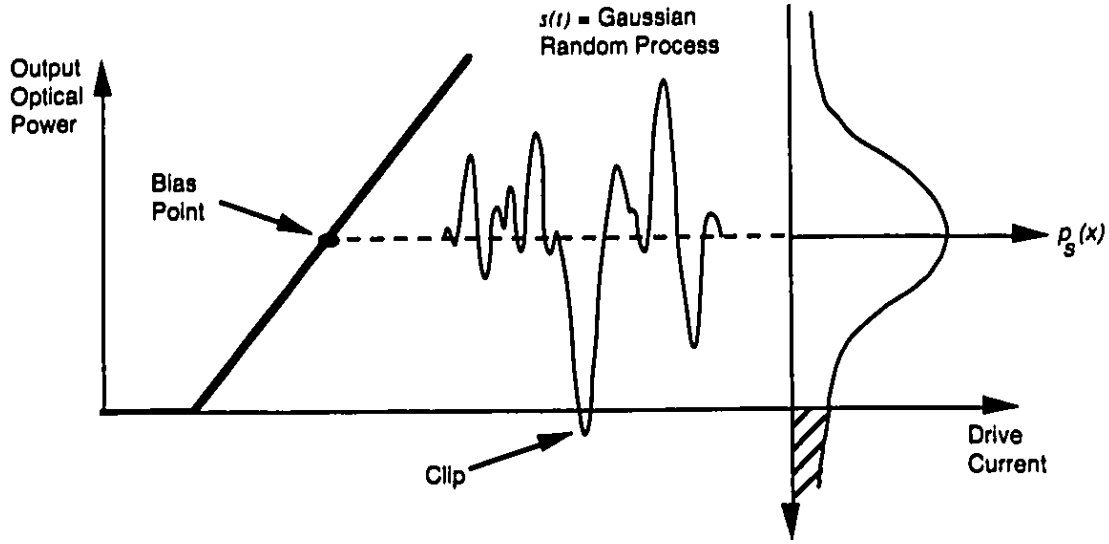


**Figure 3.3: Physical Representation of the Gaussian Approximation**

The physical representation of the Gaussian approximation is illustrated in Figure 3.3. The laser output power waveform is represented by a Gaussian random process  $s(t)$  which is centered about the constant bias point. The total output power is positive for the majority of the time, but, in the rare instance of a large excursion, can reach a value of zero and cause a clip to occur. The probability density of the amplitude of  $s(t)$  is illustrated in Figure 3.3 by the function  $p_s(x)$  and is represented by the well known equation [50]

$$p_s(x) = \frac{1}{\sqrt{2\pi}\sigma_s} \exp\left(-\frac{x^2}{2\sigma_s^2}\right) \quad (3.4)$$

where  $\sigma_s^2$  is the variance of  $s(t)$  and is given by

$$\sigma_s^2 = N \frac{P_{\text{peak}}^2}{2} = N \frac{(mP_{\text{bias}})^2}{2} = \mu^2 P_{\text{bias}}^2 \quad (3.5)$$

The region of interest in the Gaussian distribution is the lower tail where the amplitude of the sum of the bias point and  $s(t)$  falls below zero. Although the value of the probability density  $p_i(x)$  may be small in this region, it is still finite and indicates that clips will occur at some point in time. Because the output power stays at zero when the drive current falls below threshold, the transmitted optical waveform will have a value of zero for the duration of each clip.

The use of the Gaussian approximation was first proposed by Saleh [28], and has been used in most nonlinear distortion models. It should be noted, however, that the Gaussian approximation is limited by the extent to which its assumptions are valid. For example, the Central Limit Theorem applies to the case of an infinite sum of random processes, but, in an actual system, the number of carriers will be limited to  $N$  channels. Although it is generally accepted that the Gaussian approximation can be used for  $N > 10$ , the inaccuracies of the model with respect to the behavior of large excursions should be considered. While excursions in the SCM signal will never be larger than the sum of all the carrier amplitudes ( $|I_{in}(t)| < NI_{peak}$ ), for a Gaussian process there is always a finite probability of a large excursion, and this probability tends to zero for infinitely large excursions. Another discrepancy is also apparent when one considers that the Gaussian process is assumed to be a random process. In contrast, the SCM signal is a deterministic process which is governed by equation (3.2), and is, in fact, periodic in time. These inconsistencies provide a source of error when using the Gaussian assumption and could explain differences between theoretical predictions and the corresponding values measured in an experiment.

### 3.2.2 The Spectrum of a Clipped SCM Signal

The spectrum of a clipped SCM signal can be evaluated by examining the autocorrelation function of the laser input and output. The autocorrelation function of the

modulating current of equation (3.2) is given by [45]

$$R_{in}(\tau) = \frac{I}{2} I_{peak}^2 \sum_{i=1}^N \cos(2\pi f_i \tau) \quad (3.6)$$

When the signal is passed through a function  $g(\bullet)$ , which represents the laser threshold characteristic as shown in Figure 3.4, the output signal becomes a clipped version of the input. Under the Gaussian assumption, the autocorrelation function of the laser output relates to the input autocorrelation by a power series given by [43]

$$\begin{aligned} R_o(\tau) &= \sum_{k=0}^{\infty} \frac{h_k^2}{k!} \left[ \frac{R_{in}(\tau)}{\sigma_{in}^2} \right]^k \\ &= h_0^2 + h_1^2 \frac{R_{in}(\tau)}{\sigma_{in}^2} + \frac{1}{2} h_2^2 \left[ \frac{R_{in}(\tau)}{\sigma_{in}^2} \right]^2 + \frac{1}{6} h_3^2 \left[ \frac{R_{in}(\tau)}{\sigma_{in}^2} \right]^3 + \dots \end{aligned} \quad (3.7)$$

with coefficients  $h_k$  given by

$$h_k = \frac{1}{\sqrt{2\pi}\sigma_{in}} \int_{-\infty}^{\infty} g(x) H_k \left( \frac{x}{\sigma_{in}} \right) \exp \left( -\frac{x^2}{2\sigma_{in}^2} \right) dx \quad (3.8)$$

where  $H_k(\bullet)$  is the  $k^{\text{th}}$  order Hermite function and  $\sigma_{in}^2$  is the variance of the Gaussian process.

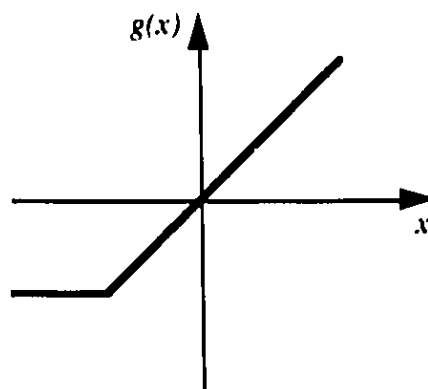


Figure 3.4: The Function  $g(x)$

It is well known that the power spectral density of a stationary stochastic process is given by the Fourier Transform of its autocorrelation function [50]. Therefore, the power spectral density of the clipped output signal can be derived by taking the Fourier Transform of equation (3.7). By taking the Fourier Transform of each of the additive terms in (3.7) individually, we can see that the second term represents the original input signal and the higher order terms represent clipping nonlinear distortion. The higher order terms contain powers of  $R_{in}(\tau)$  and, because  $R_{in}(\tau)$  is a sum of cosines at different frequencies, these terms can be multiplied out to show the contribution at specific intermodulation frequencies. As an example, the expansion of the second order term for the case of  $N = 2$  channels would give

$$\begin{aligned}
 \frac{1}{2} h_2^2 \left[ \frac{R_{in}(\tau)}{\sigma_{in}^2} \right]^2 &= \frac{1}{2} h_2^2 \left[ \frac{1}{2\sigma_{in}^2} I_{peak}^2 (\cos(2\pi f_1 \tau) + \cos(2\pi f_2 \tau)) \right]^2 \\
 &= \frac{1}{2} h_2^2 \left( \frac{I_{peak}^2}{2\sigma_{in}^2} \right)^2 \left[ \cos^2(2\pi f_1 \tau) + 2\cos(2\pi f_1 \tau)\cos(2\pi f_2 \tau) \right. \\
 &\quad \left. + \cos^2(2\pi f_2 \tau) \right] \tag{3.9} \\
 &= \frac{1}{2} h_2^2 \left( \frac{I_{peak}^2}{2\sigma_{in}^2} \right)^2 \left[ \cos^2(2\pi f_1 \tau) + \cos^2(2\pi f_2 \tau) \right. \\
 &\quad \left. + \cos(2\pi(f_1 + f_2)\tau) + \cos(2\pi(f_1 - f_2)\tau) \right]
 \end{aligned}$$

The two latter terms in the final expression show the contribution at the  $|f_1 \pm f_2|$  intermodulation frequencies.

By substituting (3.6) into (3.7), expanding the higher order terms, taking the Fourier Transform, and collecting the terms that appear at the CSO and CTB frequencies, generalized expressions for CSO and CTB can be derived. These expressions are [43]

$$CSO = \frac{K_{2v}}{8\pi N} \exp\left(\frac{-2}{m^2 N}\right) \gamma^{-2} \quad (3.10)$$

$$CTB = \frac{K_{3v}}{16\pi N^3} m^{-2} \exp\left(\frac{-2}{m^2 N}\right) \gamma^{-2} \quad (3.11)$$

where  $\gamma^{-2} = (1 + \operatorname{erf}(1/m\sqrt{N}))/2$ .  $K_{2v}$  and  $K_{3v}$  are, respectively, the second and third order power product count at frequency  $v$ .

### 3.3 Time Domain Analysis

Although there has been considerable effort in analytically determining the frequency spectrum of a clipped SCM signal, only a couple of recent papers have applied an analysis of a clipped SCM signal in the time domain [19], [47]. The theoretical analysis in this section was developed concurrently with these recently published works and contains many similar qualitative arguments and mathematical results of [19]. The use of a time domain approach in this thesis is motivated by the search for a qualitative understanding of the relationship between the clipping mechanism at the transmitter and the resulting impulsive noise seen at the receiver. An understanding of this relationship would be helpful in characterizing the behavior of clipping-induced impulsive noise in a CATV channel and could be used to predict the Bit Error Ratio (BER) performance of a digitally modulated channel in a hybrid analog/digital SCM system.

### 3.3.1 The Clipped Signal as a Sum of Two Signals

The first step in a time-based analysis of clipping distortion is to represent the clipped signal as a sum of two signals: the "desired" signal and an "error" signal. The error signal is equivalent to the negative of the desired signal when the desired signal is below threshold and is zero otherwise. In Figure 3.5, the clipped, desired, and error signals are represented by  $c(t)$ ,  $d(t)$ , and  $e(t)$  respectively. For further insight, the equivalent power spectra of the three signals are shown below their time domain representations in Figure 3.5. As discussed in Sections 2.2.3 and 3.2, the spectrum of a clipped SCM signal contains intermodulation products distributed over a wide range of frequencies due to the nonlinearity of the laser threshold. Because, the desired signal is simply the original SCM modulating waveform, its contribution to the clipped signal spectrum is only at the carrier frequencies while the error signal accounts for the rest of the clipped signal spectrum. We can thus model the error signal as a wideband random process containing power at the intermodulation frequencies.

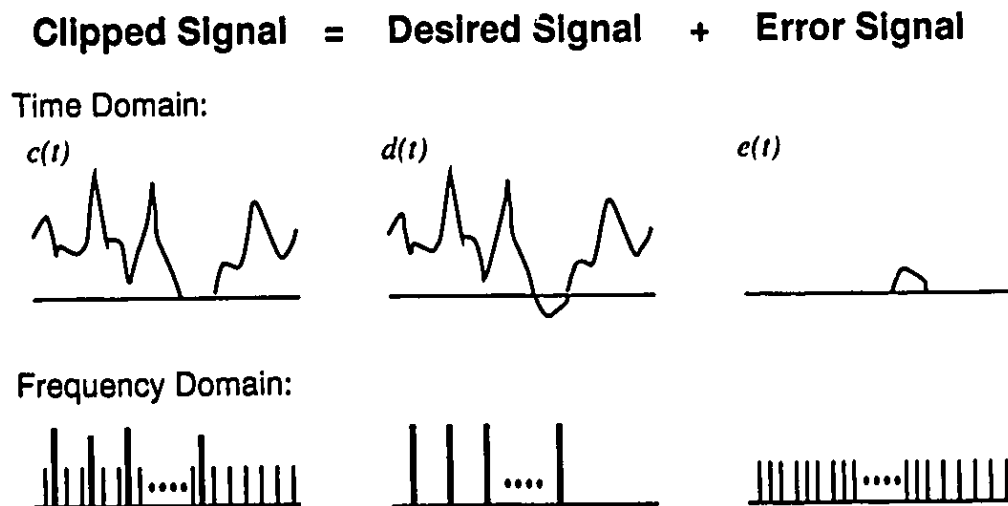


**Figure 3.5: The Clipped Signal as a Sum of Two Signals**

It should be noted that, because the error signal is correlated and, in fact, directly derived from the original desired SCM signal, the error process is not, in reality, an additive random noise source. However, it is mentioned by Mazo [44] that if the desired signal is written as the sum of the attenuated input and a noise  $e_m(t)$

$$c(t) = Kd(t) + e_m(t) \quad (3.12)$$

where  $K$  is the attenuation, then  $e_m(t)$  will become uncorrelated with  $d(t)$  as the magnitude of the difference between the clipping level current and the bias point current approaches infinity. Statistical properties of the level crossings for this asymptotic case, when the difference in current between the bias point and the clipping level is large, was studied many years ago by S.O. Rice [51], and three particularly useful results are discussed in the next section.

### 3.3.2 Asymptotic Clipping

The asymptotic clipping model is based on the representation of the SCM signal as a Gaussian random process. The probability of large excursions for the Gaussian process is very small and approaches zero for an infinitely large excursion. As the difference in current between the clipping level and the mean value of the Gaussian process becomes very large, it can be shown that, in the limit, excursions below the clipping level have the three following characteristics [44]:

- 1) The sequence of excursions becomes a Poisson process.
- 2) The probability density of the time  $\tau_p$  between any downcrossing and subsequent upcrossing becomes Rayleigh distributed.
- 3) The time dependence of the pulse between any downcrossing and subsequent upcrossing is, asymptotically, parabolic.



The fact that the sequence of downcrossing times approaches a Poisson process indicates that, in the limit of infinitely large excursions, the downcrossings become independent time events occurring at an average rate  $\lambda$ . If the spectrum of the Gaussian process is considered to be flat between the frequencies  $f_a$  and  $f_b$ , the expected rate of the Poisson downcrossings  $\lambda$  is given by [44], [51]

$$\lambda = \left[ \frac{f_b^3 - f_a^3}{3(f_b - f_a)} \right]^{1/2} \exp\left(-\frac{1}{2\mu^2}\right) \quad (3.13)$$

where  $\mu$  is the total rms modulation index of the SCM signal as defined in equation (2.8). In Figure 3.6,  $\lambda$  is plotted as a function of peak modulation index per channel for system containing the first 42 channels of the NTSC frequency plan ( $f_a = 55.25\text{MHz}$  and  $f_b = 337.25\text{MHz}$ ).

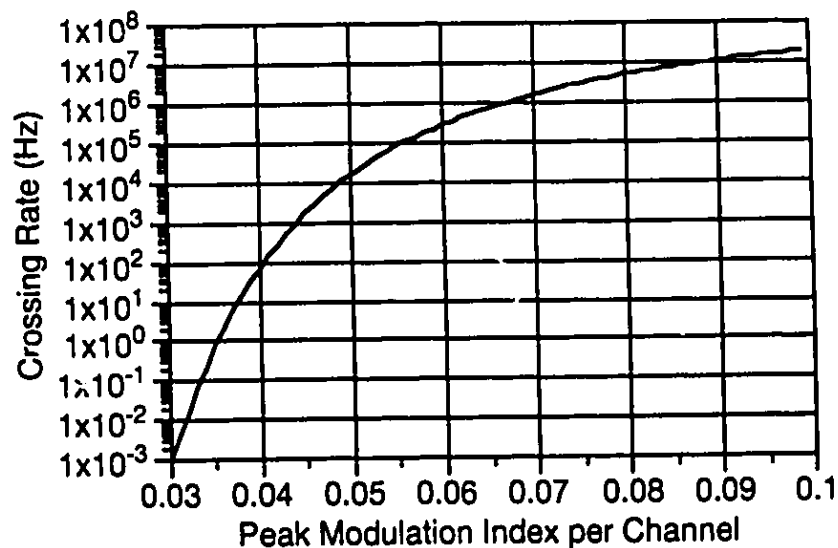


**Figure 3.6: Downcrossing Rate vs. Modulation Index for a 42 Channel System**

The probability density of the time duration of each excursion  $\tau_p$  is given by the following Rayleigh distribution [44]:

$$p(\tau_p) = \begin{cases} \frac{\pi}{2} \frac{\tau_p}{\bar{\tau}_p^2} \exp\left[-\frac{\pi}{4} \left[\frac{\tau_p}{\bar{\tau}_p}\right]^2\right] & , \tau_p \geq 0 \\ 0 & , \tau_p < 0 \end{cases} \quad (3.14)$$

where  $\bar{\tau}_p$  is the average time duration and is related to the clipping rate  $\lambda$  by [44]

$$\bar{\tau}_p = \frac{1}{2\lambda} \operatorname{erfc}\left(\sqrt{\frac{1}{2\mu^2}}\right) \quad (3.15)$$

In Figure 3.7,  $\bar{\tau}_p$  is plotted as a function of the peak modulation index per channel and is shown to range between 200 to 800 picoseconds for modulation indices of 0.03 to 0.1. For a typical modulation index of  $m = 0.04$ , the average duration is  $\bar{\tau}_p = 334 \text{ ps}$  and the Rayleigh probability density of  $\tau_p$  is shown in Figure 3.8.

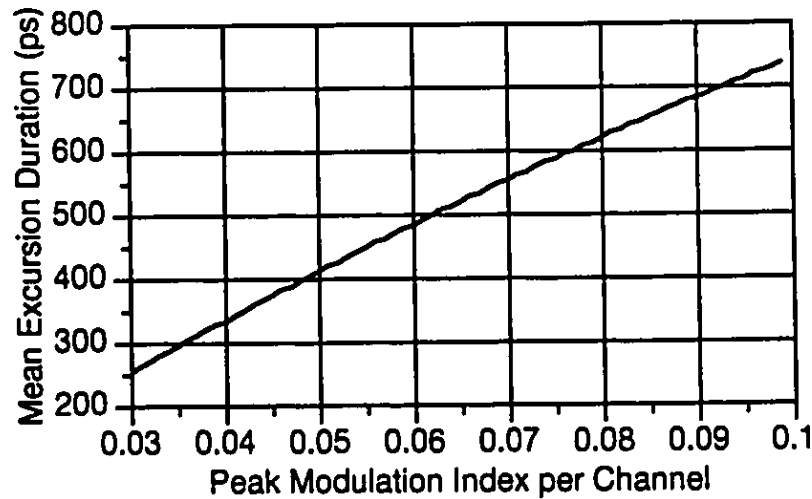


**Figure 3.7: Mean Excursion Duration vs. Modulation Index for a 42 Channel System**

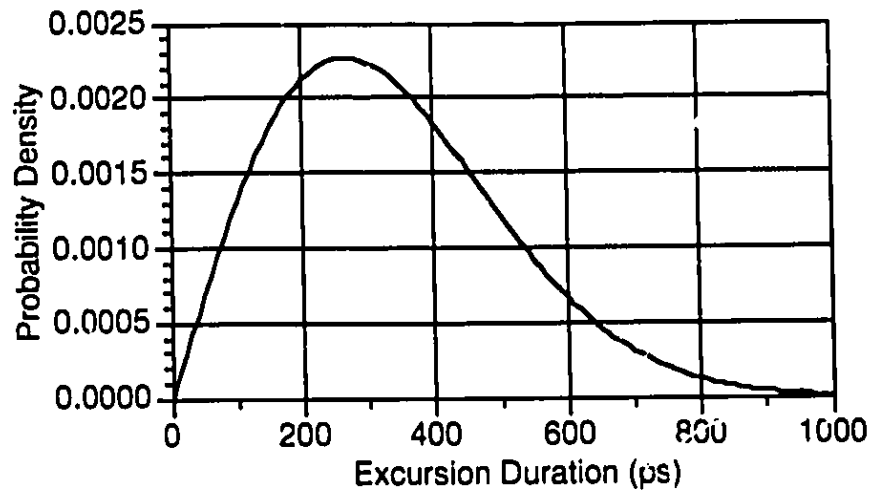


**Figure 3.8: Probability Density of Excursion Duration for  $m=0.04$**

Using the three properties of asymptotic clipping discussed in this section, the error process can be modeled as a sequence of parabolic pulses in the time domain occurring at a Poisson rate with pulse duration following a Rayleigh distribution as shown in Figure 3.9.

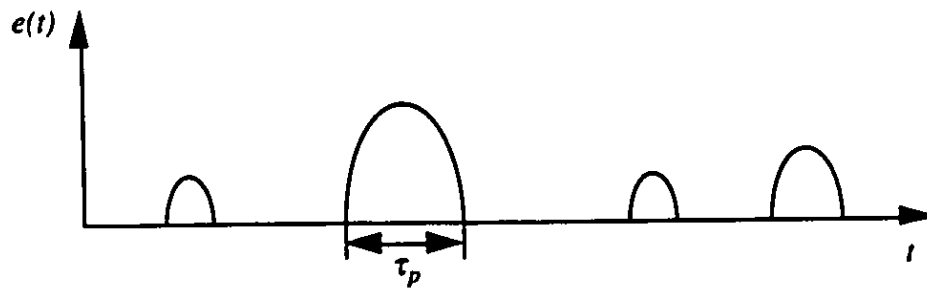


**Figure 3.9: The Error Process**

### 3.3.3 Filtering the Clipped SCM Signal

The BER degradation of a digital channel in an analog/digital hybrid system is caused by the additive noise in the digital channel. In an actual system, the additive noise waveform can be observed by connecting an oscilloscope to the channel output and turning

the channel off at the transmitter [9], [10], [13]. In the interest of predicting the output noise waveform when laser clipping is the dominant source of noise in the system, we investigate the effect of filtering the subcarrier multiplexed signal after it has been clipped by the laser threshold. This analysis of a clipped and filtered SCM signal will lead to an understanding of how impulsive noise generated by laser clipping is processed by the channel filters in the optical receiver, and how this bandlimited impulsive noise impacts on the BER of digital signals.

### 3.3.3.1 Qualitative Analysis: Bandlimiting Effect of a Bandpass Filter

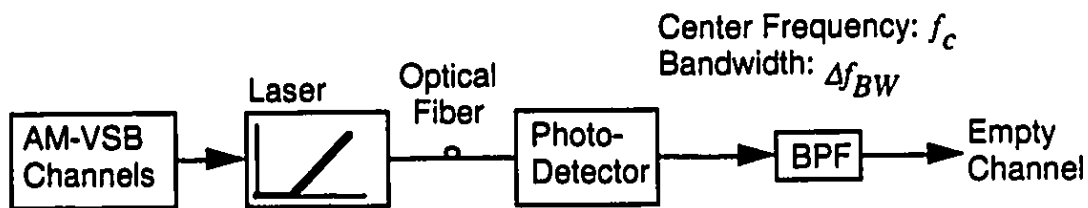


**Figure 3.10: System Model of Clipped and Filtered Signal**

A diagram of the system model is shown in Figure 3.10. The AM-VSB signal modulates a laser with an ideal threshold characteristic, and the clipped signal is received at the photodetector. For the purpose of illustration, it is assumed that the filter is a bandpass filter (BPF) with a center frequency of  $f_c$  and a bandwidth of  $\Delta f_{BW}$ . Figure 3.11 shows the spectrum of the original SCM signal and the passband of the BPF at the receiver. It is assumed that none of the subcarrier frequencies land in the filter passband, and only intermodulation products pass through.

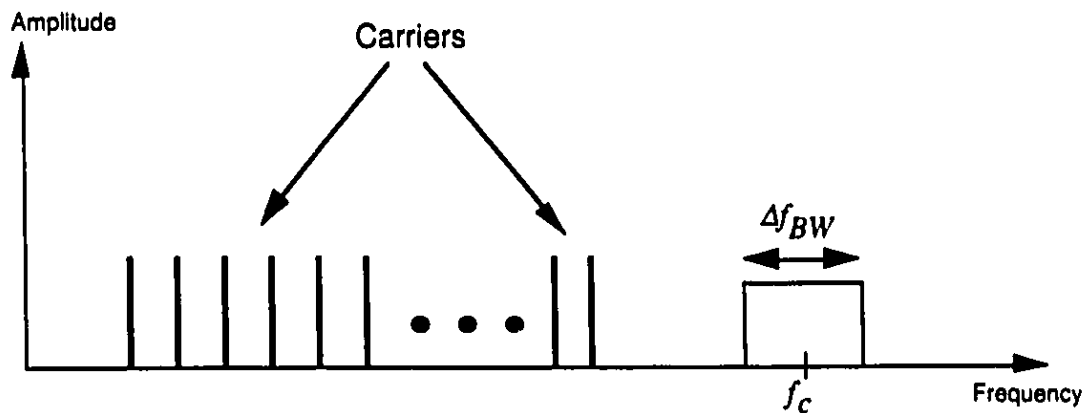


**Figure 3.11: SCM Spectrum and BPF Passband**

At this point, it is useful to consider the representation of the clipped signal as the sum of the desired signal and the error signal. Because the BPF is a linear system, the principle of superposition applies, and the effect of the desired signal and the error signal can be considered individually and then summed at the output [52]. The representation of the clipped, desired, and error signals as they pass through the BPF is shown in Figure 3.12. Because the desired signal is simply the unclipped version of the SCM signal, it does not contain any frequencies which land inside the filter bandwidth and therefore does not contribute to the filter output. As a pulse from the error signal passes through the filter, it causes a transient response at the output which will eventually decay over time. The transient response waveform is determined by the filter impulse response function and the input pulse shape and time duration. Because the error signal is the only constituent of the clipped signal that contributes to the filter output, the filter response to the clipped signal can be determined by simply examining the filter response to the error signal.

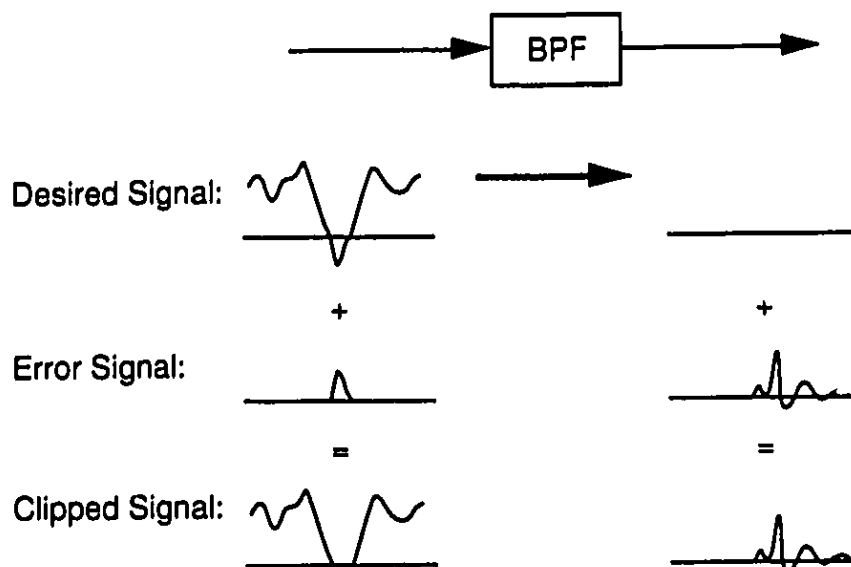


**Figure 3.12: Response of the BPF to the Clipped Signal**

As mentioned in the previous section, the error process in the asymptotic clipping case can be modeled as a Poisson impulse train with pulse duration following a Rayleigh density and shape following a parabola. The time domain and frequency domain representations of the error process at the input and output of the BPF are shown in Figure 3.13. The frequency spectrum of the input error process consists of the intermodulation products which are spread over the entire CATV band. Each pulse at the input of the BPF causes a corresponding output transient response in the time domain. In the frequency domain, this is equivalent to reducing the bandwidth of the error process to  $\Delta f_{BW}$ . Considering the alterations of the error process as it passes through the bandpass filter in Figure 3.13, it is readily apparent that the effect of the filter is to change the wideband error process into a narrowband noise process. This narrowband noise process consists of a sequence of filter transient responses which are stimulated by the sequence of parabolas at the input. Because the duration of each transient response may be longer than the time between input parabolas, the output transient responses may be superimposed onto each other in the output waveform. It is suggested that this narrowband noise process may have

impulsive characteristics and may resemble the impulsive noise that has been observed in previous experiments [9], [10], [13].

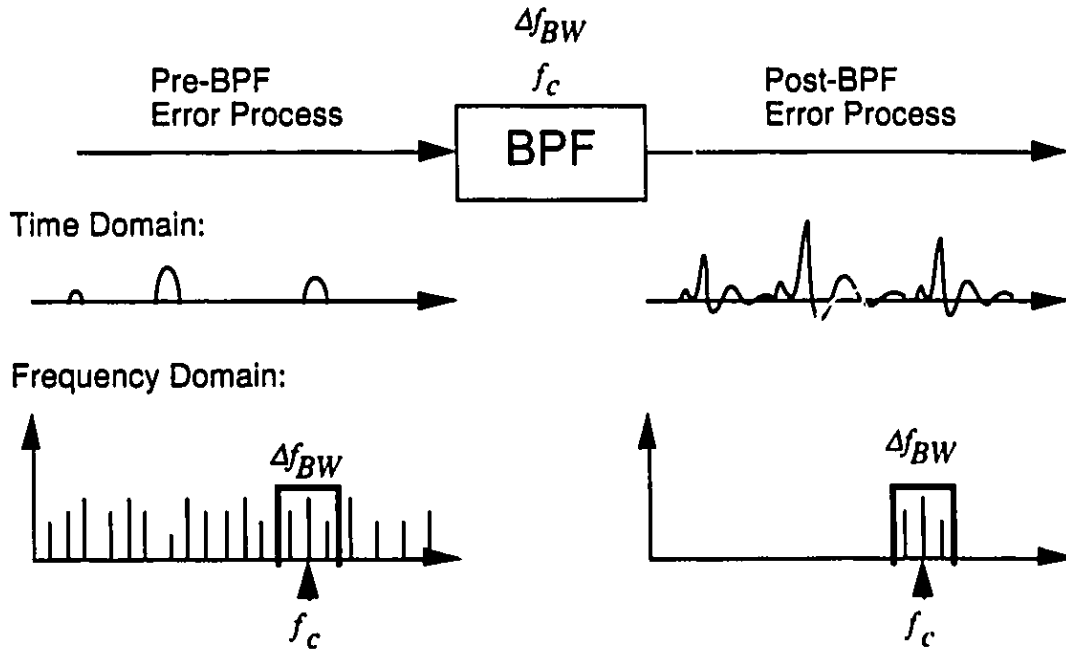


**Figure 3.13: Response of the BPF to the Error Signal**

### 3.3.3.2 Quantitative Analysis: The Response at the Filter Output

Although the response of a bandpass filter to a parabolic input pulse can be determined using common signal analysis techniques, it was determined, during the course of this work, that the mathematical expressions for the noise process at the filter output become quite complex. To simplify the mathematical development of a clipping-induced impulsive noise model, the input parabolic pulses are modeled as impulse functions with the same area as the parabolic pulses. The validity of this approximation is discussed in Appendix B.

Using the impulse approximation, the error process can be mathematically

represented by

$$e(t) = \sum_{k=-\infty}^{\infty} A_k \delta(t - t_k) \quad (3.16)$$

where  $\delta(\bullet)$  is the impulse (or Dirac delta) function,  $t_k$  are Poisson distributed event times, and  $A_k$  are random variables representing the parabola area. The amplitude and area of each parabola are, respectively, proportional to the square and cube of the time duration  $\tau_p$ . Because  $\tau_p$  has a random Rayleigh distribution given by equation (3.14), the random distribution of  $A$ , as shown in the Appendix, has the following form:

$$p(A) = \begin{cases} \frac{2}{3} \frac{c}{A^{1/3}} \exp[-c A^{2/3}] & , A > 0 \\ 0 & , A \leq 0 \end{cases} \quad (3.17)$$

where

$$c = \left( \frac{6}{\overline{A^2}} \right)^{3/2} \quad (3.18)$$

and  $\overline{A^2}$  is the mean square value of  $A$ .

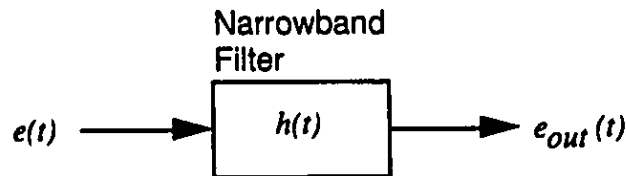


**Figure 3.14: Filtered Error Process**

The output of a narrowband filter placed after the receiver can be predicted with the filtered error process model shown in Figure 3.14. The input error process  $e(t)$  is given



by equation (3.16), and the output is simply the convolution of the input impulses with the filter impulse response  $h(t)$ :

$$e_{out}(t) = e(t) \otimes h(t) = \sum_{k=-\infty}^{\infty} A_k \delta(t - t_k) \otimes h(t) = \sum_{k=-\infty}^{\infty} A_k h(t - t_k) \quad (3.19)$$

where  $\otimes$  denotes the convolution operation. The output  $e_{out}(t)$  is a shot noise process. The shot noise waveforms are filter impulse responses weighted by the random value of  $A_k$ . By applying Rice's Shot Noise Model [53], [54], the characteristic function (or moment generating function) can be written as

$$M_{out}(jv) = \exp \left[ \lambda \int_{-\infty}^{\infty} \int_{-\infty}^{\infty} (e^{jvAh(t)} - 1) p(A) dA dt \right] \quad (3.20)$$

where  $\lambda$  is the average rate of events given by equation (3.13),  $p(A)$  is the probability density of  $A$  given by equation (3.17), and  $v$  is the characteristic function variable.

It is well known that the amplitude probability density of a specific process is given by the Inverse Fourier Transform of its characteristic function [50]. The amplitude probability density of  $e_{out}(t)$  is therefore given by

$$\begin{aligned} p(e_{out}) &= F^{-1}[M_{out}(jv)] = F^{-1} \left[ \exp \left( \lambda \int_{-\infty}^{\infty} \int_{-\infty}^{\infty} (e^{jvAh(t)} - 1) p(A) dA dt \right) \right] \\ &= \frac{1}{2\pi} \int_{-\infty}^{\infty} \exp \left( \lambda \int_{-\infty}^{\infty} \int_{-\infty}^{\infty} (e^{jvAh(t)} - 1) p(A) dA dt \right) e^{-jv\omega} dv \end{aligned} \quad (3.21)$$

In general, it is difficult to obtain a closed-form solution to the expression of equation (3.21). Depending on the nature of  $h(t)$ , some analytic simplifications may be possible in approximating the probability density function of  $e_{out}(t)$ . Computer programs

implementing numerical analysis techniques may also be used in evaluating equation (3.21).

To get an idea of what the impulse response waveform  $h(t)$  might look like, the BPF filter can modeled as an ideal filter with the following transfer function:

$$H_{BPF}(\omega) = \begin{cases} 1 & , |\omega - \omega_c| \leq \Delta\omega_{BW}/2 \\ 0 & , |\omega - \omega_c| > \Delta\omega_{BW}/2 \end{cases} \quad (3.22)$$

where  $\omega$  is the angular frequency,  $\omega_c = 2\pi f_c$ , and  $\Delta\omega_{BW} = 2\pi\Delta f_{BW}$ . The BPF can be used to represent a CATV channel filter with channel center frequency  $\omega_c$  and with channel bandwidth  $\Delta\omega_{BW}$ . The impulse response  $h_{BPF}(t)$  is given by the Inverse Fourier Transform of  $H_{BPF}(\omega)$  and consists of a cosine wave of frequency  $\omega_c$  with a sinc envelope [52]:

$$h_{BPF}(t) = F^{-1}[H_{BPF}(\omega)] = \frac{\Delta\omega_{BW}}{2\pi} \text{sinc}\left(\frac{\Delta\omega_{BW}t}{2\pi}\right) \cdot \frac{1}{\pi} \cos(\omega_c t) \quad (3.23)$$

To illustrate the nature of  $h_{BPF}(t)$ , the impulse response of an ideal filter is plotted in Figure 3.15 for the case of  $\omega_c = 2\pi(30\text{MHz})$  and  $\Delta\omega_{BW} = 2\pi(6\text{MHz})$ . In Figure 3.15, the amplitude has been normalized to have a unity peak value. If each parabolic pulse of the error process is approximated as an impulse, then the impulsive noise at the output of the BPF can be represented by the superposition of a sequence of impulse responses, which have a similar appearance to the waveform in Figure 3.15, occurring at random points in time. It is proposed that this representation is a close approximation to the impulsive noise waveforms that have been observed in recently published experiments [10], [13].

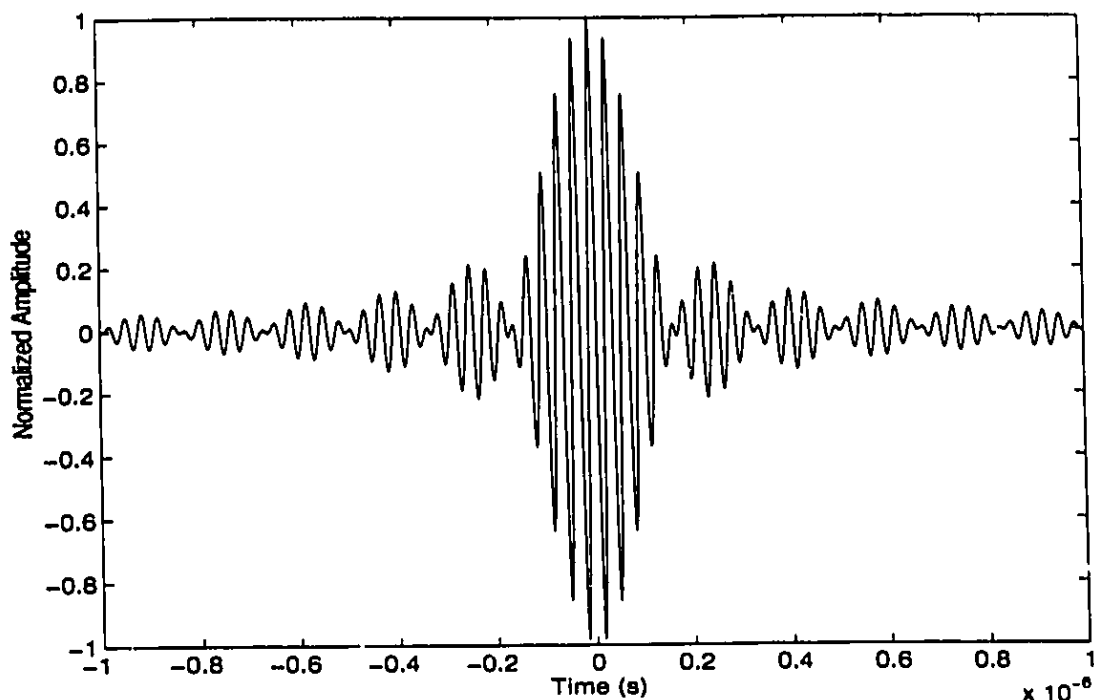


**Figure 3.15: Impulse Response of an Ideal BPF**

### **3.3.4 The Impact of Clipping on the Bit Error Ratio of an ASK Channel in a Hybrid AM-VSB/ASK System**

Hybrid optical transmission systems provide a way of transmitting traditional analog television channels simultaneously with digital channels containing HDTV or data. This format will likely be adopted in the transition period when HDTV is introduced in the cable television network [3]. Recent studies have demonstrated that laser diode clipping severely impacts the quality of the digitally modulated channels [10]-[14]. In this section, we develop a theoretical approximation for the BER of an Amplitude-Shift Keyed (ASK) channel in a hybrid AM-VSB/ASK system. Although the development assumes that the digital channels are ASK modulated, the analysis can readily be applied to other digital amplitude modulation schemes such as Quadrature Amplitude Modulation (QAM).

### 3.3.4.1 System Model

A typical AM-VSB/ASK hybrid system can be represented by the block diagram in Figure 3.16. In the system model, it is assumed that the laser transfer function has an ideal turn-on characteristic, and that the only source of nonlinear distortion in the system is from laser diode clipping. In an actual system, there will be other sources of nonlinear distortion such as resonance distortion, amplifier nonlinear gain, and the interaction between laser diode chirp and fiber dispersion. However, in the interest of studying the ASK performance in systems where clipping distortion is the dominant source of nonlinear distortion, these other effects will be neglected.

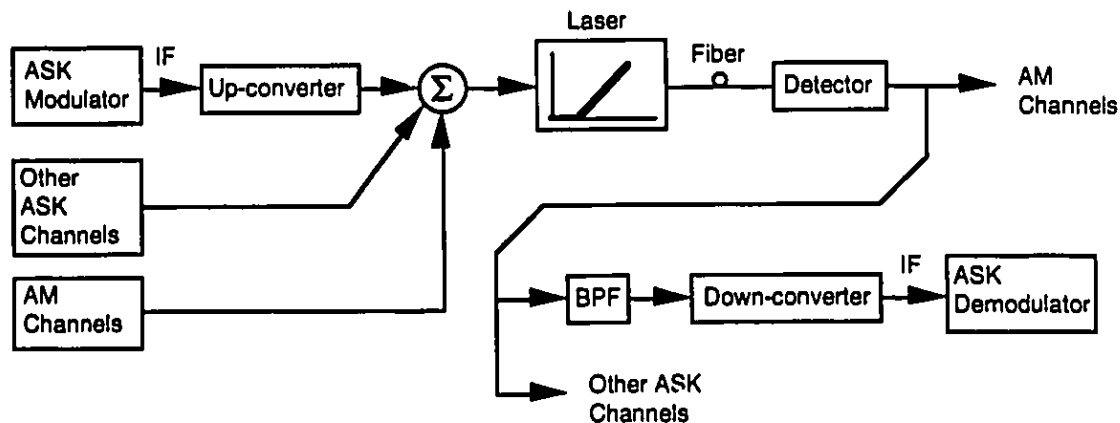


**Figure 3.16: Typical AM-VSB/ASK Hybrid System**

To determine how laser diode clipping affects the performance of an ASK channel, it is instructive to first consider the case when the laser output is not clipped. If the laser output is unclipped, the signal received at the detector is simply a frequency division multiplexed signal with the AM and ASK channels side-by-side in the frequency domain. Because the receiver for each ASK channel contains a bandpass filter which suppresses all frequencies outside of the ASK channel, the performance of a particular ASK channel does not depend on the presence or absence of the other channels. In other words, the

performance of the ASK channel would be the same if the AM channels and other ASK channels were removed from the system. The system model for this (unclipped) case is shown in Figure 3.17 with representations of the frequency spectrum at certain points in the system. The sources for the AM channels and the other ASK channels are drawn in dashed lines because they can be removed without affecting the performance of the ASK channel of interest.

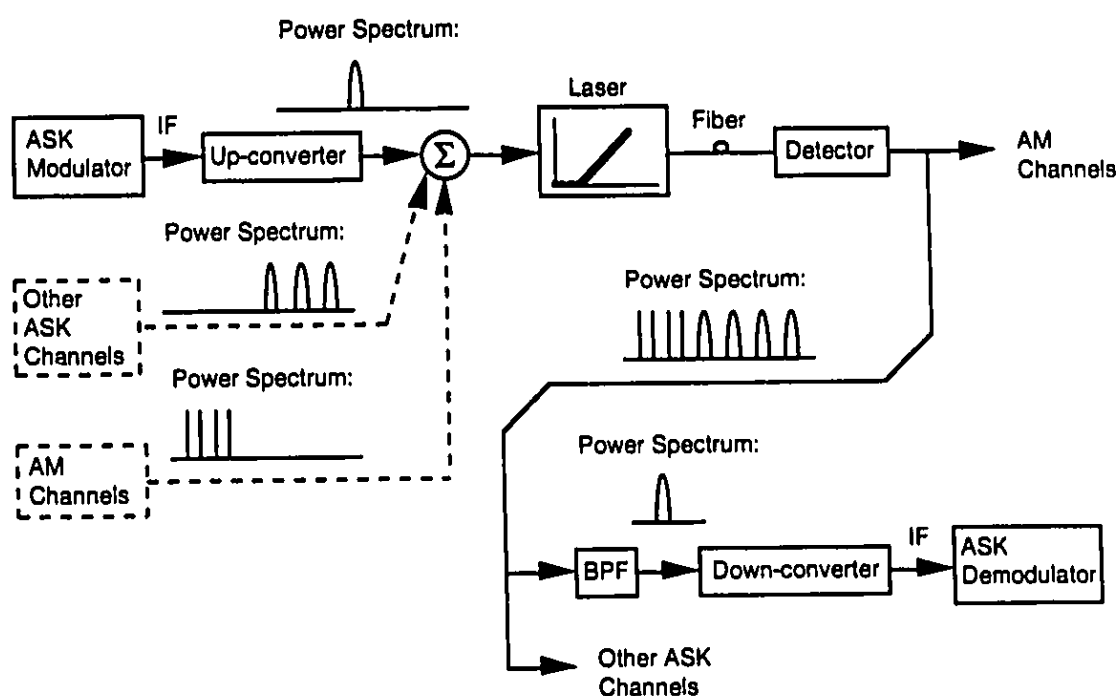


**Figure 3.17: Unclipped Case**

Considering that the diagram above applies only to the case where there is no clipping, the question arises: How can we account for the channel sources when there is clipping? From the discussion in Section 3.3.1, it was shown that the clipped signal at the laser output can be considered as the sum of a desired signal and an error signal. Because the clipped signal can be fully represented by the desired signal and the error signal, the laser can be removed from the system model by introducing an error signal source at the

transmitter. This modified model is shown in Figure 3.18 with the appropriate time domain representations of the signals in the system.

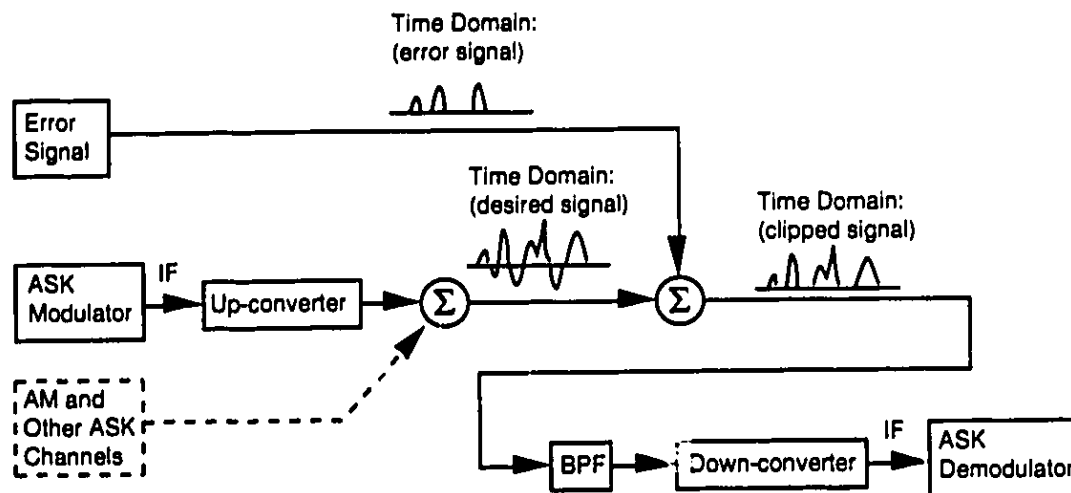


**Figure 3.18: Modified Model**

The advantage of representing the system with the model in Figure 3.18 becomes apparent when one considers that, as in the case of an unclipped laser output, the signal from the "AM and other ASK channels" source does not contain frequencies inside the ASK channel of interest and, thus, does not affect its performance. This source can in fact be removed from the model without affecting the results of the ASK channel analysis. The error signal source, however, cannot be removed because the error process contains power in a wide range of frequencies, and a portion of this spectral power is transmitted through the bandpass filter, degrading the performance of the ASK demodulator. The portion of the error signal spectrum that passes through the bandpass filter corresponds to the bandpass filtered impulses, generated by the nonlinear laser turn-on characteristic, that land inside the ASK channel.

### 3.3.4.2 Receiver Noise Analysis

In an M-ary ASK system, the  $m^{\text{th}}$  transmitted symbol is represented by [50]

$$s_m(t) = B_m u(t) \cos(\omega_{ASK} t) \quad (3.24)$$

where

$$B_m = 2m - 1 - M, \quad m = 1, 2, \dots, M, \quad (3.25)$$

$\omega_{ASK}$  is the frequency of the ASK channel, and  $u(t)$  is the pulse shape. To make  $s_m(t)$  in terms of photocurrent at the detector,  $u(t)$  is expressed in units of current, and the coefficient,  $B_m$ , is unitless. In this analysis, we assume that  $u(t)$  is symmetrical about  $t = 0$ , and is zero for  $|t| > T_u$  such that

$$s_m(t) = \begin{cases} B_m u(t) \cos(\omega_{ASK} t) & , -T_u < t < T_u \\ 0 & , \text{otherwise} \end{cases} \quad (3.26)$$

In a practical system, the shape of  $u(t)$  will generally not be rectangular because of the wide bandwidth required for rectangular pulses. To reduce the ASK channel bandwidth, the duration of the pulse ( $2T_u$ ) may be longer than the symbol period, but will have a shape that minimizes intersymbol interference (ISI) at the receiver. If the receiver decision circuit is assumed to sample at  $t = 0$ , then the baseband matched filter, which minimizes the effect of additive Gaussian noise, will have the following impulse response:

$$h_b(t) = \begin{cases} c_A u(t) & , -T_u < t < T_u \\ 0 & , \text{otherwise} \end{cases} \quad (3.27)$$

where  $c_h$  is a constant. The representation of the down-converter and the ASK demodulator is shown in Figure 3.19.

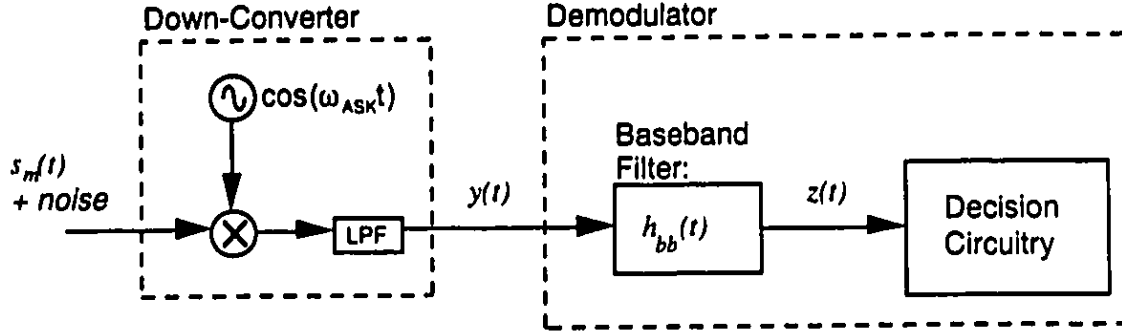


**Figure 3.19: Down-converter and Demodulator**

The input to the baseband filter,  $y(t)$ , will be the baseband version of the transmitted symbol and will be corrupted by the additive Gaussian and non-Gaussian noise in the transmission link:

$$y(t) = B_m u(t) + n_G(t) + n_I(t) \quad (3.28)$$

where  $n_G(t)$  and  $n_I(t)$  are sample functions of Gaussian and non-Gaussian noise currents at the filter input. At the output of the baseband filter,  $z(t)$  is sampled and the decision circuitry determines which of the  $M$  symbols were received at the sampling time. At the sampling time  $t = 0$ ,  $z(t)$  will be

$$z_m = y(t) \otimes h_{bb}(t) \Big|_{t=0} = B_m \int_{-\infty}^{\infty} u(\tau) h_{bb}(\tau) d\tau + N_G + N_I \quad (3.29)$$



where

$$\begin{aligned} N_G &= \int_{-\infty}^{\infty} n_G(\tau) h_{bb}(-\tau) d\tau = \int_{-\tau_s}^{\tau_s} n_G(\tau) h_{bb}(\tau) d\tau \\ N_I &= \int_{-\infty}^{\infty} n_I(\tau) h_{bb}(-\tau) d\tau = \int_{-\tau_s}^{\tau_s} n_I(\tau) h_{bb}(\tau) d\tau \end{aligned} \quad (3.30)$$

The random variables,  $N_G$  and  $N_I$ , cause symbol errors when

$$N_G + N_I > \int_{-\infty}^{\infty} u(\tau) h_{bb}(\tau) d\tau \quad (3.31)$$

and are characterized in the two following sections.

### 3.3.4.3 The Gaussian Noise Component

The variance of  $N_G$  in an optical system is (in units of  $A^2$ )

$$\sigma_G^2 = i_{th}^2 B + 2q(\mathcal{R}P_o)B + RIN(\mathcal{R}P_o)^2 B \quad (3.32)$$

where  $i_{th}^2$  is the receiver front-end thermal noise current spectral density,  $B$  is the noise equivalent bandwidth of the ASK channel, and the other variables are defined in Section 2.2.2. The characteristic function of  $N_G$  is [50]

$$M_G(jv) = e^{-\frac{v^2 \sigma_G^2}{2}} \quad (3.33)$$

### 3.3.4.4 The Impulsive Noise Component

To characterize the non-Gaussian noise component due to clipping-induced impulsive noise, it is instructive to examine the error signal response at the input to the

decision circuit in Figure 3.19. The impulses from the error process are multiplied by the oscillator tone in the down-converter and generate impulse responses at the baseband filter output. This process  $e_t(t)$  can be represented by

$$e_t(t) = \left[ \sum_{k=-\infty}^{\infty} A_k \delta(t - t_k) \cos(\omega_{ASK} t) \right] \otimes h_{bb}(t) = \sum_{k=-\infty}^{\infty} A_k \cos(\omega_{ASK} t_k) h_{bb}(t - t_k) \quad (3.34)$$

Because the event times  $t_k$  occur randomly in time, the  $\cos(\omega_{ASK} t_k)$  weighting factor for each impulse response is represented with a random variable  $F_\theta$  such that

$$e_t(t) = \sum_{k=-\infty}^{\infty} A_k F_\theta h_{bb}(t - t_k) \quad (3.35)$$

where

$$F_\theta = \cos(\theta) \\ p(\theta) = \begin{cases} \frac{1}{2\pi} & , 0 \leq \theta < 2\pi \\ 0 & , \text{otherwise} \end{cases} \quad (3.36)$$

The down-conversion process results in a characteristic function for  $N_t$  that requires a slight modification of equation (3.20):

$$M_t(j\nu) = \exp \left[ \lambda \int_{-\infty}^{\infty} \int_{-\infty}^{\infty} \int_{-\infty}^{\infty} (e^{j\nu A F_\theta h_{bb}(t)} - 1) p(\theta) p(A) dt d\theta dA \right] \quad (3.37)$$

If we consider the regions in which  $h_{bb}(t)$ ,  $A$ , and  $F_\theta$  have a value of zero, the limits of integration can be further defined:

$$M_t(j\nu) = \exp \left[ \lambda \int_0^{T_b} \int_0^{2\pi} \int_0^{T_b} (e^{j\nu A F_\theta h_{bb}(t)} - 1) p(\theta) p(A) dt d\theta dA \right] \quad (3.38)$$

If we introduce a new parameter called the clipping index  $\gamma$  [55] which represents the average number of clips in the interval  $[-T_u, T_u]$ , we can write  $M_I(j\nu)$  as

$$M_I(j\nu) = \exp \left[ \frac{\gamma}{2T_u} \int_0^{2\pi} \int_0^{T_u} \int_0^{T_u} (e^{j\nu A F_\theta h_{bb}(t)} - 1) p(\theta) p(A) dt d\theta dA \right] \quad (3.39)$$

where  $\gamma = \lambda \cdot (2T_u)$ . An approximation can be made in the case where  $\gamma \ll 1$  by expanding the outer exponential and neglecting higher order terms. The result is [56]

$$M_I(j\nu) \approx (1 - \gamma) + \frac{\gamma}{2T_u} \left[ \int_0^{2\pi} \int_0^{T_u} \int_0^{T_u} (e^{j\nu A F_\theta h_{bb}(t)}) p(\theta) p(A) dt d\theta dA \right] \quad (3.40)$$

Because  $p(\theta)$  is uniform between  $\theta = 0$  and  $\theta = 2\pi$ , the probability density of  $F_\theta = \cos(\theta)$  is symmetric about  $F_\theta = 0$ . Consequently, the imaginary part of the complex exponential in equation (3.40) does not contribute to  $M_I(j\nu)$  and we can write

$$\begin{aligned} M_I(j\nu) &\approx (1 - \gamma) + \frac{\gamma}{2T_u} \left[ \int_0^{2\pi} \int_0^{T_u} \int_0^{T_u} \cos(\nu A F_\theta h_{bb}(t)) p(\theta) p(A) dt d\theta dA \right] \\ &\approx (1 - \gamma) + \frac{\gamma}{2T_u} \left[ \int_0^{T_u} \int_0^{T_u} J_0(\nu A h_{bb}(t)) p(A) dt dA \right] \end{aligned} \quad (3.41)$$

where  $J_0$  is the 0<sup>th</sup> order Bessel function of the first kind.

The variance of  $N_I$  is then

$$\sigma_I^2 = \frac{\gamma}{2T_u} \overline{A^2} \frac{1}{2} \int_{-\infty}^{\infty} h_{bb}^2(\tau) d\tau = \lambda \overline{A^2} \cdot \frac{1}{2} \int_{-\infty}^{\infty} h_{bb}^2(\tau) d\tau \quad (3.42)$$

and is equivalent to the clipping-induced nonlinear distortion power that lands in the ASK channel bandwidth. A value for  $\sigma_I^2$  and can be calculated using various nonlinear distortion models [28], [36]-[49]. If the  $\sigma_I^2$ ,  $\lambda$ , and  $\hat{n}_{bb}(\tau)$  are known, equation (3.42) can be used to determine the appropriate value for  $\overline{A^2}$ .

### 3.3.4.5 Probability of Symbol and Bit Error

If we define the sum of the Gaussian and impulsive noise components to be,

$$N_T = N_G + N_I \quad (3.43)$$

then, because  $N_G$  and  $N_I$  are independent random variables, the characteristic function of  $N_T$  is [50]

$$M_T(j\nu) = M_G(j\nu) \cdot M_I(j\nu) \quad (3.44)$$

and the probability density of the combined noise process  $p(N_T)$  is given by the Inverse Fourier Transform of  $M_T(j\nu)$ .

The probability of a symbol error in an M-ary ASK system is

$$P_M = \frac{M-1}{M} P(|N_T| > d_{min}/2) = \frac{M-1}{M} \cdot 2 \cdot \int_{d_{min}/2}^{\infty} p(N_T) dN_T \quad (3.45)$$

where

$$\begin{aligned} d_{min}/2 &= \frac{\sqrt{2PF_{M,ASK}P_{ave}}}{M-1} \\ PF_{M,ASK} &= 3 \frac{M-1}{M+1} \\ P_{ave} &= (m_{ASK} \Re P_o)^2 / 2 \end{aligned} \quad (3.46)$$

where  $PF_{M,ASK}$  is the power factor for M-ary ASK,  $P_{ave}$  is the transmitted ASK power, and  $m_{ASK}$  is the effective ASK modulation index. Because a symbol represents  $\log_2 M$  bits, the probability of a bit error for a Gray-encoded system will be

$$P_e \approx \frac{2}{\log_2 M} \left(1 - \frac{1}{M}\right) \int_{d_{min}/2}^{\infty} p(n) dn = BER \quad (3.47)$$

### 3.3.4.6 Extending the Results to M-ary QAM

The probability of a symbol error in an M-ary QAM system is

$$P_M = 4 \left(1 - \frac{1}{\sqrt{M}}\right) \int_{d_{min}/2}^{\infty} p(n) dn \quad (3.48)$$

where

$$\begin{aligned} d_{min}/2 &= \frac{\sqrt{PF_{M,QAM} P_{ave}}}{\sqrt{M} - 1} \\ PF_{M,QAM} &= 3 \frac{\sqrt{M} - 1}{\sqrt{M} + 1} \\ P_{ave} &= (m_{QAM} \mathcal{R}P_o)^2 / 2 \end{aligned} \quad (3.49)$$

where  $PF_{M,QAM}$  is the power factor for M-ary QAM,  $P_{ave}$  is the transmitted QAM power, and  $m_{QAM}$  is the effective QAM modulation index.

Because a symbol represents  $\log_2 M$  bits, the probability of a bit error for a Gray-encoded system will be

$$P_e \approx \frac{4}{\log_2 M} \left(1 - \frac{1}{\sqrt{M}}\right) \int_{d_{min}/2}^{\infty} p(n) dn = BER \quad (3.50)$$

### 3.3.4.7 The Case of Rectangular Pulses

Some mathematical simplifications for  $M_I(j\nu)$  can be made if it is assumed that the symbol pulse shape is rectangular. For this case, the impulse response of the baseband filter is also rectangular and can be written as

$$h(t) = \begin{cases} 1 & , -T_u < t < T_u \\ 0 & , \text{otherwise} \end{cases} \quad (3.51)$$

Substituting (3.51) into (3.41), the expression for  $M_I(j\nu)$  can be simplified to

$$M_I(j\nu) = (1 - \gamma) + \gamma \left[ \int_0^{\infty} J_0(\nu A) p(A) dA \right] \quad (3.52)$$

When the distribution for  $p(A)$  given in equation (3.17) is substituted into (3.52), it was found that a closed-form solution for  $M_I(j\nu)$  can be obtained. This closed-form solution was obtained using the symbolic integration feature of the Mathematica software package and is given by

$$M_I(j\nu) = (1 - \gamma) + \gamma \left[ \frac{2}{9} \sqrt{\frac{3}{\pi}} \frac{c^{3/2}}{\nu} K_{1/6} \left( \frac{2c^3}{27\nu^2} \right) \exp \left( \frac{2c^3}{27\nu^2} \right) \right] \quad (3.53)$$

where  $K_{1/6}(\bullet)$  is the 1/6th order modified Bessel function of the second kind and  $c$  is given by equation (3.18).

#### 4. Implementation of a Fiber-Optic AM-VSB System

This chapter describes the experimental AM-VSB optical transmission system which was implemented for the purpose of conducting experiments on clipping-induced impulsive noise. A block diagram of the system is shown in Figure 4.1.

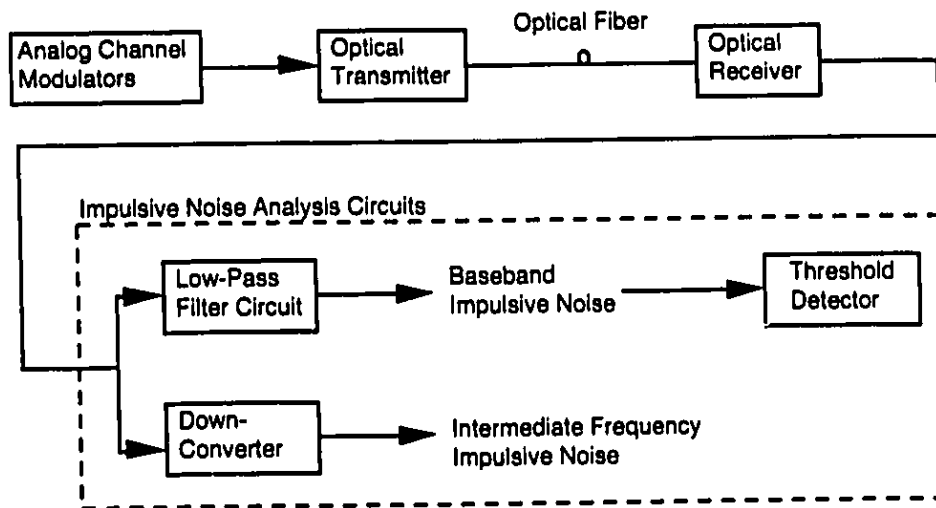


**Figure 4.1: Block Diagram of Experimental AM-VSB Optical Transmission and Analysis System**

It should be noted that in a practical system, the optical receiver is normally followed by channel selection and demodulation circuits. However, because the intent of this thesis is to investigate the fundamental characteristics of clipping-induced impulsive noise, the optical receiver is followed by either of two impulsive noise analysis circuits: a low-pass filter circuit or a down-converter circuit. The low-pass filter circuit was designed to generate baseband impulsive noise by filtering out the channel frequencies and allowing the low-frequency intermodulation products contained in a clipped SCM signal to pass through. The down-converter, which is normally used to shift a selected channel down to

an intermediate frequency, is used to investigate the nature of down-converted impulsive noise.

The main components in the experimental transmission system include the following:

- i) Analog Channel Modulators
- ii) Analog Optical Transmitter
- iii) Analog Optical Receiver
- iv) Low-Pass Filter Circuit
- v) Threshold Detector
- vi) Down-Converter

A description of the electrical and optical properties of these components is given in the following sections.

#### **4.1 Analog Channel Modulators**

The AM-VSB channels were simulated using a Matrix multiple frequency signal generator (Model ASX-16) [57]. The Model ASX-16 contains a bank of crystal-controlled and amplitude-variable oscillators which are tuned to the carrier frequencies of channels 2 through 43 (55.25 MHz to 337.25 MHz) of the NTSC channel frequency plan. The output of the oscillators are combined to simulate up to 42 unmodulated video carriers. The operation of the Model ASX-16 is controlled remotely using IEEE 488 (HP-IB) which facilitates the automation of experiments.

#### **4.2 Analog Optical Transmitter**

The purpose of the optical transmitter in an analog, fiber-based CATV transmission system is to provide a linear transfer function between the input electrical signal and the output optical signal. Because of the stringent requirements on linearity and noise, some lasers are specifically manufactured for application in CATV lightwave transmission. The



optical transmitter used in the experiments contains a distributed feedback (DFB) CATV laser purchased from Fujitsu.

The optical transmitter was designed and built by Kinh Pham and David Clegg of TR Labs for use in analog optical transmission experiments. The transmitter contains a  $75\ \Omega$  input for RF modulation of the laser. The laser bias current is adjusted with a dial on the front panel and can be set from 0 to 60 mA. The DFB laser developed by Fujitsu (model FLD150F3ACH-AL) has a peak wavelength of 1543 nm [58]. The relative intensity noise of the laser module is specified to be -160 dB/Hz and -165.3 dB/Hz at 50 and 550 MHz, respectively.

In Figure 4.2, the output optical power of the transmitter is plotted as a function of bias current. The values for output power were measured with a Hewlett Packard 8153A Lightwave Multimeter as the bias current was slowly increased. The L-I curve shows that the output power of the laser is negligible when the bias current is below threshold. The curve appears to be highly linear in the region above threshold up to 55 mA.

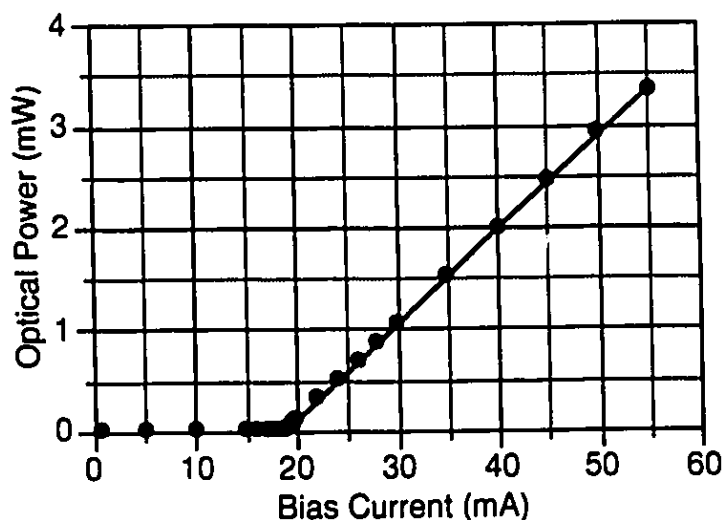


**Figure 4.2: Optical Power vs. Bias Current for Fujitsu CATV Laser**

To get a good estimate of the laser threshold current, an expanded view of the threshold region is shown in Figure 4.3. A nonideal property of the laser can be seen in the curved region between the low power LED and high power lasing regions indicating the gradual onset of stimulated emission in the laser cavity. This characteristic shows a slight deviation from an abrupt turn-on which was assumed in developing the theoretical model in Chapter 3 and demonstrates a possible limitation of the model when it is applied to an actual CATV laser. The threshold current of the laser can be determined by extrapolating the linear lasing portion of the curve back to intersect the forward extrapolated LED portion of the curve [34]. Using this technique, the threshold current is determined to be 18.7 mA.

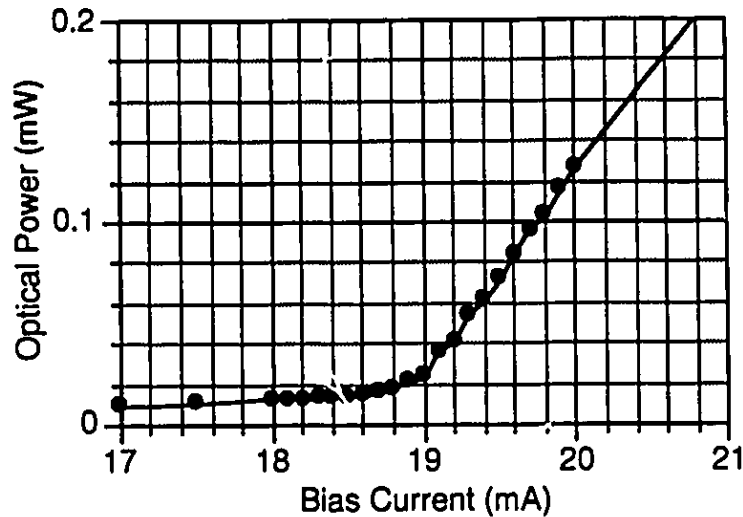


**Figure 4.3: Threshold Region of Optical Power vs. Bias Current Curve**

### 4.3 Analog Optical Receiver

A commercial analog optical receiver manufactured by Ipitek was used in the experiments in this thesis. The Ipitek FiberHub 600 Receiver Module contains an AT&T (model 131D) PIN photodetector which is specifically designed for use in AM-VSB receivers [59]. The AT&T photodetector has a responsivity of 1.05 A/W for an input light wavelength of 1543 nm. The Ipitek receiver also contains a Philips transimpedance

amplifier and a  $75\ \Omega$  RF output on the front panel. The specification for the total front-end noise current spectral density due to the photodetector and transimpedance amplifier is  $6\ \text{pA}/\sqrt{\text{Hz}}$ .

The frequency response of the receiver is of particular interest in clipping-induced impulsive noise experiments because it affects spectrum of the intermodulation power seen at the output. The intrinsic frequency responses of the photodetector, transimpedance amplifier, and internal circuitry all have an affect on the clipped signal waveform as it passes through the receiver. Because of the changes that these components induce on the received optical signal, the output electrical signal may not be a faithful reproduction of the clipped SCM signal that was transmitted from the laser. One way of determining the magnitude of the receiver transfer function is by using the Amplified Spontaneous Emission (ASE) from an optical amplifier as a source of white optical noise and observing the spectrum of the receiver electrical output [60]. Because the bandwidth of the noise generated by the interference between electric field components of the amplifier spontaneous emission (spontaneous-spontaneous beat noise) is very large compared to the high-frequency cutoff of the receiver, the optical noise spectrum is relatively flat across the receiver bandwidth. Thus, the receiver acts as a bandlimiting device, and if enough spontaneous-spontaneous beat noise can be generated to overcome the front-end noise, the magnitude of the frequency response can be observed directly with a conventional RF spectrum analyzer. This technique was used in the setup shown in Figure 4.4 to determine the response profile of the Iptek receiver. An Erbium-Doped Fiber Amplifier (EDFA) was used to generate the ASE noise and the receiver output spectrum was observed with a 0-22 GHz Hewlett Packard 70000 Series spectrum analyzer. A variable optical attenuator (VOA) was employed to adjust the amount of received optical power. For a received optical power of -7.52 dBm, the spectrum shown in Figure 4.5 was detected. It can be seen that the receiver profile is relatively flat across the passband and has a high-frequency cutoff at about 650 MHz. The receiver profile at the low frequencies is shown in Figure

4.6. The bottom trace of Figure 4.6 was captured when the receiver was disconnected from the spectrum analyzer and represents the spectrum analyzer noise floor. The top trace represents the receiver profile which appears to have a low-frequency 3 dB cutoff at about 4 MHz.

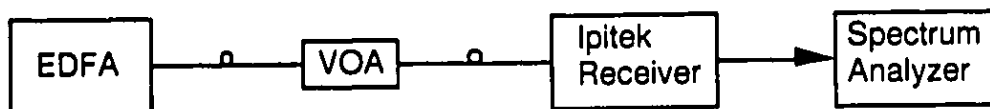


**Figure 4.4: Setup for Determining Receiver Frequency Response**

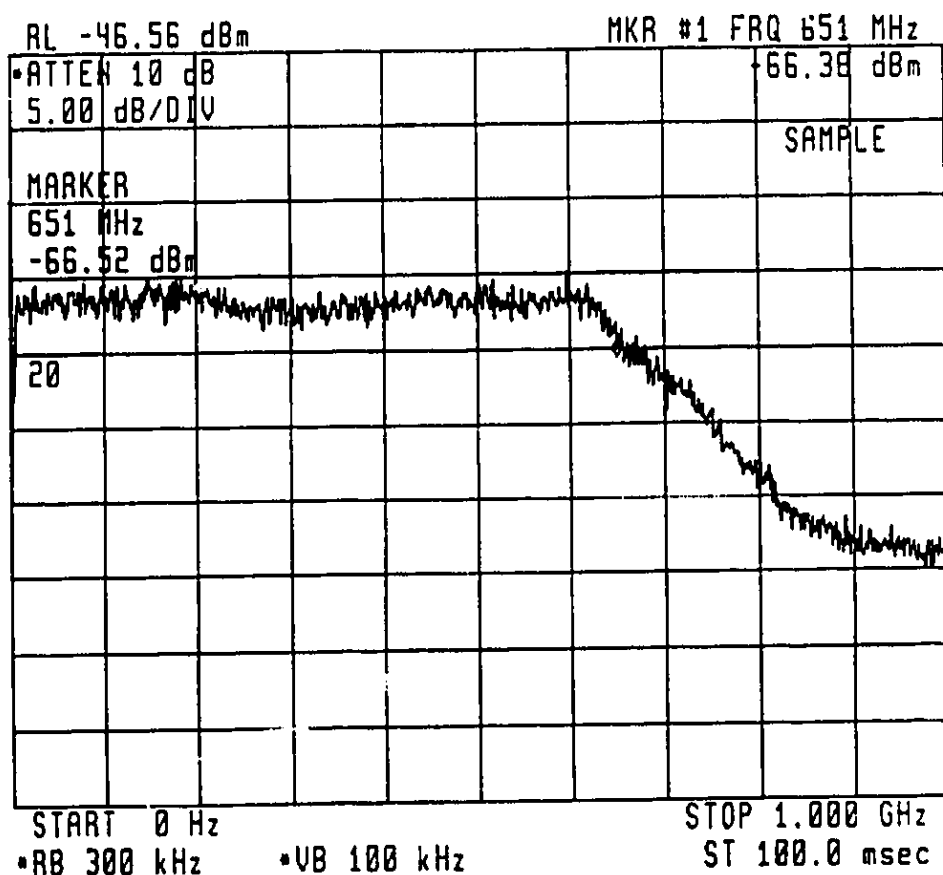


**Figure 4.5: Frequency Response of the Ipitek Receiver**

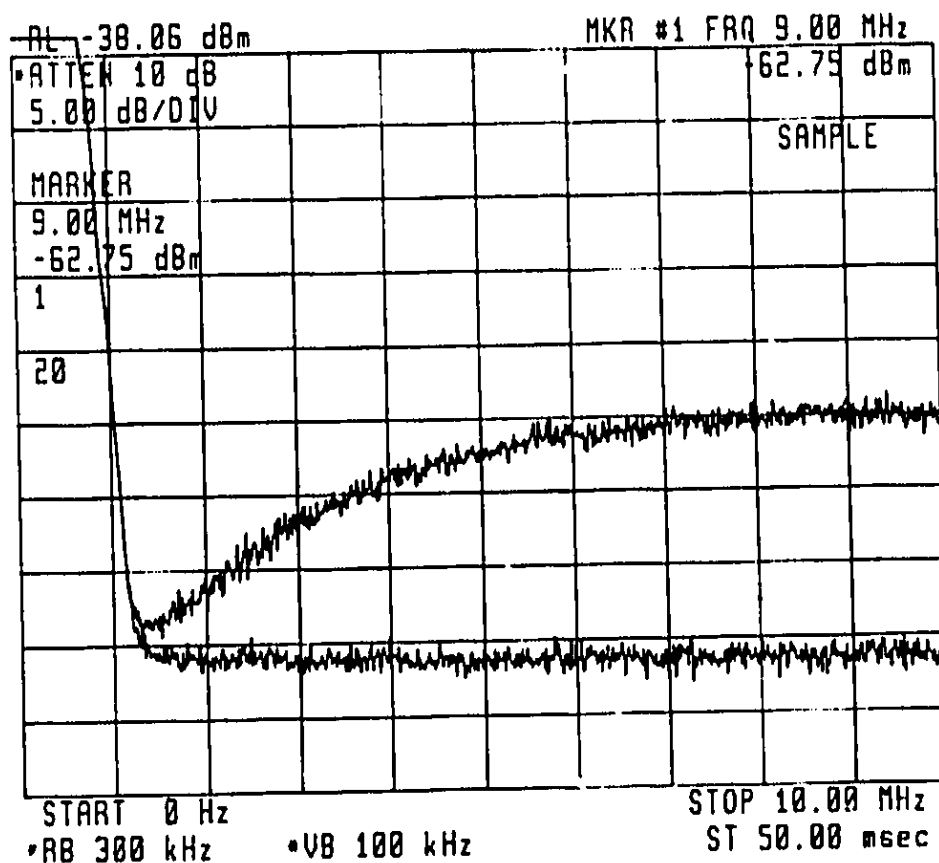


**Figure 4.6: Low Frequency Response of the Ipitex Receiver**

#### 4.4 Low-Pass Filter Circuit

The low-pass filter circuit was designed to pass the low-frequency content of the clipped SCM signal through while suppressing the carrier frequencies. The clipped SCM signal contains many intermodulation products, some of which land in the region between 0 Hz and the lowest carrier frequency. In the NTSC frequency plan, Channel 2 has the lowest carrier frequency at 55.25 MHz. To adequately characterize the impulsive noise induced by clipping, it is desirable to send as much impulsive noise power through as possible such that the impulsive noise can be distinguished from the additive Gaussian noise in the system. However, the low-pass filter must also adequately suppress the frequency components of the carriers so that they are not present in the output noise signal.

The low-pass filter circuit is shown in Figure 4.7. The Mini-Circuits SLP-21.4 low-pass filter has a 3 dB cutoff at 24 MHz and has an insertion loss of 65 dB at 55.25 MHz as shown in Figure 4.8. The frequency response of Figure 4.8 was measured with a Hewlett Packard 8753A network analyzer which also has the ability to determine the impulse response by performing a Fast Inverse Fourier Transform. The rectified version of the impulse response is shown in Figure 4.9. Because of the low cutoff frequency of the SLP-21.4, most of the carrier power is reflected back towards the output of the optical receiver. A 10 dB attenuator is placed in front of the filter to dampen the reflected carrier power so that it does not distort the clipped SCM signal at the receiver output. The SLP-21.4 is followed by two RF amplifiers which are needed to increase the amplitude of the impulse noise for amplitude distribution and time distribution measurements. The SHF90P is a 10 kHz-15 GHz broadband amplifier which has a gain of 25 dB and a noise figure of 7 dB. The 3 kHz-10 GHz Veritech (model VMA3K10C-323) broadband amplifier has a gain of 32 dB, a noise figure of 7 dB, and a 1 dB gain compression point at 17 dBm output power.

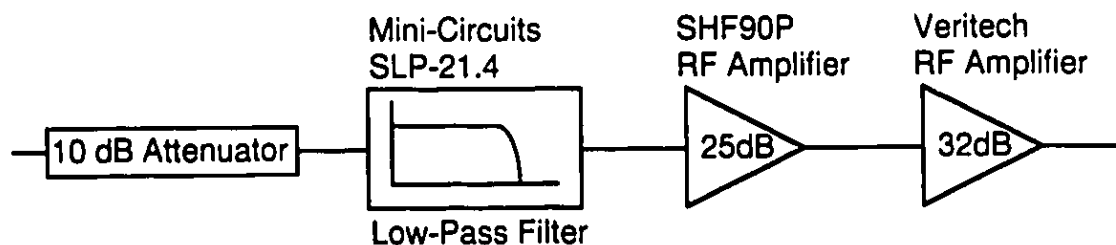


**Figure 4.7: Low-Pass Filter Circuit**

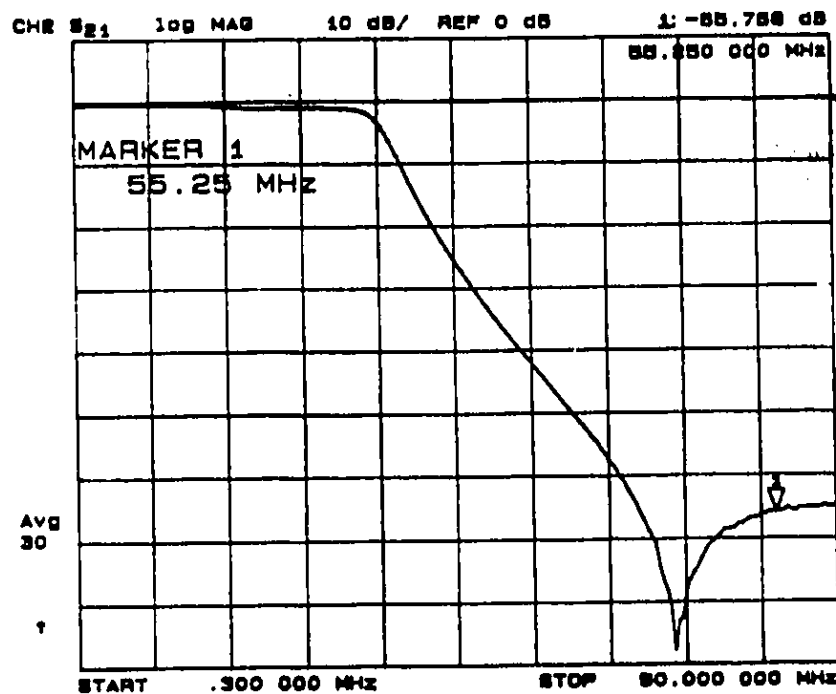


Figure 4.8: Magnitude of Low-Pass Filter Frequency Response

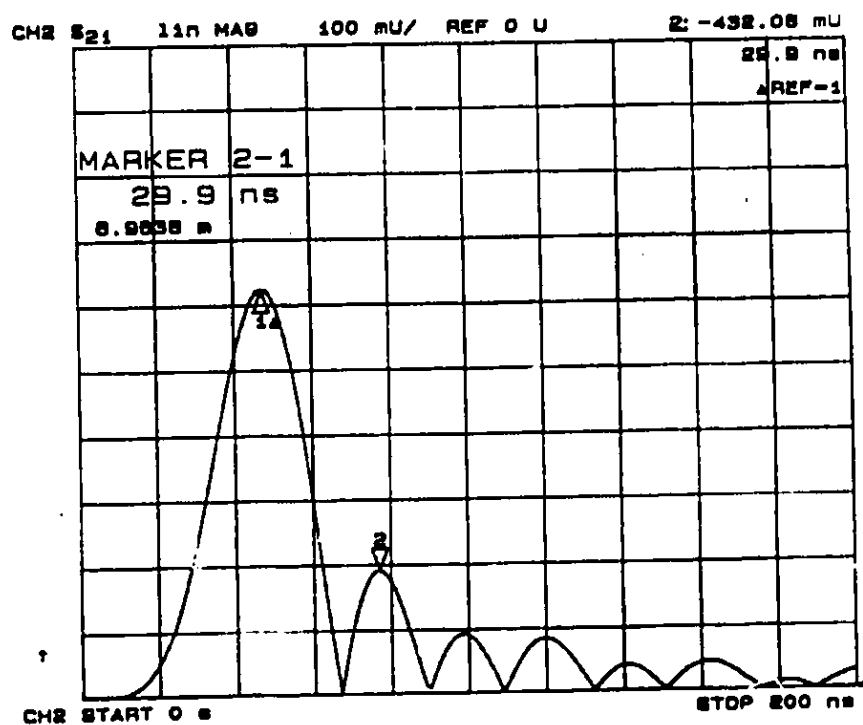
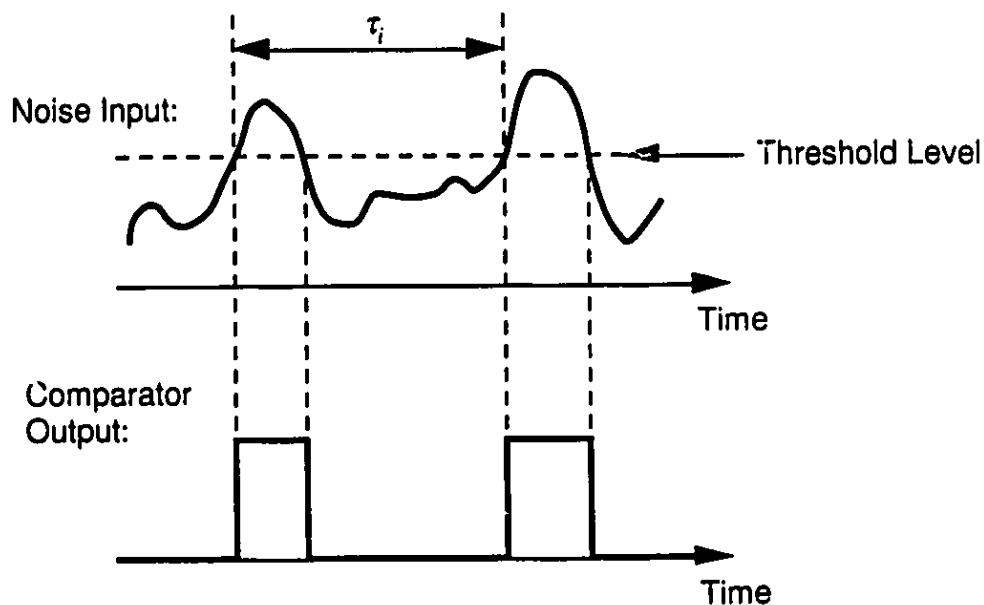


Figure 4.9: Low-Pass Filter Impulse Response

#### 4.5 Threshold Detector

The threshold detector was designed and built at TRLabs specifically to measure the statistics of low-frequency impulsive noise. Its operation is based on comparing the input signal level to a fixed and stable threshold voltage. A fast Integrated Circuit (IC) comparator is used to provide a TTL output that indicates whether the input signal is above or below the threshold. The threshold detector also contains a Time Interval Sampler circuit that measures the time between consecutive upcrossings of the input noise signal. Figure 4.10 shows examples of the noise input and comparator output waveforms and indicates the time interval  $\tau_i$  between upcrossings.



**Figure 4.10: Sample Waveforms of Comparator Input and Output**

The block diagram of the threshold detector is shown in Figure 4.11. The threshold level is set by a potentiometer dial on the front panel and has a range of -5 volts to +5 volts. Stability of the +5 volt and -5 volt references is important for accurate threshold



crossing measurements, therefore an Analog Devices AD588 High Precision Voltage Reference IC is employed. The comparator used in the threshold detector is an Analog Devices AD9696 Ultrafast Comparator which provides a TTL compatible output. The AD9696 has a 4.5 ns propagation delay and 200 ps maximum propagation delay dispersion. The threshold detector also contains a Time Interval Sampler which measures the time between two consecutive threshold upcrossings. The Time Interval Sampler circuit is implemented with FAST TTL logic and utilizes a 50 MHz 32-bit counter to measure the time interval. A finite state machine is used to start and stop the counter and to provide the appropriate control and data signals. The control and data signals are accessed via a 50-pin connector on the front panel.

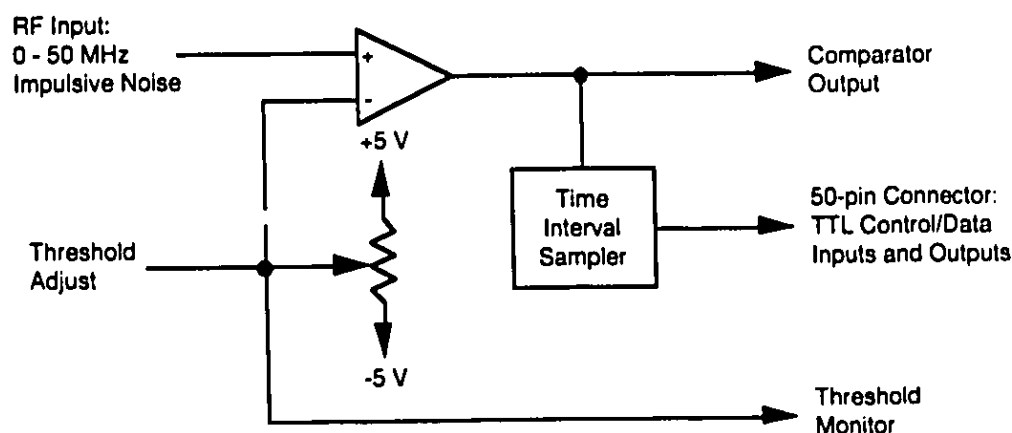


**Figure 4.11: Block Diagram of the Threshold Detector**

A more detailed description of the design of the Threshold Detector along with circuit schematics is included in the Appendix.

## 4.6 Down-Converter

The down-converter used in the experiments was designed and built by David Moore and is shown in the block diagram in Figure 4.12. A two-stage design was chosen

to allow any 15 MHz wide channel under 600 MHz to be shifted down to an arbitrary Intermediate Frequency (IF) below 300 MHz. The particular channel to be down-converted is selected by using an appropriate frequency for the first oscillator while the frequency of the second oscillator is used to select the desired output IF frequency.

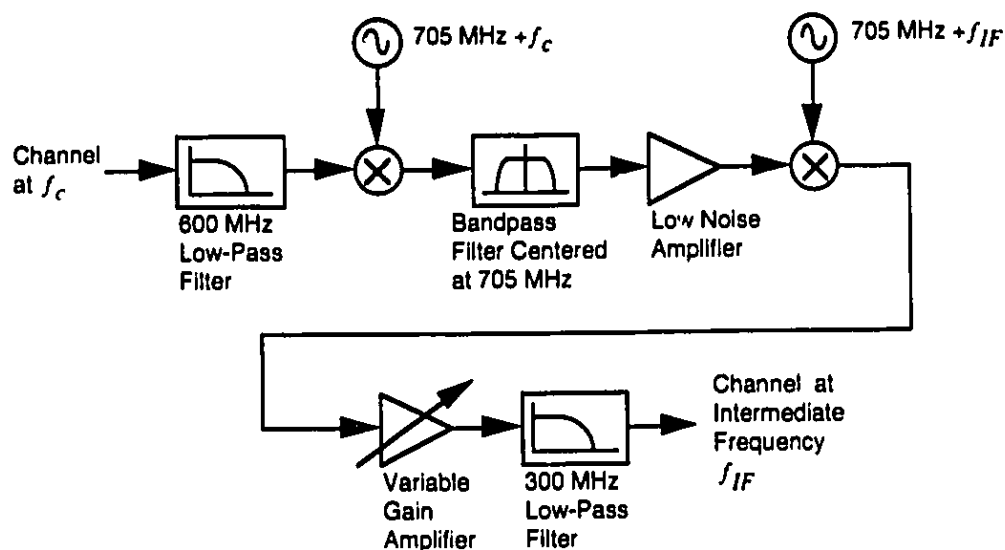


**Figure 4.12: Block Diagram of Down-Converter**

The input of the down-converter contains a 600 MHz low-pass filter which attenuates the noise at images frequencies which would degrade the channel during the mixing stages. The received signal is then mixed with a local oscillator at a frequency of  $705 \text{ MHz} + f_c$  resulting in a signal at 705 MHz. This signal is filtered by a 15 MHz wide bandpass filter centered at 705 MHz. The power level of the signal is then boosted by a Low Noise Amplifier (LNA) which provides 20 dB of gain. The 705 MHz signal is mixed with a local oscillator at  $705 \text{ MHz} + f_{IF}$  resulting in a down-converted signal at  $f_{IF}$  and an up-converted signal at  $1410 \text{ MHz} + f_{IF}$ . The up-converted signal is removed with a 300 MHz low-pass filter at the output of the down-converter, and the output power is adjusted using a variable gain amplifier. The local oscillator carriers were generated with a Hewlett Packard 8642A signal generator and the continuous-wave output of a Hewlett Packard

8753A network analyzer. The rest of the components in the down-converter are specified in the following table:

Component	Model Number
600 MHz low-pass filter	Mini-Circuits SLP-600
First and second mixers	Mini-Circuits ZFM-150
Bandpass filter centered at 705 MHz	Trak ACF 705-X12-3SS
Low noise amplifier	Mini-Circuits ZFL-1000LN
Variable gain amplifier	Mini-Circuits ZFL-1000GH
300 MHz low-pass filter	Mini-Circuits SLP-300

**Table 4.1: Down-Converter Component Model Numbers**

#### 4.7 System Characterization

This section contains two parts: modulation index calibration and CNR. First, a method for determining the peak modulation index per channel in the system is explained. To verify the accuracy of the modulation index calibration as well as other system parameters, the CNR of the system is determined and compared with the theoretical CNR which was developed in Chapter 2.

##### 4.7.1 Modulation Index Calibration

Obtaining an accurate value for the experimental modulation index is critical in the analysis of clipping-induced impulsive noise because small deviations in the modulation index cause large changes in the results of the theoretical model. The modulation index is defined by

$$m = \frac{I_{peak}}{I_{bias} - I_{th}} \quad (4.1)$$

The parameters  $I_{bias}$  and  $I_{th}$  are the laser bias and threshold currents and can be accurately measured in an experiment. However, a precise value for peak amplitude of the modulation current  $I_{peak}$  is more difficult to determine. It might be suggested that  $I_{peak}$  could be determined by simply measuring the amplitude at the modulation input of the optical transmitter. However, electronic circuits and connections inside the transmitter affect the amplitude of the modulating signal as it travels from the input to the laser diode. To obtain accurate values for modulation index in the experiments in this thesis, an alternate technique is used.

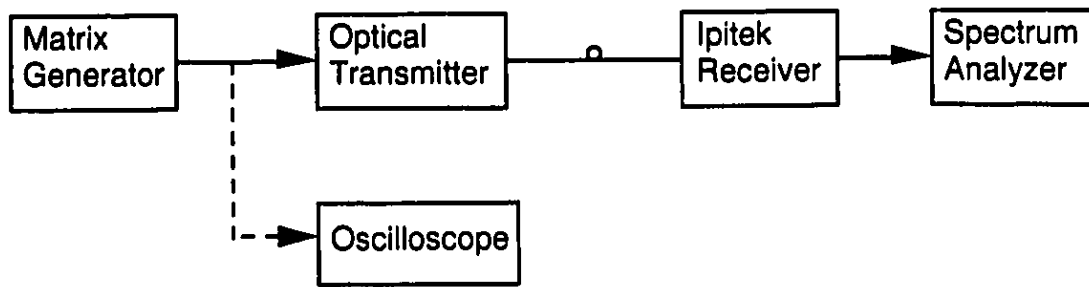


**Figure 4.13: Modulation Index Calibration Setup**

The technique involves determining the bias current value that gives 100% modulation for a known input sinusoidal amplitude. The setup for performing the calibration is shown in Figure 4.13. Only the 163.25 MHz carrier (NTSC Channel 21) is used from the Matrix Generator. The peak-to-peak voltage of this carrier  $V_{c,p-p}$  is measured on a Tektronics 2465A analog oscilloscope. The laser bias current is initially set to a high value such that no clipping occurs when the Matrix Generator is connected to the transmitter. The bias current is then slowly decreased until 100% modulation is attained. This point is determined by observing the power of the carrier with a spectrum analyzer at the receiver. As the bias current is decreased below the 100% modulation point, the bottom portion of the modulating sinusoid becomes clipped, and the power in the fundamental frequency shifts to higher harmonics. When the carrier power is plotted as a function of

bias current, the 100% modulation bias current  $I_c$  is indicated by a rapid drop in carrier power caused by the onset of clipping. Once  $I_c$  is determined for the input voltage amplitude of  $V_{c,p-p}$ , a simple transformation can be used to calculate the modulation index for the general case of an arbitrary bias current  $I_{bias}$  and an arbitrary input voltage (peak-to-peak) amplitude of  $V_{in,p-p}$ :

$$m = \frac{V_{in,p-p}}{V_{c,p-p}} \frac{I_c - I_{th}}{I_{bias} - I_{th}} \quad (4.2)$$

Figure 4.14 shows the carrier power versus bias current for  $V_{c,p-p} = 620 \text{ mV}$ . It can be seen that the carrier power drops dramatically at a bias current of  $I_c = 24 \text{ mA}$ . Using the value for the threshold current which was obtained in Section 4.2, the following expression can be used to calculate the modulation index in the system:

$$m = \frac{V_{in,p-p}}{620 \text{ mV}} \frac{24 \text{ mA} - 18.7 \text{ mA}}{I_{bias} - 18.7 \text{ mA}} = \frac{V_{in,p-p}}{620 \text{ mV}} \frac{5.3 \text{ mA}}{I_{bias} - 18.7 \text{ mA}} \quad (4.3)$$

To ensure that the modulation index value is valid for all the other carriers in the 42 channel system, the power of the carriers are individually adjusted to be equivalent to the Channel 21 carrier power in the fiber. In an experiment, the peak modulation index per channel for a specific SCM input is simply determined by shutting off all the channels except for Channel 21, recording the peak-to-peak voltage  $V_{in,p-p}$  on the oscilloscope, and calculating the value of equation (4.3).

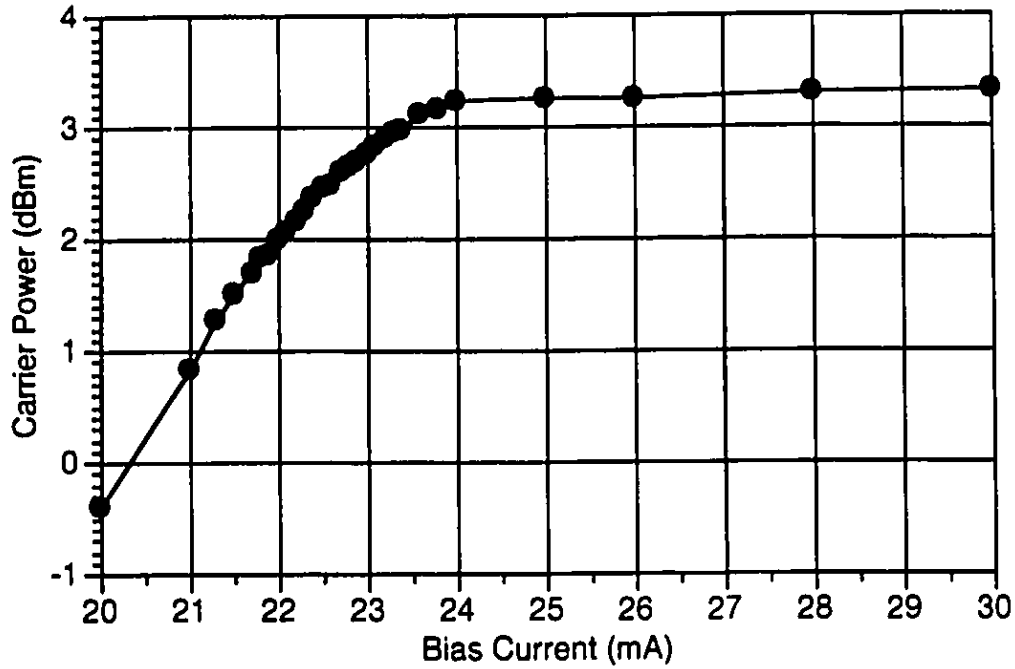


**Figure 4.14: Carrier Power vs. Bias Current for Channel 21 (163.25 MHz)**

#### 4.7.2 System CNR

The Carrier-to-Noise Ratio is often used to characterize the performance of an analog system and can be expressed as

$$CNR = \frac{\frac{1}{2}(m\mathcal{R}P_o)^2}{(i_{th}^2)B + 2q\mathcal{R}P_oB + RIN(\mathcal{R}P_o)^2B} \quad (4.4)$$

where  $i_{th}$  is the front-end noise current spectral density and the other parameters are defined in Section 2.2.2. The first, second, and third terms in the denominator of equation (4.4) account for the CNR limitations caused by receiver thermal noise, shot noise, and laser RIN noise, respectively.

To compare the CNR performance of the experimental system with the CNR predicted by equation (4.4), the setup shown in Figure 4.15 is used. The 163.25 MHz carrier of Channel 21 (163.25 MHz) from the Matrix Generator is used to modulate the

Fujitsu laser diode which is biased at 50 mA. A variable optical attenuator controls the optical power received by the photodetector. The peak modulation index is set to 0.0288. The responsivity of the AT&T photodiode is 1.05 A/W, and the laser RIN has a -160 dB/Hz specification at a bias current of 50 mA. The thermal noise current density referred to the output of the photodiode is  $6 \text{ pA} / \sqrt{\text{Hz}}$ . In calculating equation (4.4), it is standard practice [31] to use a value of  $B = 4 \text{ MHz}$  which is the baseband bandwidth of the video portion of the signal.

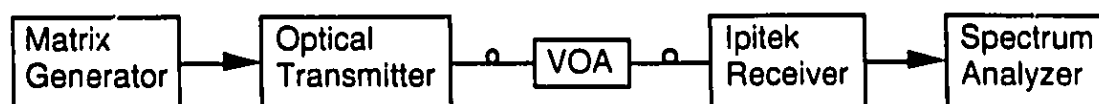


**Figure 4.15: Experimental Setup for Measuring CNR**

The carrier power is measured in units of dBm with the spectrum analyzer adjusted to the following setting as specified by the NCTA Recommended Practices and Procedures [31]: resolution bandwidth of 300 kHz, video bandwidth of 100 Hz, and frequency span of 10 MHz. The noise power is measured using the noise measurement function of the HP 70000 spectrum analyzer. The function gives the noise spectral density in units of dBm/Hz and takes into account the shape of the resolution bandwidth filter in the spectrum analyzer. The noise in a 4 MHz bandwidth is obtained by multiplying the measured noise spectral density with 4 MHz. To ensure that the measured noise level is due to the noise of the optical system and is not dominated by the intrinsic thermal noise of the spectrum analyzer, a simple test can be performed by disconnecting the system from the spectrum analyzer. If the noise level drops appreciably when the system is disconnected, the system noise is dominant, but if the noise floor remains unchanged, the spectrum analyzer noise is dominant. If the noise level does not drop by more than 10 dB, the spectrum analyzer thermal noise can be accounted for by subtracting the disconnected noise power from the noise power which is measured after the system is re-connected.

The CNR was measured for different received optical powers as shown in Figure 4.16. The plot also contains the values calculated using equation (4.4) and the CNR limit due to the separate sources of noise. It can be seen that there are three distinct noise limited regimes: 1) the RIN noise limited region for high received optical powers, 2) the shot noise limited region for moderate received optical powers, and 3) the thermal noise limited region for low received optical powers. There is good agreement between the calculated and measured CNRs which suggests that the system specifications given in this chapter are accurate and that the modulation index calibration is valid.

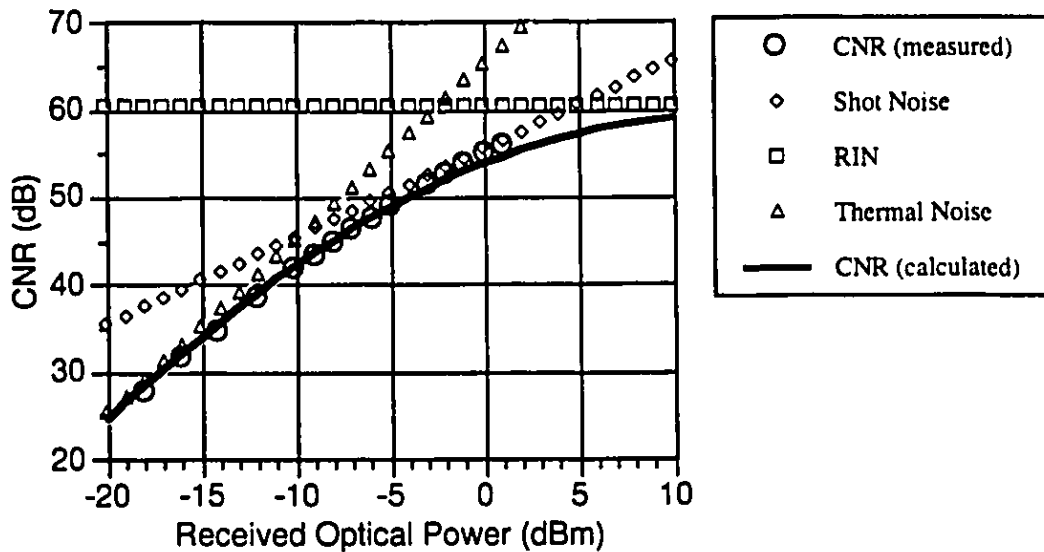


**Figure 4.16: Measured and Calculated System CNR Performance**



## 5. Experiments on Clipping-Induced Impulsive Noise

### 5.1 Low-Pass Filter Experiments

The motivation for the low-pass filter experiments is to characterize the statistics of clipping events in a directly-modulated SCM system. The problem of analyzing the threshold crossings of an SCM signal may seem conceptually quite simple. However the experimental verification of threshold crossing behavior is complicated by the fact that excursions beyond the threshold can have a very short duration and a very small amplitude. Because the average duration of clipping events is very short, as illustrated by Figure 3.7, the complete detection of threshold crossings directly at the transmitter would be very difficult even with the fastest electronics currently available.

An alternate approach to detecting the clipping events utilizes a low-pass filter at the receiver to increase the time duration of each clip as shown in Figure 5.1. At the transmitter output, the clipping events are represented by the error signal which sums with the desired signal to form the clipped signal. The function of the low-pass filter after the receiver is to filter out all frequency components of the desired signal such that the output only contains the low-frequency responses to the clipping events in the error signal. In an NTSC system, the desired SCM signal does not contain any frequency components below the lowest channel carrier of 55.25 MHz (Channel 2) so a low-pass filter with a cutoff below 55.25 MHz is appropriate. As illustrated in the figure, each input clipping event at the filter will stimulate an output transient response having a longer time duration. While the low-pass filter has the effect of elongating the clip pulse, the output response will also have a smaller amplitude due to energy conservation principles. An amplification stage is used after the filter to boost the power of the filtered impulsive noise to within the sensitivity range of the instruments used for measurements.

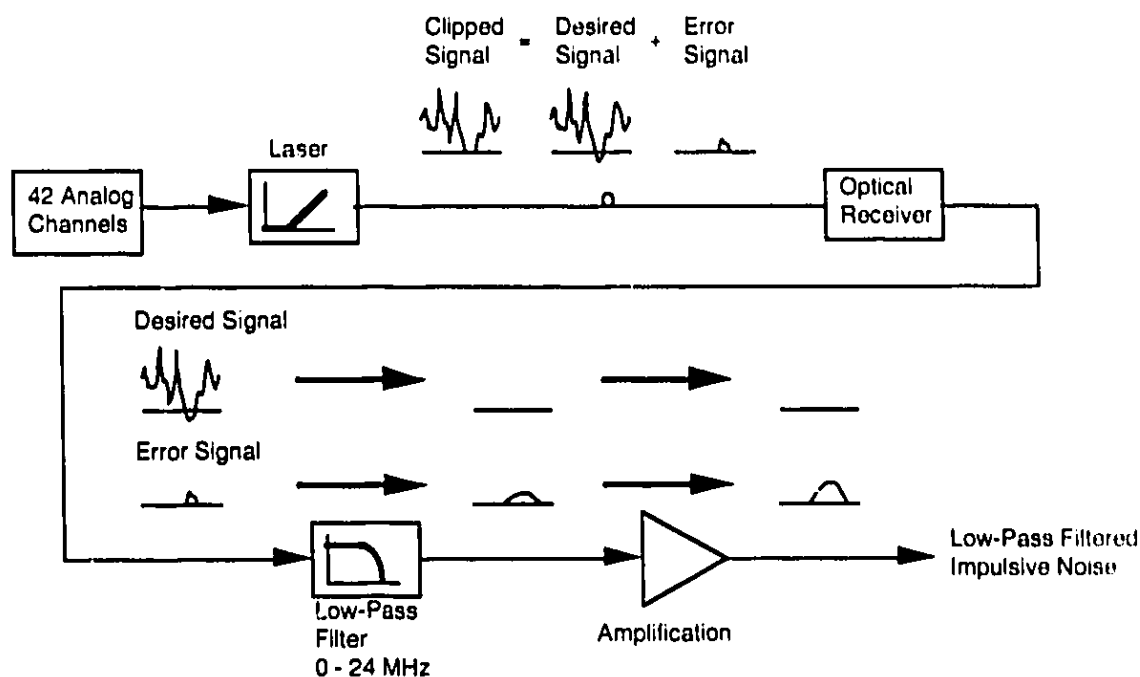


**Figure 5.1: Generating Low-Pass Filtered Impulsive Noise**

It is the intent of the low-pass filter experiments to demonstrate the nature of the clipping process by detecting threshold crossings of the filter impulse responses. A one-to-one correspondence between a clipping event at the transmitter and a threshold crossing at the receiver would require the filter to have a non-oscillatory transient response. However, because of the sharp frequency response rolloff required to attenuate the SCM signal spectrum, the impulse response of the SLP-21.4 low-pass filter (Figure 4.9) does have decaying oscillations which may cause multiple threshold crossing events to be detected. The possibility of multiple threshold crossings caused by a single clip is a source of error in the results for the low-pass filter experiments. The effect of additive Gaussian noise in the system will also cause the statistics of the detected threshold crossings to deviate from the statistics of the clipping events at the transmitter. One final source of error to consider is the low-frequency cutoff of the Iptek optical receiver which, when cascaded with the frequency response of the low-pass filter, will cause the impulsive noise to be bandpass

filtered as opposed to low-pass filtered. This effect can be seen in the spectrum analyzer plot of Figure 5.2 which was measured at the output of the amplification stage. The noise plateau between 6 MHz and 24 MHz is due to the combined effect of the low-frequency cutoff of the Ipittek receiver, the high-frequency cutoff of the SLP 21.4 low-pass filter, and the amplification of the noise at the filter output. The drop in the noise floor at 24 MHz suggests that the thermal noise contribution of the wideband amplifiers is small and that the shot and thermal noise generated before the filter are the dominant sources of Gaussian noise. A sample of the low-pass filtered impulsive noise waveform was captured using a Hewlett Packard 16531A Digitizing Oscilloscope and is shown in Figure 5.3.

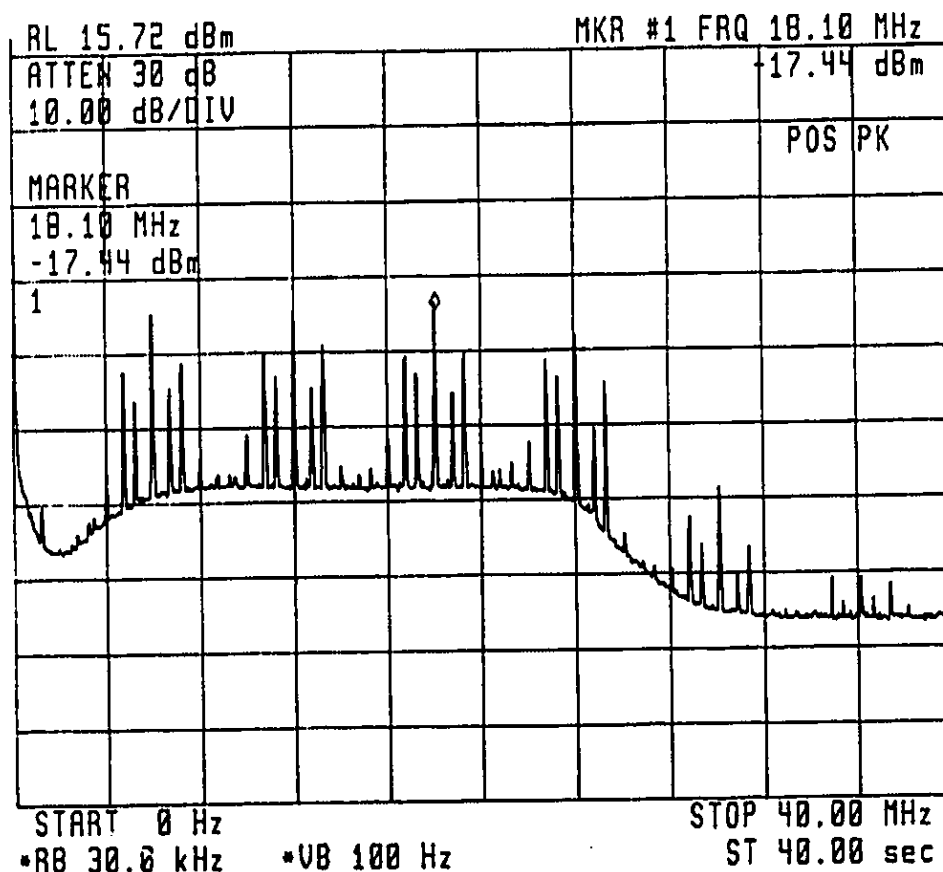


**Figure 5.2: Spectrum of Low-Pass Filtered and Amplified Impulsive Noise**

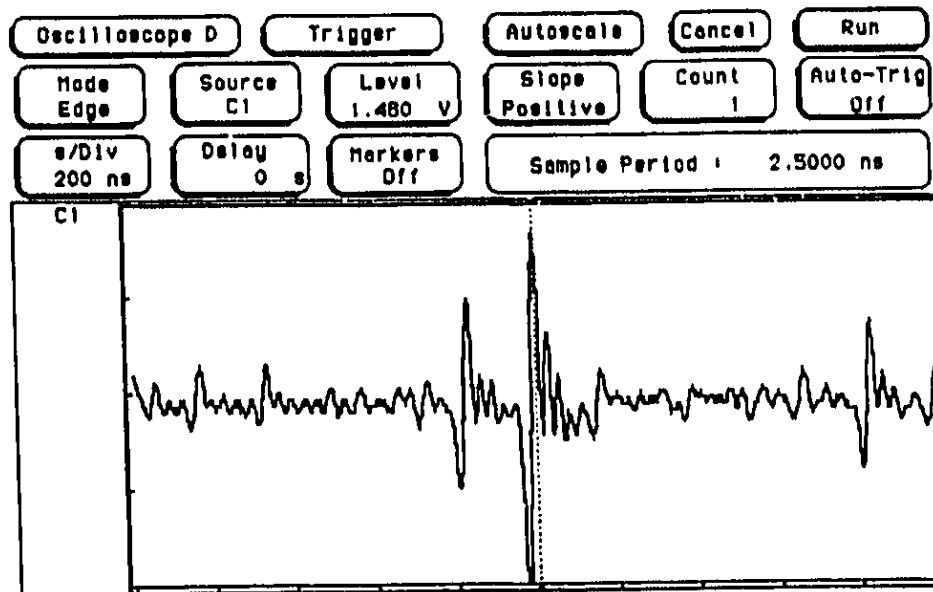


**Figure 5.3: Low-Pass Filtered Impulsive Noise Sample Waveform**

For the experimental work in this thesis, there are three types of measurements performed on the low-pass filtered and amplified impulsive noise:

- 1) Probability density of the noise amplitude
- 2) Threshold crossing rate as a function of threshold value
- 3) Probability density of the time interval between consecutive threshold crossings

A detailed description of the experimental setups as well as the measurement results are given in the following sections.

### **5.1.1 Amplitude Distribution**

The experimental setup shown in Figure 5.4 was used to obtain the amplitude probability density of impulsive noise. A very short length of optical fiber (approximately 4 meters) was used so that the deleterious effects of fiber dispersion and attenuation would

not have a significant effect on the statistics of the impulsive noise generated at the receiver. At the output of the low-pass filter circuit, a Hewlett Packard 54120B Digitizing Oscilloscope was used to sample the amplitude of the noise signal. The histogram function on the HP 54120B samples the input and categorizes each sample into one of 256 voltage ranges. To determine the experimental amplitude probability densities in this thesis, representative histograms with a sample size of 100200 were acquired with the HP 54120B. The operation of the HP 54120B was remotely controlled by a computer using the HP-IB interfacing bus and the Labview software program. The use of Labview facilitated the capture of histogram data into raw data files that were later uploaded to a Unix workstation. The experimental probability densities were derived from the histogram data by a simple normalization process. In this process, the histogram area was calculated using the trapezoidal rule where the sampled values of the histogram function corresponded to the sample counts for each of the 256 voltage ranges. Each sample count was then divided by the histogram area to obtain the normalized probability density. The C program used to implement the normalization process is given in the Appendix.

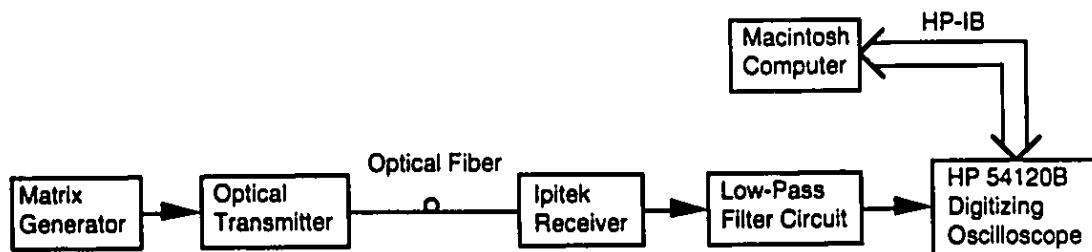


**Figure 5.4: Setup for Amplitude Distribution Experiment**

In the experiment, several probability densities were obtained for modulation indices ranging from  $m = 0$  to  $m = 0.062$ . The experimental probability densities obtained for the cases of  $m = 0$ ,  $m = 0.04$ ,  $m = 0.05$ , and  $m = 0.062$  are shown in Figure 5.5. The laser bias current was set to 50 mA which resulted in a received optical power of 3.3

dBm at the photodetector. A high received optical power was desired to maximize the signal-to-noise power ratio at the input to the oscilloscope. In this experiment, the signal is considered to be the clipped SCM waveform, and the noise includes the Gaussian front-end, RIN, and shot noises. Referring to the plot of the system CNR performance in Figure 4.6, it can be seen that a received optical power of 3.3 dBm corresponds to a shot noise limited regime where the dominant source of Gaussian noise is due to the random arrival of photons at the photodetector.

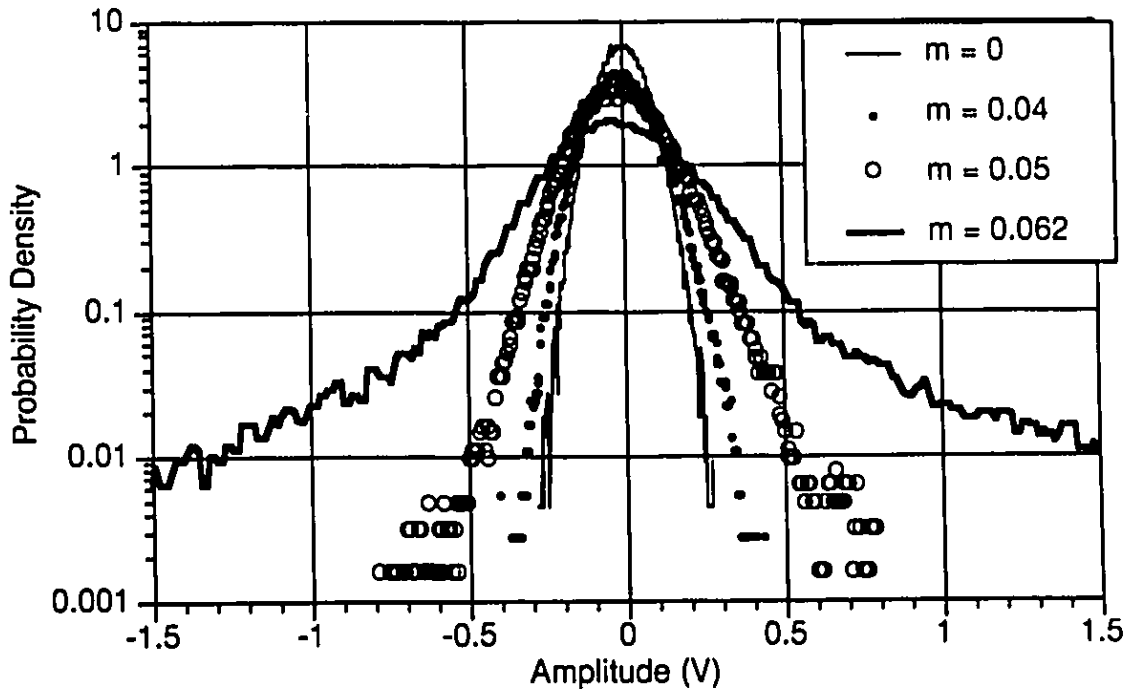


**Figure 5.5: Probability Density of Low-Pass Filtered Impulsive Noise**

In Figure 5.5, it can be seen that increasing the modulation index at the transmitter has the effect of spreading out the probability density of the noise amplitude at the receiver. The spreading of the probability density curve is expected because of the increased amplitude and frequency of clipping events (and impulse responses) for higher modulation indices. For the case of  $m = 0$ , there is no modulation on the optical carrier and the

received optical power is constant at the photodetector. The probability density for this case represents the Gaussian noise in the system and contributes to the shape of the probability densities for the other cases. In addition to spreading out the curve, it is observed that higher modulation indices cause the tails of the probability density to be pronounced. This effect is visible in the curve for  $m = 0.062$  where the shape of the probability density is significantly different from the Gaussian shape of  $m = 0$ .

To demonstrate how the probability density deviates from a Gaussian distribution as the modulation index is increased, Figures 5.6 to 5.9 show the experimental probability densities compared with the equivalent Gaussian distribution for modulation indices of 0.02, 0.05, 0.055, and 0.062. The equivalent Gaussian distributions are generated by using the equation

$$p_x(x) = \frac{1}{\sqrt{2\pi}\sigma_x} \exp\left(-\frac{x^2}{2\sigma_x^2}\right) \quad (5.1)$$

where  $x$  is the amplitude and  $\sigma_x^2$  is the variance of the Gaussian distribution. The HP 54120B Digitizing Oscilloscope has the capability of calculating the standard deviation of the histogram data. The variance of the input signal can thus be calculated by squaring the standard deviation value. In Figures 5.4 to 5.7, the variance  $\sigma_x^2$  in equation (5.1) is equated to the measured variance of the input signal so that a comparison can be made between the amplitude distributions of the input signal and a Gaussian signal having the equivalent power.

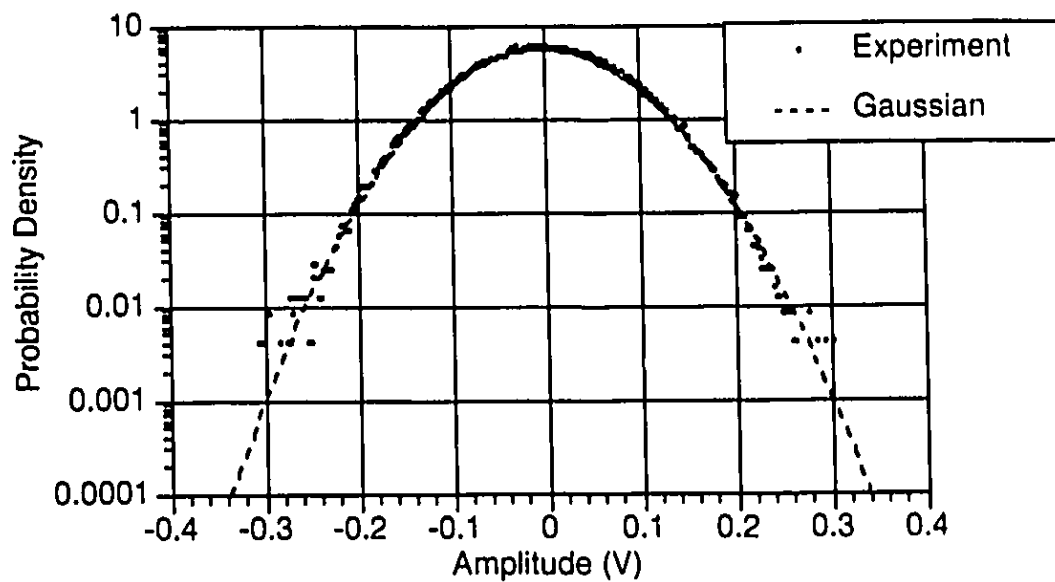


**Figure 5.6: Probability Density of Low-Pass Filtered Impulsive Noise for  $m = 0.02$**

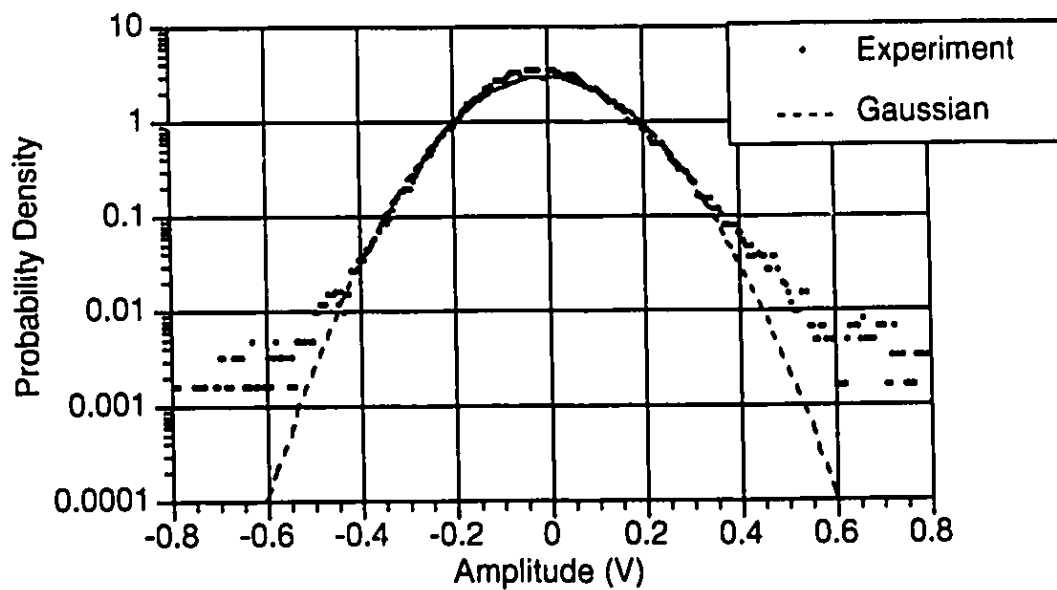


**Figure 5.7: Probability Density of Low-Pass Filtered Impulsive Noise for  $m = 0.05$**



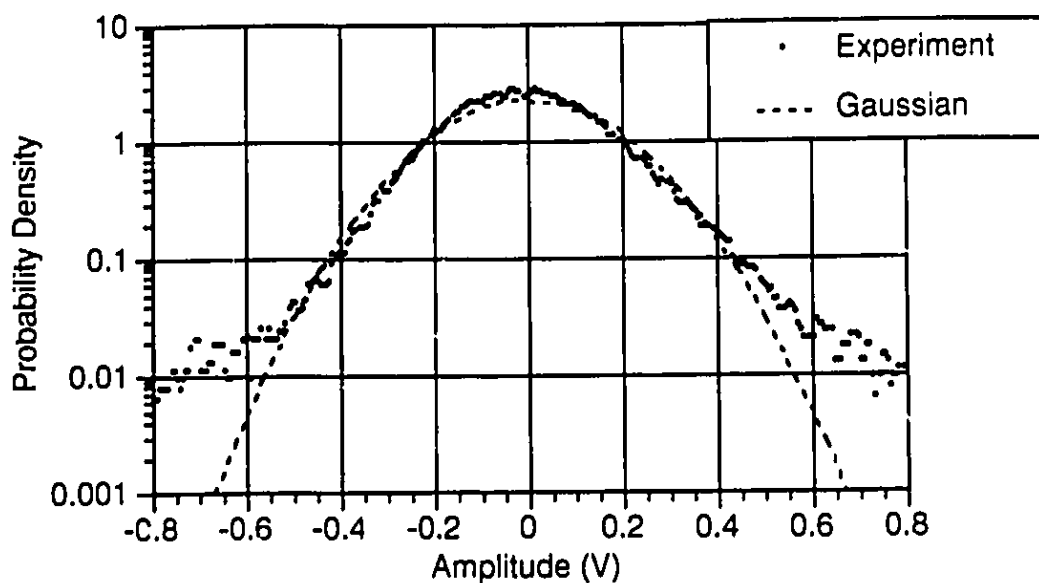


**Figure 5.8: Probability Density of Low-Pass Filtered Impulsive Noise for  $m = 0.055$**

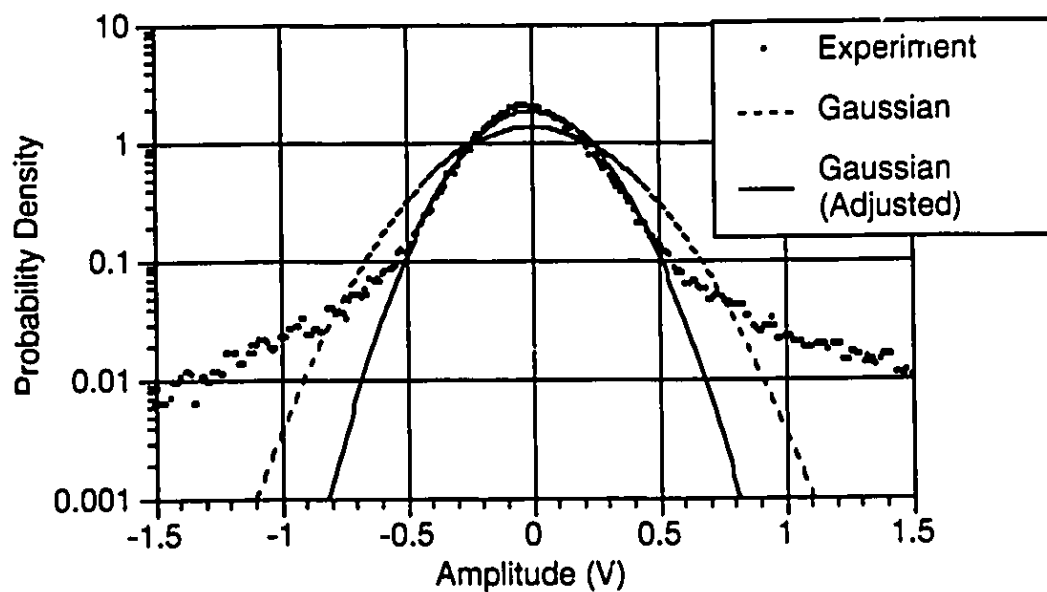


**Figure 5.9: Probability Density of Low-Pass Filtered Impulsive Noise for  $m = 0.062$**

In Figure 5.6, it can be seen that the experimental curve follows the Gaussian curve quite closely. This indicates that at a modulation index of 0.02, the Gaussian noise is still dominant and that the effect of clipping on the probability density is negligible. As the modulation index is increased to 0.05 in Figure 5.7, the experimental density starts to deviate from the Gaussian shape as the tail sections of the curve become raised. This effect is further emphasized in Figures 5.8 and 5.9. In Figure 5.9, the experimental probability density is compared to two different Gaussian distributions. The distribution represented by the dotted line is the theoretical amplitude probability density of a Gaussian noise signal having the same variance (and hence power) as the input noise signal. The second Gaussian distribution has been adjusted to fit the central part of the experimental distribution as close as possible. This was achieved by setting  $\sigma_v = 210\text{mV}$  in equation (5.1). It can be seen from Figure 5.9 that the contribution of clipping-induced impulsive noise for the case of  $m = 0.062$  results in a probability density shape that is significantly different than that of an equivalent-power Gaussian noise signal. However, it appears that an adjusted Gaussian distribution can be used to model the probability density quite accurately in the region close to the mean. In the large amplitude regions, the adjusted Gaussian distribution is not accurate due to the pronounced tails of the experimental distribution. The Gaussian shaped main lobe region is the subject of further discussion in Section 5.3

As mentioned earlier in this section, the HP 54120B has the ability to calculate the standard deviation of an acquired histogram. The power of the input noise signal can be determined by first squaring the standard deviation to obtain the mean square value of the signal amplitude. Because the oscilloscope has a  $50\ \Omega$  input, the noise power  $P_{in}$  can be obtained by dividing the mean square value by  $50\ \Omega$ :

$$P_{in} = \frac{\sigma_{tot}^2}{50\Omega} \quad (5.2)$$

where  $\sigma_{tot}$  is the standard deviation of the input signal noise voltage. Because the  $m = 0$  distribution represents the total Gaussian noise in the system, the Gaussian noise power can be calculated by

$$P_{in} = \frac{\sigma_g^2}{50\Omega} = \frac{(71.08 \text{ mV})^2}{50\Omega} = 0.101 \text{ mW} = -9.95 \text{ dBm} \quad (5.3)$$

where  $\sigma_g = 71.08 \text{ mV}$  is the standard deviation of the  $m = 0$  distribution measured by the oscilloscope. Because the additive noise due to clipping is statistically independent of the Gaussian noise, the standard deviation of the impulsive noise distribution can be calculated by [50]

$$\sigma_i = \sqrt{\sigma_{tot}^2 - \sigma_g^2} \quad (5.4)$$

Table 5.1 lists the standard deviation of the input noise signal for various modulation indices and the values for  $\sigma_i$  calculated using equation (5.4). Comparing  $\sigma_g$  and  $\sigma_i$ , it can be seen that the impulsive noise power is greater than the Gaussian noise power for modulations indices above  $m = 0.043$ .

$m$	$\sigma_{tot} \text{ (mV)}$	$\sigma_i \text{ (mV)}$
0	71.08	0
0.02	72.34	13.49
0.04	92.35	58.97
0.044	107.38	80.49
0.05	132.88	112.27
0.055	170.78	154.98
0.062	290.5	281.67

**Table 5.1: Standard Deviations for Low-Pass Filtered Impulsive Noise**

### 5.1.2 Impulse Rate

The goal of the impulse rate experiment is to measure, for different modulation indices, the threshold upcrossing rate as a function of threshold value for the low-pass filtered impulsive noise. The output of the low-pass filter circuit was connected to the input of the Threshold Detector as shown in Figure 5.10. The comparator output of the Threshold Detector was connected to a Fluke 1912A Multi-Counter to measure the threshold upcrossing rate, and the threshold itself was measured with a Fluke 75 Multimeter. The Fluke 1912A Multi-Counter is a standard electronic frequency counter and determines the average rate by counting the number of positive-going transitions in the comparator output for a specific sampling time and dividing the count by the sampling time. In the experiment, the threshold value was manually increased with the potentiometer dial on the Threshold Detector panel as the upcrossing rate and threshold voltage were recorded. The results of this procedure for a received optical power of 3.2 dBm are shown in Figure 5.11.

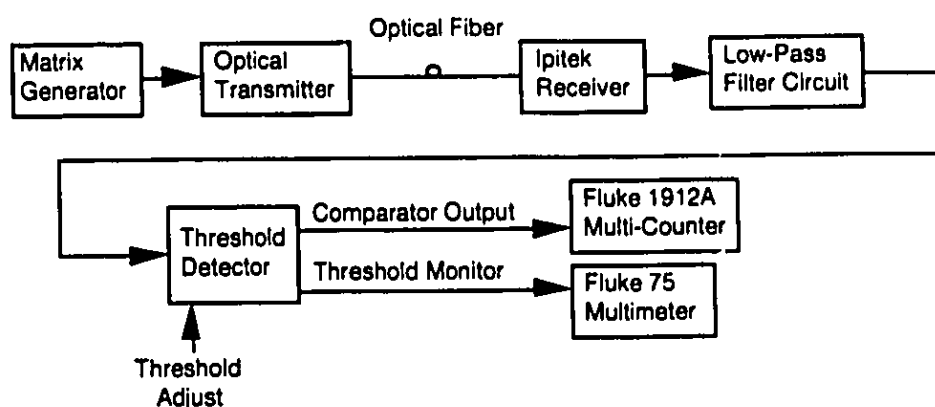


**Figure 5.10: Setup for Impulse Rate Experiment**

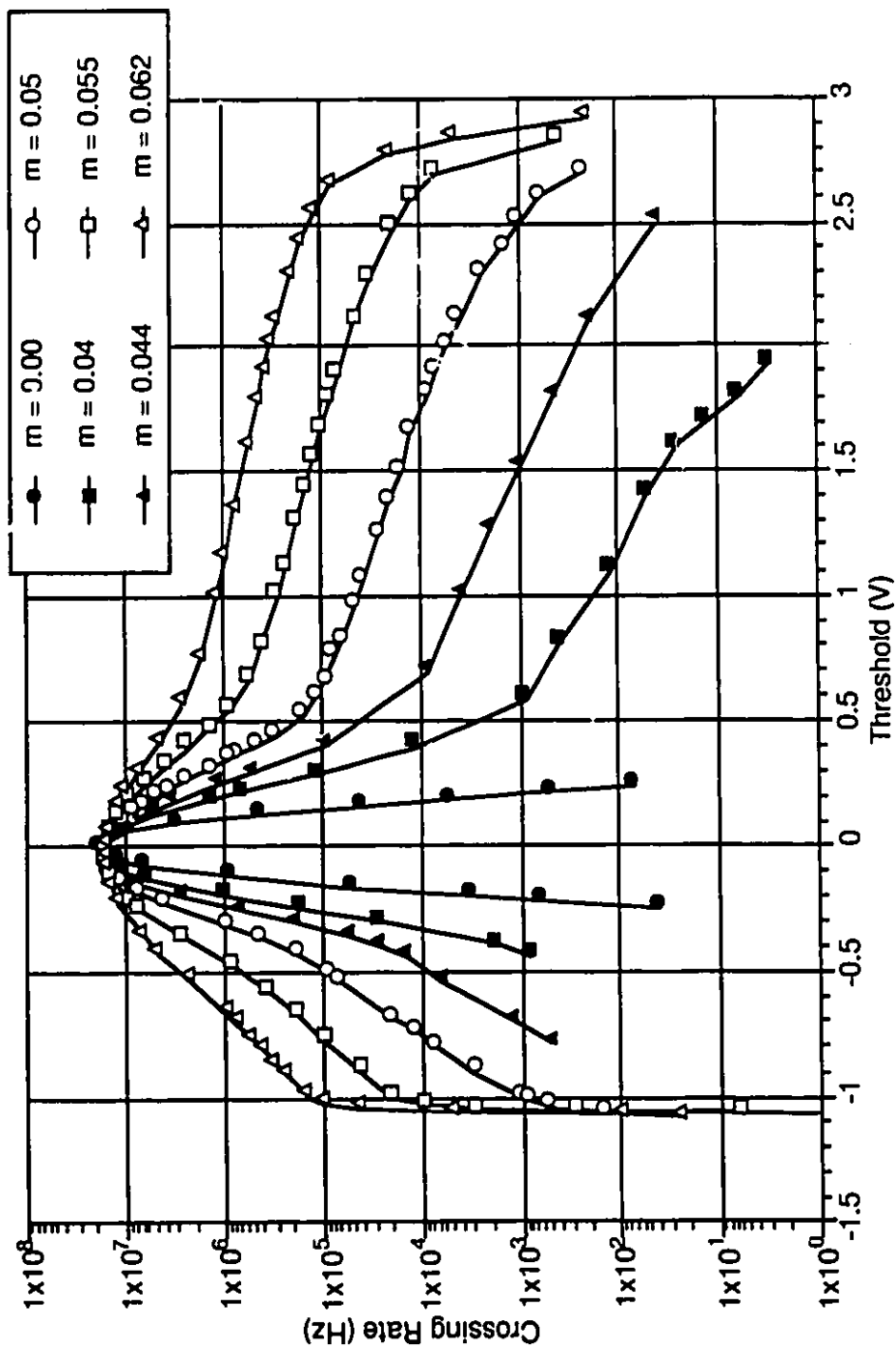
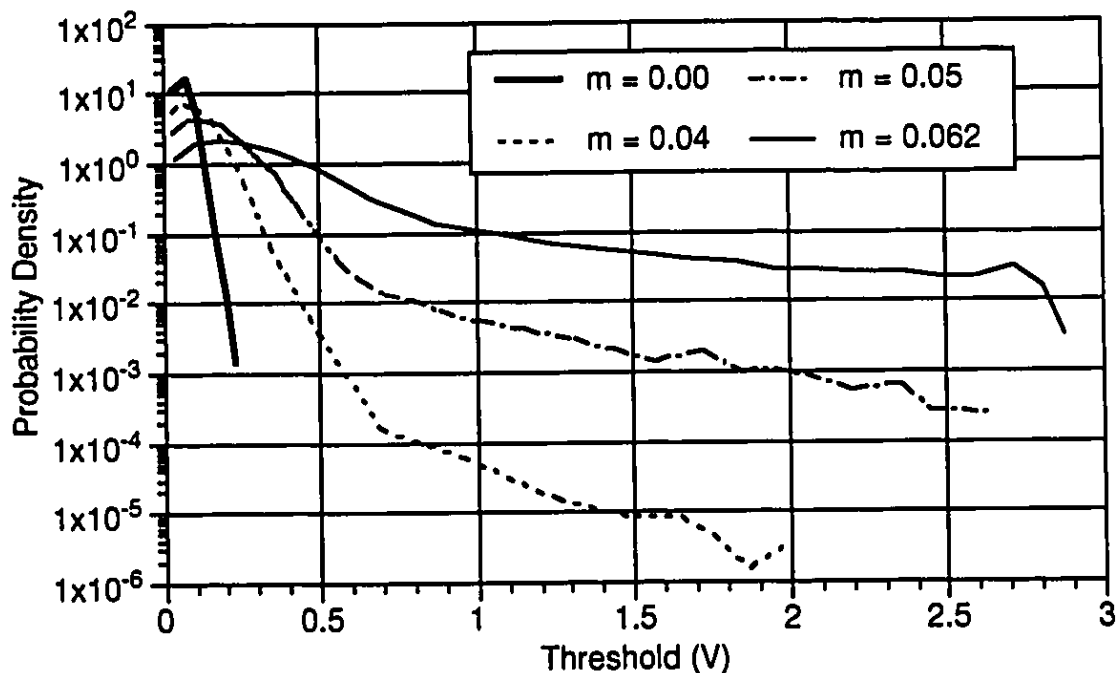


Figure 5.11: Threshold Upcrossing Rate vs. Threshold Voltage

In Figure 5.11, the effect of clipping is shown in the  $m = 0.04$  to  $m = 0.062$  curves to cause "angled floors" for positive threshold values. The curve for  $m = 0$ , which represents the threshold crossings of the system Gaussian noise, drops quite rapidly as the threshold voltage is increased. In contrast, the crossing rate is observed to decrease much slower for the cases where high modulation indices induce clipping at the transmitter. Another interesting observation is that the rate curves for the modulated cases are non-symmetrical about the zero threshold point. The rates for positive threshold values are considerably higher than the rates for corresponding negative threshold values which is a consequence of the single-sided nature of the laser threshold clipping. Because the error signal, which is equal to the negative of the SCM signal during clipping, is represented by a series of positive amplitude impulses, the low-pass filter output consists of positive-oriented impulse responses. These positive-oriented impulse responses cause higher threshold crossing rates for positive threshold values. Another distinct feature of the crossing rate curves for the modulated cases is the sharp drop above and below the threshold values of 2.5 V and -1 V, respectively. To explain this characteristic, one should consider that the largest value excursion in an SCM signal is limited by the sum of the amplitudes of all the carriers. For example, if  $I_{in}(t)$  is the modulating signal consisting of a sum of cosines as in equation (3.2), then the amplitude of  $I_{in}(t)$  is limited by  $|I_{in}(t)| \leq NI_{peak}$  which means that the maximum amplitude possible for a clip will be  $I_{max} = NI_{peak} - I_{th}$ . The fact that the amplitude of the clips is limited by a maximum value also means that there will be a maximum size impulse response. It is suggested that the drops at 2.5 V and -1 V are, respectively, due to the highest and lowest point of the maximum size (and positively-oriented) impulse response.

If it is assumed that each threshold upcrossing represents an excursion in the noise signal, then we can use the threshold crossing rate data of Figure 5.11 to approximate the probability density of the excursion amplitude. The excursion amplitude is defined as the maximum voltage that the input noise signal reaches between a threshold upcrossing and

subsequent downcrossing event. The probability density of the excursion amplitude should not be confused with the probability density of the noise amplitude which was measured in Section 5.1.1. The excursion amplitude probability density shows what the peak voltage of each excursion is likely to be whereas the noise amplitude probability density, measured in Section 5.1.1, shows what the voltage of the noise signal is likely to be at any point in time. The process of deriving the probability density of excursion amplitudes is explained in Appendix D. Figure 5.12 shows the result of applying this procedure to the crossing rate data for modulation indices of 0, 0.04, 0.05 and 0.062. As expected, the probability of large amplitude excursions is higher for larger modulation indices.



**Figure 5.12: Probability Density of Excursion Amplitudes for Low-Pass Filtered Impulsive Noise**

If we assume that each excursion represents a filter impulse response, then the curves of Figure 5.12 represent probability density of the impulse response amplitude.

According to basic signal and systems theory [52], the impulse response amplitude is proportional to the area of the stimulating impulse therefore the curves of Figure 5.12 can be compared to the theoretical probability density of the impulse area in the error process. This comparison is shown in Figure 5.13 where equation (C.4) from Appendix C was used with equations (3.13) and (3.15) to generate the theoretical impulse area curves. The value for  $c_2$  in equation (C.4) was not easily traceable to experimental parameters so a suitable value ( $c_2 = 9 \times 10^{26}$ ) was found by trial and error. It can be seen from Figure 5.13 that, although the curves for impulse area have the same downward trend as the excursion amplitude curves, they do not follow them exactly. This discrepancy is attributed to the somewhat inaccurate assumptions of one-to-one correspondences between: 1) threshold upcrossings and excursions; and 2) excursions and filter impulse responses. The effects of additive Gaussian noise in the experiment also contribute to the discrepancy.

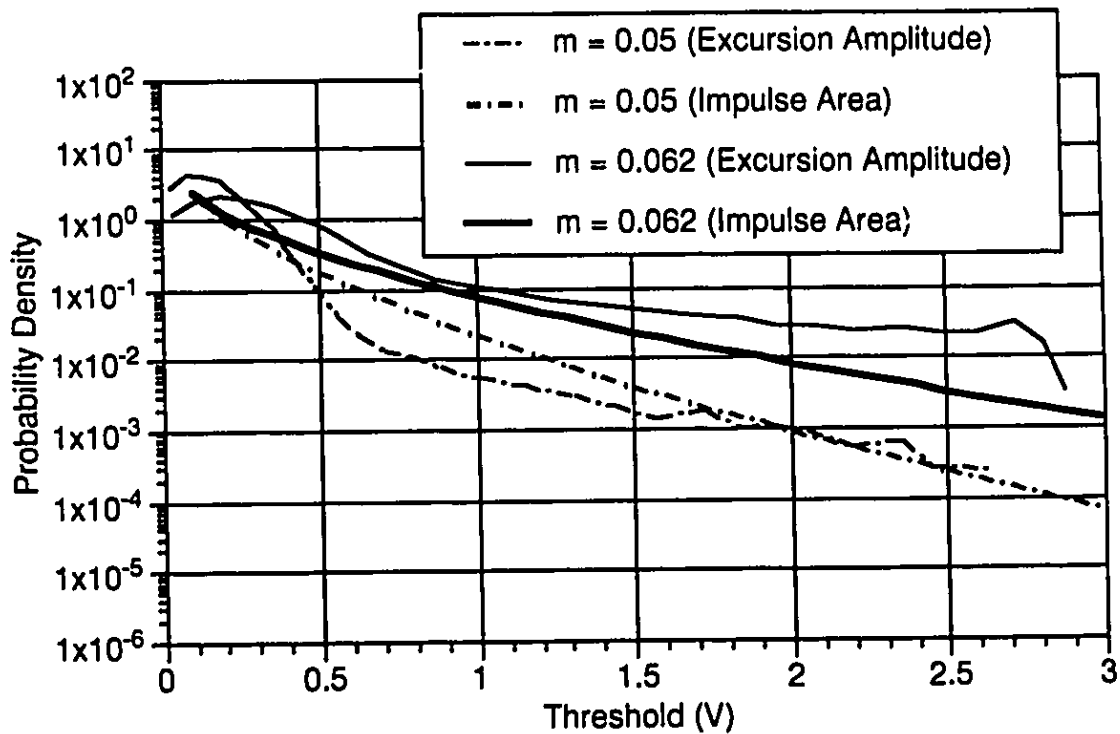


**Figure 5.13: Comparing Probability Densities of Experimental Noise Excursion Amplitude to Theoretical Impulse Area**



### 5.1.3 Time Distribution

In this experiment, we investigate the probability density of the time interval between consecutive threshold upcrossings in the low-pass filtered impulsive noise. It is anticipated that the information obtained about the time interval between the impulsive noise excursions will reveal how the clipping events at the transmitter are distributed in time. As mentioned in Section 5.1, the correspondence between a clipping event and a threshold crossing is not strictly one-to-one, therefore there is some degree of uncertainty in correlating the time distribution of clipping to the results obtained in this experiment.

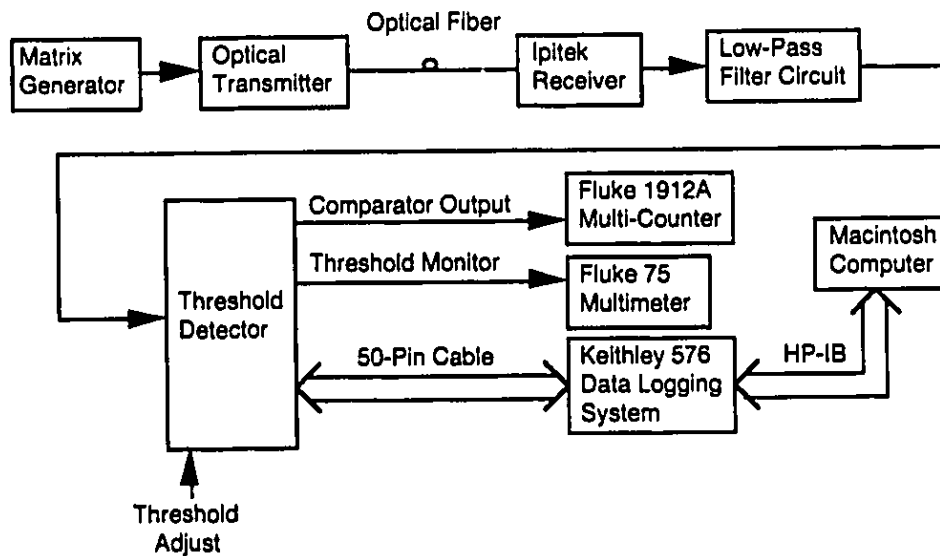


**Figure 5.14: Setup for Time Distribution Experiment**

The setup of Figure 5.14 was used to repeatedly sample the interval between upcrossings. The TTL inputs and outputs to the Time Interval Sampler in the Threshold Detector were controlled using a Keithley 576 Data Logging Device. The automation of the time interval sampling was accomplished with an HP-IB connection and a Labview program on the Macintosh computer. The Fluke 1912A Multi-Counter was connected to

the comparator output to obtain readings for the threshold upcrossing rate. Theoretically, the upcrossing rate measured by the Multi-Counter should be equivalent to the value obtained by taking the reciprocal of the average time interval sample. In the experiments, however, it was observed that the Multi-Counter rates were up to 8 times larger than this value for sample sizes of 5000. This discrepancy is attributed to the nonideal performance of the Threshold Detector hardware and the different threshold crossing sensitivities of the Time Interval Sampler and the Fluke 1912A Multi-Counter. The results of the sampling for a received optical power of 1.8 dBm are shown in histogram form in Figures 5.15 to 5.18. All of the histograms have a sample size of 5000. Figures 5.15 to 5.17 show the time distribution of threshold crossings for  $m = 0.05$  and threshold values of 0.2 V, 0.24 V, and 0.4 V. Figure 5.18 shows the time distribution for  $m = 0.062$  and a threshold of 1.0 V. The Multi-Counter rate measured for each case is also included with the figures.

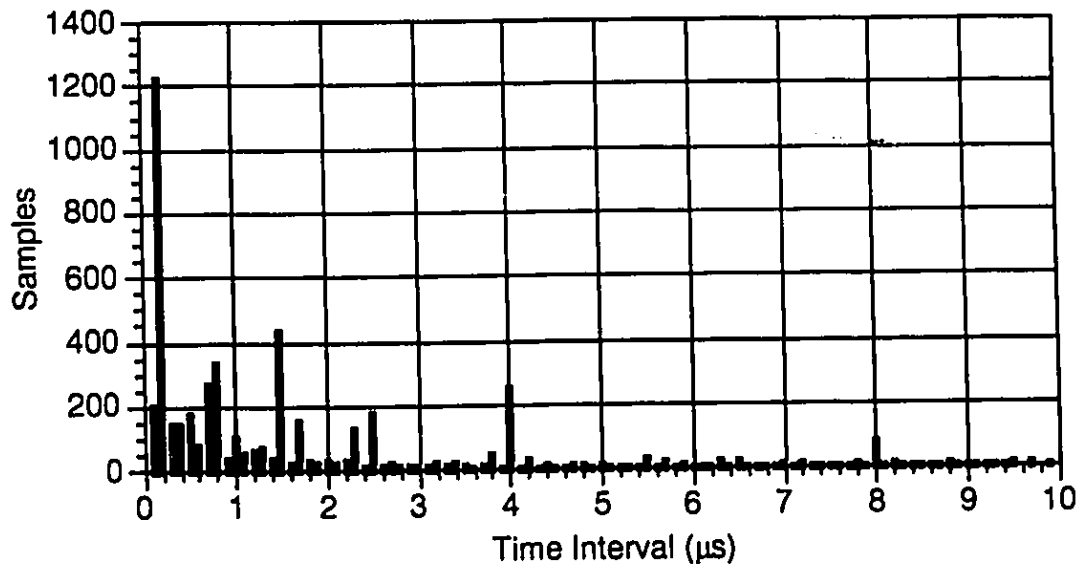


**Figure 5.15: Time Interval Histogram for 0.2 V Threshold.**  
**Sample Size = 5000, Multi-Counter Rate = 1.1 MHz, and  $m = 0.05$ .**

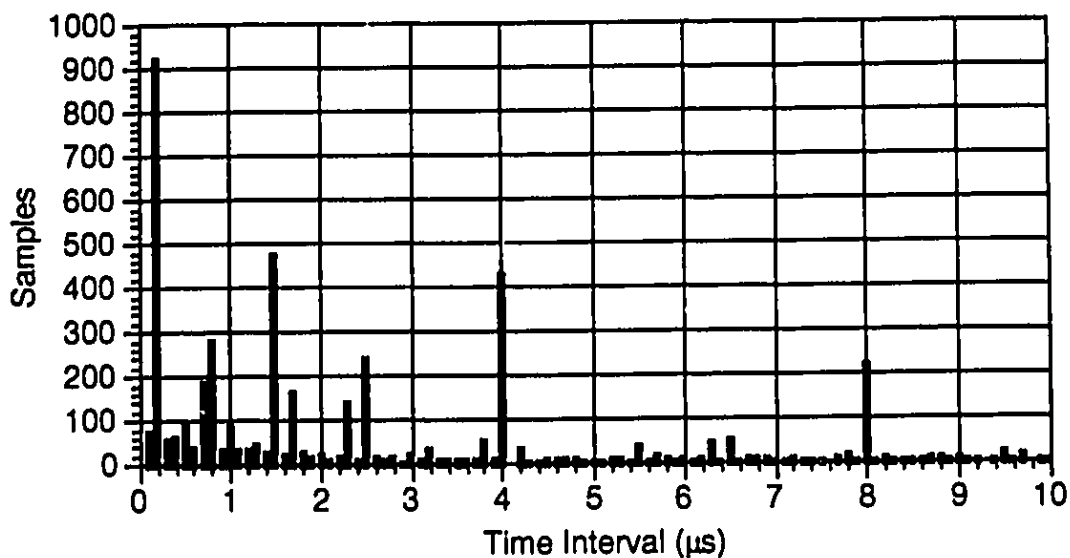


**Figure 5.16: Time Interval Histogram for 0.24 V Threshold.**  
**Sample Size = 5000, Multi-Counter Rate = 670 kHz,**  
**and  $m = 0.05$ .**

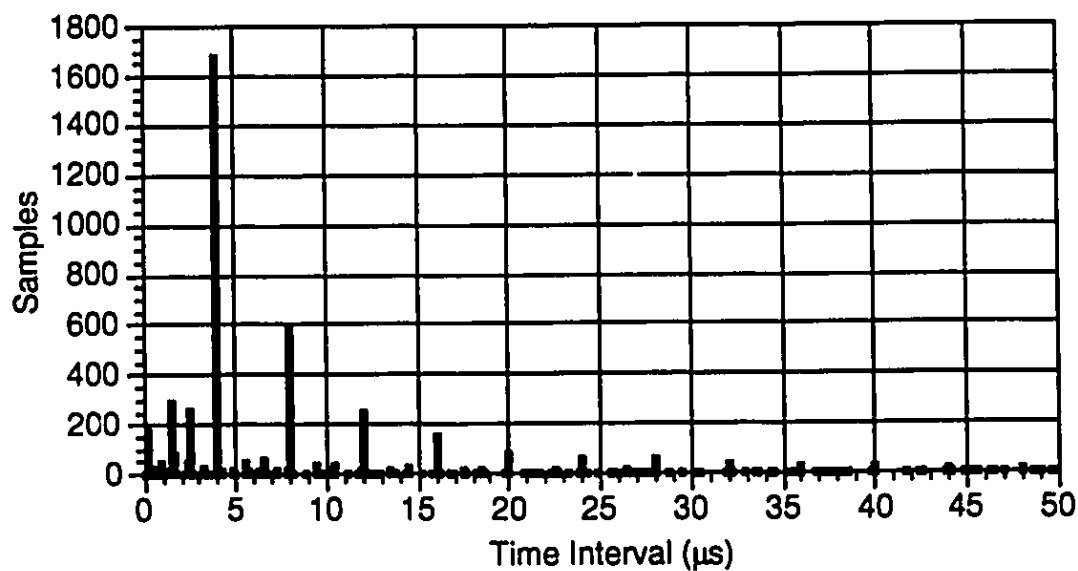


**Figure 5.17: Time Interval Histogram for 0.4 V Threshold.**  
**Sample Size = 5000, Multi-Counter Rate = 95 kHz,**  
**and  $m = 0.05$ .**

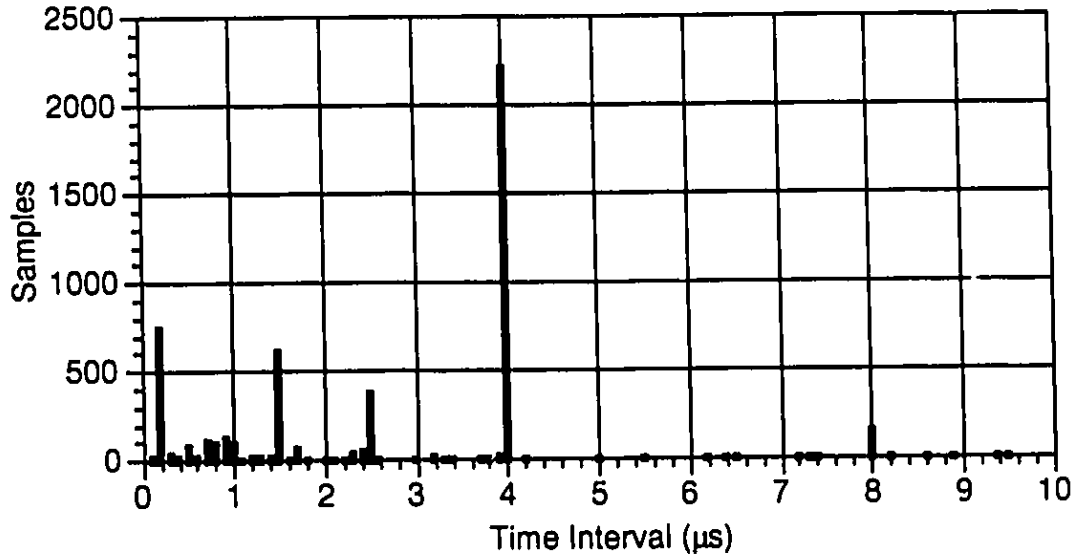


**Figure 5.18: Time Interval Histogram for 1.0 V Threshold.**

**Sample Size = 5000, Multi-Counter Rate = 582 kHz,**

**and  $m = 0.062$ .**

From the histograms, it can be seen that the excursion time distribution is not a smooth function, and there exist distinct times after an excursion where the next excursion is more likely to occur. This seems to contradict the assumption that the clipping events are Poisson distributed independent time events. If each impulsive noise excursion represented a clipping event, and the clipping events were Poisson distributed, then the time interval between consecutive excursions would have the following exponential probability distribution [61]:

$$p(\tau_i) = \lambda e^{-\lambda \tau_i} \quad (5.5)$$

where  $\tau_i$  is the time interval between excursions. To provide a comparison,  $p(\tau_i)$  is plotted in Figure 5.19 where the Poisson arrival rate  $\lambda$  is set to the inverse of the average time interval in Figure 5.15.

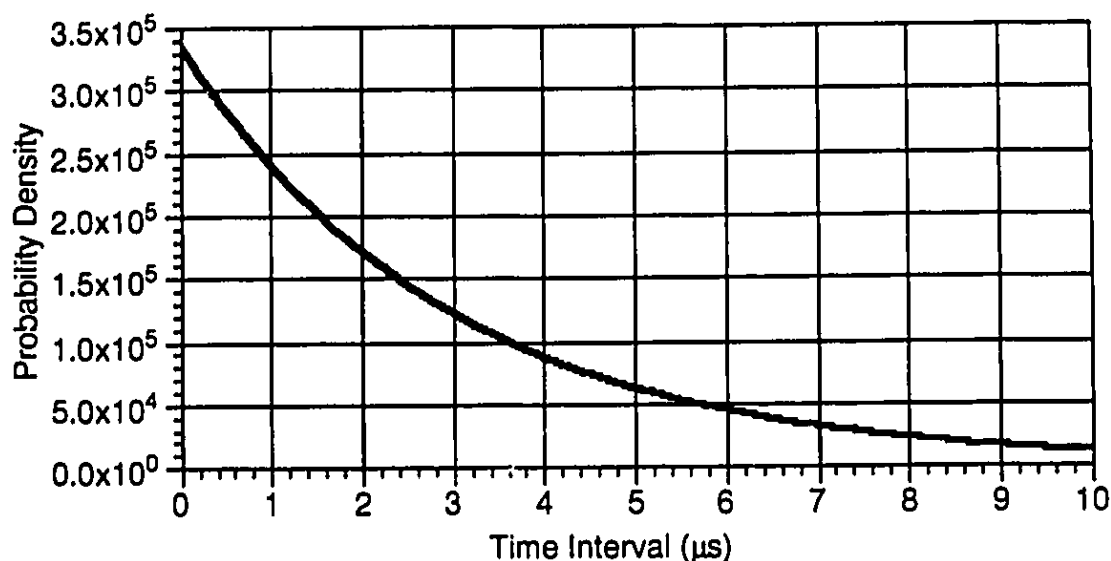


**Figure 5.19: Time Interval Probability Density for a Poisson Process  
with  $1/\lambda = 2.97 \mu s$**

In Figures 5.15 to 5.18, it is observed that the time interval probability is distinctly pronounced at durations of 160 ns, 1.5  $\mu s$ , 4  $\mu s$ , and multiples of 4  $\mu s$ . The 160 ns and 1.5  $\mu s$  durations are observed to be more dominant for lower threshold values. To explain the dominant 160 ns interval, we observe that  $1/160ns = 6.25MHz$ . Considering the fact that the 50 MHz TTL time interval counter in the Threshold Detector has a resolution of 20 ns, it has been concluded that the 160 ns samples are in fact be caused by a  $1/6MHz = 167ns$  time interval. The frequently-occurring  $1/6MHz$  time interval between clips is directly is related to the 6 MHz spacing between adjacent carriers in the NTSC frequency plan. The frequently-occurring 1.5  $\mu s$  interval is related to the carrier frequencies of Channels 5 and 6 which are not exactly 6 MHz apart from the rest of the carriers. A more detailed explanation of the cause of the dominant 167 ns and 1.5  $\mu s$  intervals is given in Appendix E. From Figures 5.17 and 5.18, it is apparent that, for larger threshold levels, the 4  $\mu s$  duration becomes the dominant time interval. This is a

consequence of the periodic nature of the modulating SCM signal. By observing that the inverse of  $4\ \mu\text{s}$  is  $1/4\ \mu\text{s} = 250\text{kHz}$  and that each carrier frequency is an integer multiple of 250 kHz (Channel 2 = 55.25 MHz, Channel 3 = 61.25 MHz, Channel 4 = 67.25 MHz, etc.), then it is obvious that all the carrier oscillators undergo an integer number of periods in the span of  $4\ \mu\text{s}$ . The entire (unmodulated) SCM signal is therefore periodic, and it is reasonable to suggest if the sum of the carrier amplitudes cause the laser drive current to fall below threshold at particular instant in time, then another clip will likely occur  $4\ \mu\text{s}$  later. The element of predictability in clipping occurrences revealed in this experiment may possibly be exploited by implementing the appropriate error correcting measures when a digital channel is multiplexed with the analog channels in a hybrid system.

## 5.2 Down-Converter Experiments

The experimental setup shown in Figure 5.20 was used to investigate the amplitude probability density of down-converted impulsive noise. The HP 8753A network analyzer was used to select the frequency of the (vacant) channel to be down-converted, and the bandpass filter in the down-converter limited the impulsive noise to a bandwidth of 15 MHz. The Intermediate Frequency (IF) of the output impulsive noise was controlled by the HP 8642A signal generator.

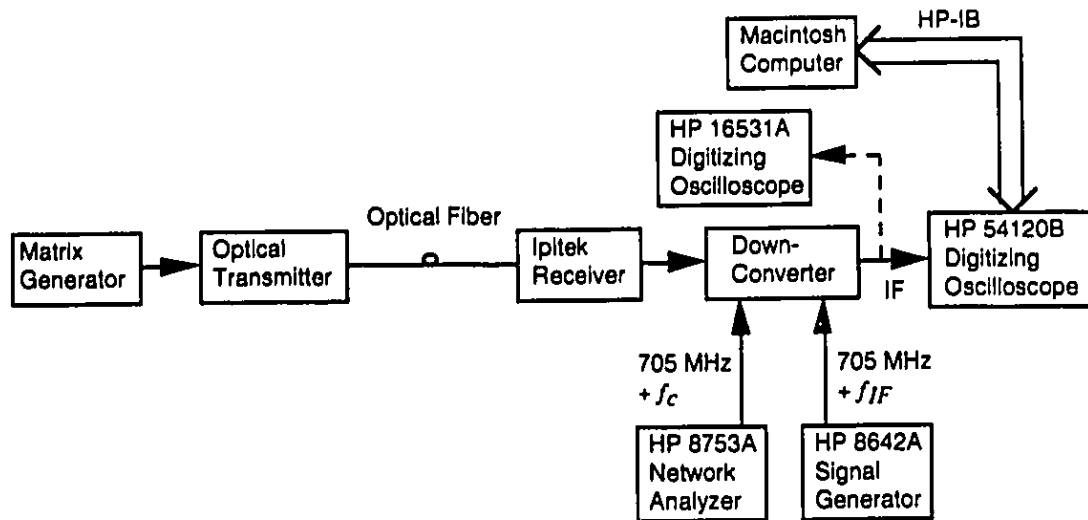


**Figure 5.20: Setup for Down-Converter Experiment**

### 5.2.1 Qualitative Nature of Down-Converted Impulsive Noise

To determine the qualitative nature of down-converted impulsive noise, the HP 16531A Digitizing Oscilloscope was used to capture time domain waveforms of the IF output. Sample waveforms for a channel frequency of  $f_c = 417\text{ MHz}$  and an IF frequency of  $f_{IF} = 44\text{ MHz}$  are shown in Figures 5.21 to 5.23 where the time resolution has been increased for each successive figure. In Figure 5.21, the impulsive noise contains large excursions with varying amplitudes occurring randomly in time. The increased time scale in Figures 5.22 and 5.23 reveal the presence of oscillations inside each excursion envelope. The validity of the bandpass filter model developed in Chapter 3 is reinforced by comparing these waveforms to the bandpass filter impulse response of Figure 3.15 which is quite similar. It is noted that the period of the oscillations in Figure 5.23 is about 22 ns which corresponds to the period of the 44 MHz intermediate frequency.

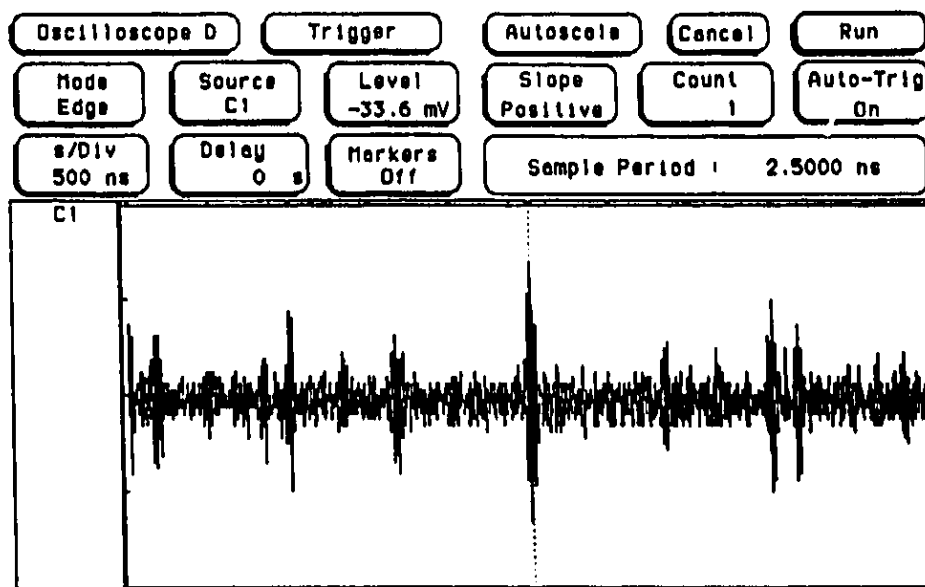


Figure 5.21: Sample Waveform of Down-Converted Impulsive Noise.  
500 ns/div,  $f_c = 417$  MHz,  $f_{IF} = 44$  MHz, and  $m = 0.05$ .

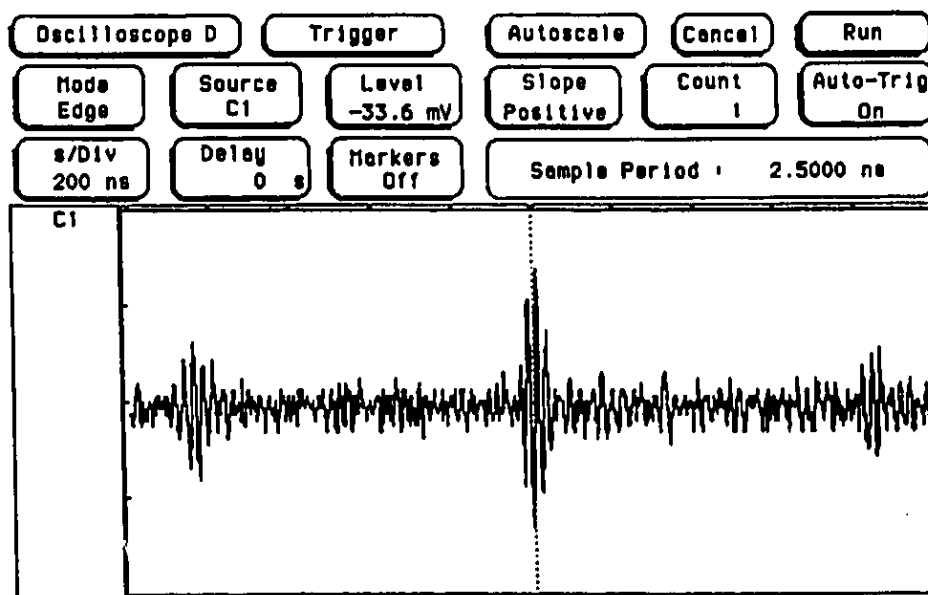
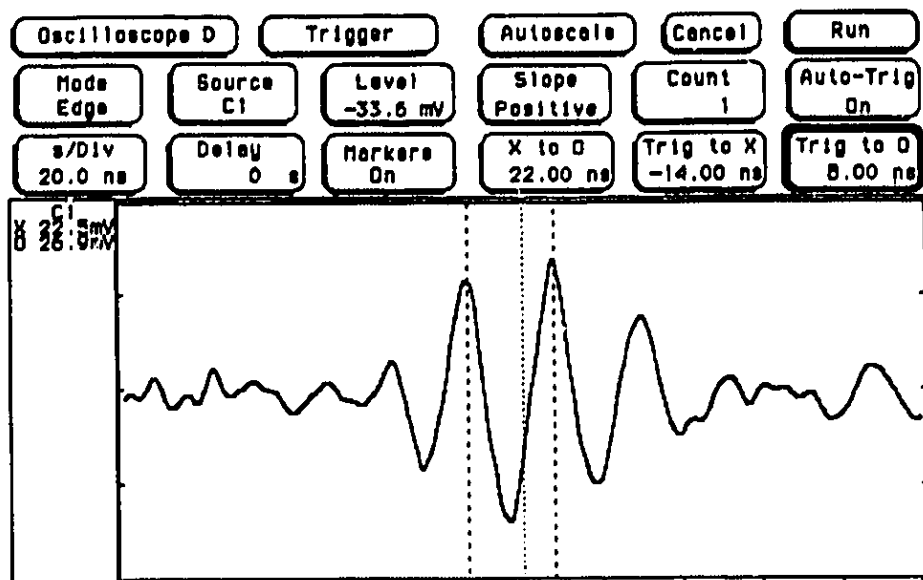


Figure 5.22: Sample Waveform of Down-Converted Impulsive Noise.  
200 ns/div,  $f_c = 417$  MHz,  $f_{IF} = 44$  MHz, and  $m = 0.05$ .





**Figure 5.23: Sample Waveform of Down-Converted Impulsive Noise.**  
 20 ns/div,  $f_c = 417$  MHz,  $f_{IF} = 44$  MHz, and  $m = 0.05$ .

### 5.2.2 Amplitude Distribution

To determine the experimental amplitude probability density of down-converted impulsive noise, the HP 54120B Digitizing Oscilloscope was used to obtain representative histograms of the down-converter output. A center frequency of  $f_c = 549$  MHz, which corresponds to Channel 78 in the NTSC frequency plan, was chosen to be down-converted to intermediate frequencies of 70 MHz and 0 MHz. The received optical power at the photodetector was 1.6 dBm.

The amplitude probability densities for the cases of  $m = 0, 0.04, 0.05$ , and  $0.062$  are shown in Figure 524 for  $f_{IF} = 70$  MHz. The measured standard deviations of the total noise and the impulsive noise are also given in Table 5.2. The intermediate frequency of 70 MHz was chosen because it is commonly used in the QAM modulators and demodulators that may be employed in hybrid systems.

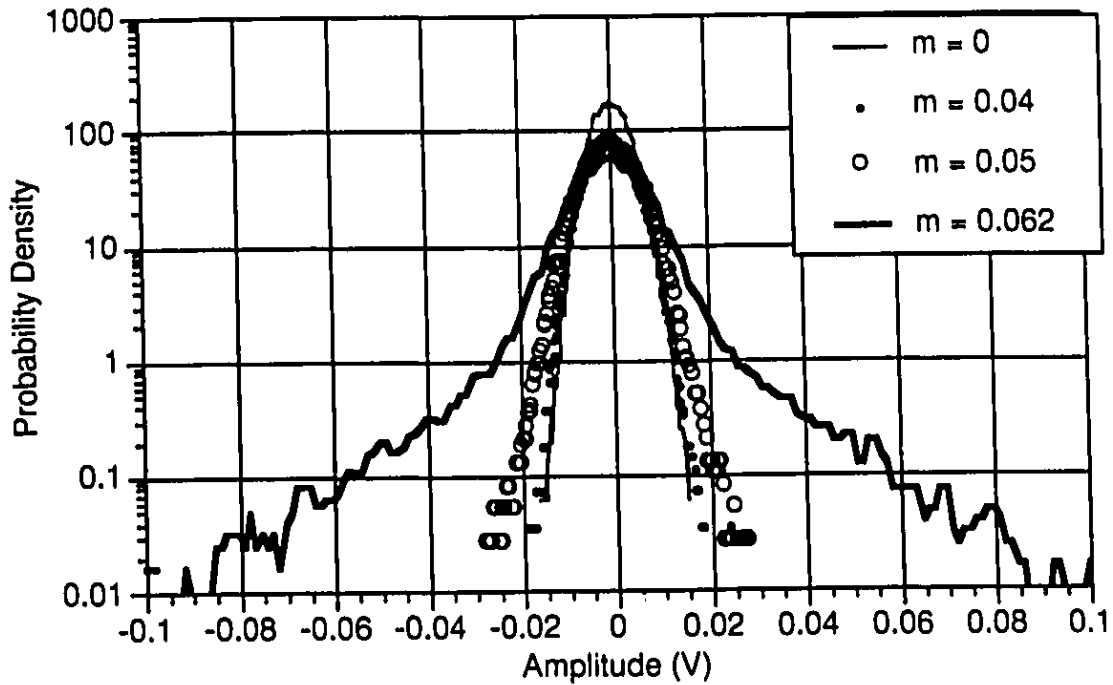


**Figure 5.24: Probability Density of Down-Converted Impulsive Noise.**  
 $f_c = 549$  MHz and  $f_{IF} = 70$  MHz.

$m$	$\sigma_{tot} (mV)$	$\sigma_i (mV)$
0	3.819	0
0.02	3.82	0.096
0.04	4.378	2.14
0.044	4.71	2.756
0.05	5.426	3.854
0.055	6.733	5.544
0.062	10.43	9.707

**Table 5.2: Standard Deviations for Down-Converted Impulsive Noise.**  
 $f_c = 549$  MHz and  $f_{IF} = 70$  MHz.

The intermediate frequency was also set to  $f_{IF} = 0$  MHz to determine the probability density of impulsive noise at baseband. The curves obtained are shown in Figure 5.25 and the standard deviations are listed in Table 5.3. If the down-converted channel were used to

transmit a digital signal, a curve in Figure 5.25 would represent the probability density of the noise at the input of the decision circuit in the demodulator.

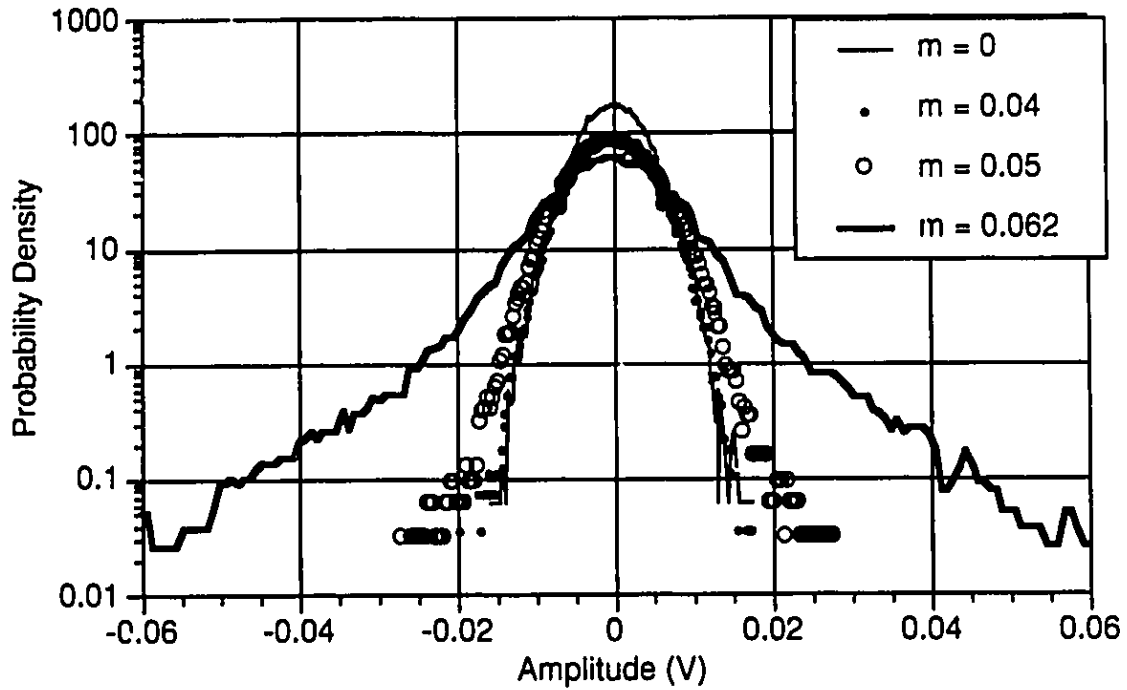


**Figure 5.25: Probability Density of Down-Converted Impulsive Noise.**  
 $f_c = 549$  MHz and  $f_{IF} = 0$  MHz.

$m$	$\sigma_{tot} (mV)$	$\sigma_i (mV)$
0	3.788	0
0.02	3.832	0.584
0.04	4.189	1.79
0.044	4.393	2.226
0.05	4.864	3.052
0.055	5.803	4.397
0.062	8.555	7.671

**Table 5.3: Standard Deviations for Down-Converted Impulsive Noise.**  
 $f_c = 549$  MHz and  $f_{IF} = 0$  MHz.

Using the curves obtained for  $f_{if} = 70\text{MHz}$  and  $f_{if} = 0\text{MHz}$ , it is possible to investigate the effect of IF frequency on the down-converted impulsive noise distribution. In Figure 5.26, the curves for  $m = 0.062$  for both intermediate frequencies are superimposed to provide a comparison. It is apparent from the graph that an intermediate frequency of 70 MHz causes the tail area of the distribution to be slightly higher than the case of 0 MHz.

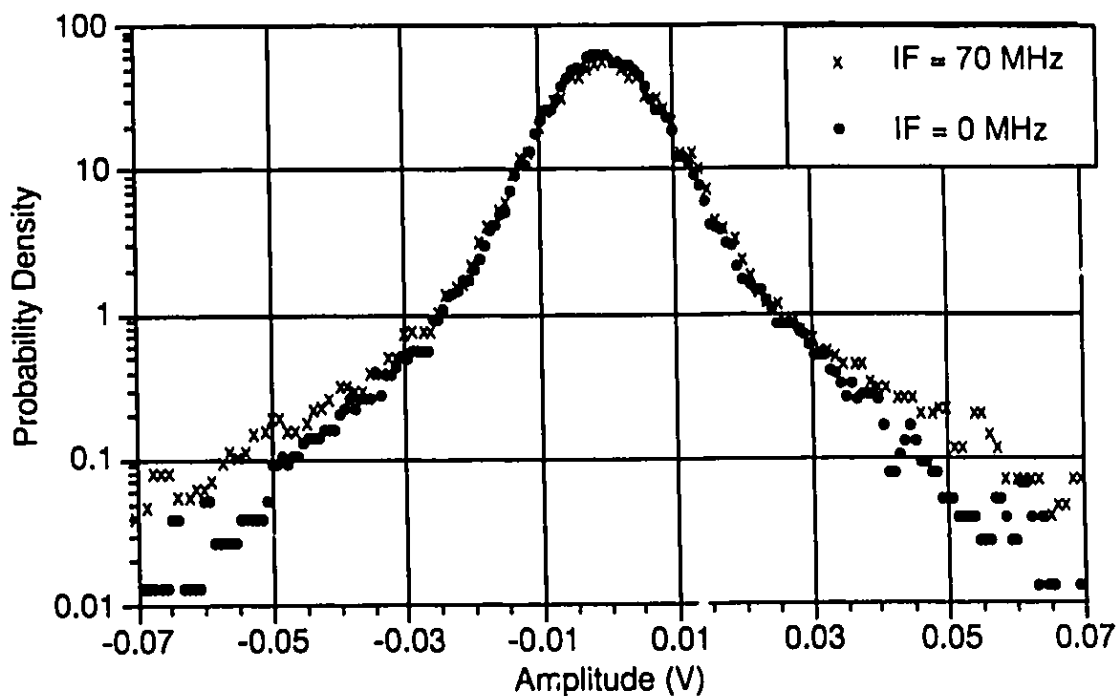


**Figure 5.26: Effect of Intermediate Frequency on Probability Density**  
 $m = 0.062$

Because the curves in Figure 5.25 represent the amplitude probability of the impulsive and Gaussian noise at the input to a decision circuit, they can be compared to the theoretical model developed in Section 3.3.4. In Figure 5.27, the experimental probability distribution for  $m = 0.062$  is compared to the theoretical distribution obtained by performing an Inverse Fourier Transform of equation (3.44). Equation (3.33) was used

for the characteristic function of Gaussian noise with the variance set to the square of the standard deviation of the  $m = 0$  case in Table 5.3. The impulse response of the 15 MHz bandpass filter in the down-converter was approximated by a rectangular pulse having a time duration of  $1/15\text{MHz} = 66.7\text{ns}$ . With the value of  $\sigma_i$  from Table 5.3, equation (3.42) was used to obtain a suitable value for  $\overline{A^2}$  which was used in equation (3.18) and (3.53) to obtain the characteristic function of the impulsive noise process. A program implemented in Mathematica (which is shown in the Appendix) was used to calculate the theoretical probability density of the down-converted impulsive noise. It can be seen from Figure 5.27 that the model deviates significantly from the experimental distribution at low amplitude values. However, in the tail regions of the curves which correspond to large but infrequent excursions, the comparison between the theoretical model and the experimental result is quite close. It is interesting to note that a Gaussian distribution seems to model the experimental probability density quite adequately in the small amplitude region whereas the impulsive noise model is more accurate in the large amplitude region. It is observed that shape of the theoretical curve is similar to the characteristic amplitude distribution of impulsive noise with a large central lobe and pronounced tail regions.

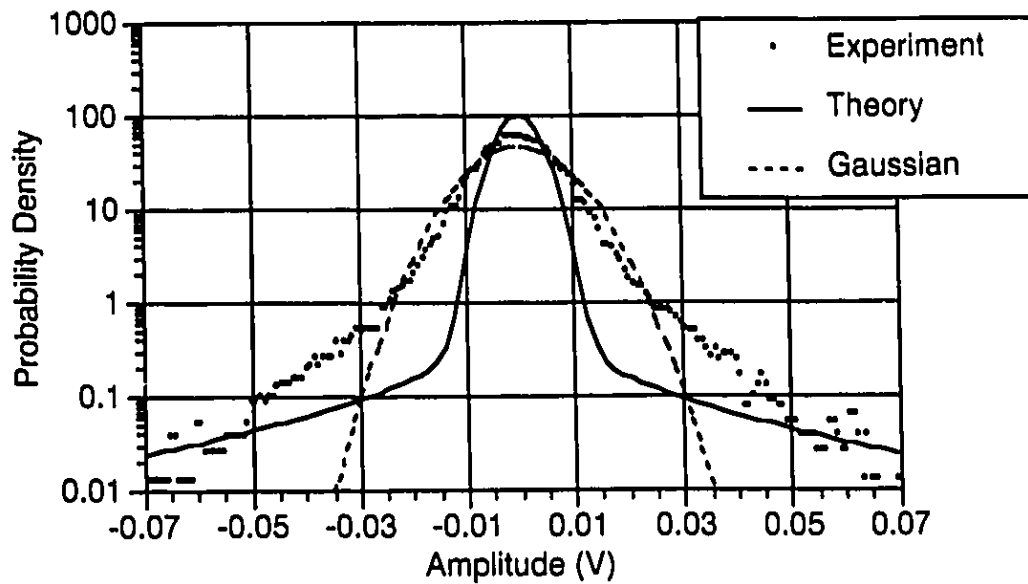


**Figure 5.27: Theoretical and Experimental Probability Density**  
 $m = 0.062$

To provide an interesting comparison, the theoretical curve of Figure 5.27 was adjusted to match the experimental curve in the central lobe region. This was accomplished by increasing the standard deviation of the Gaussian noise component to  $\sigma_g = 7mV$  and decreasing the standard deviation of the impulsive noise component to  $\sigma_i = 4.9mV$  such that the standard deviation of the total noise was still  $\sigma_{tot} = 8.555mV$ . The result of this adjustment is shown in Figure 5.28 where the theoretical probability density is observed to follow the experimental data quite closely.

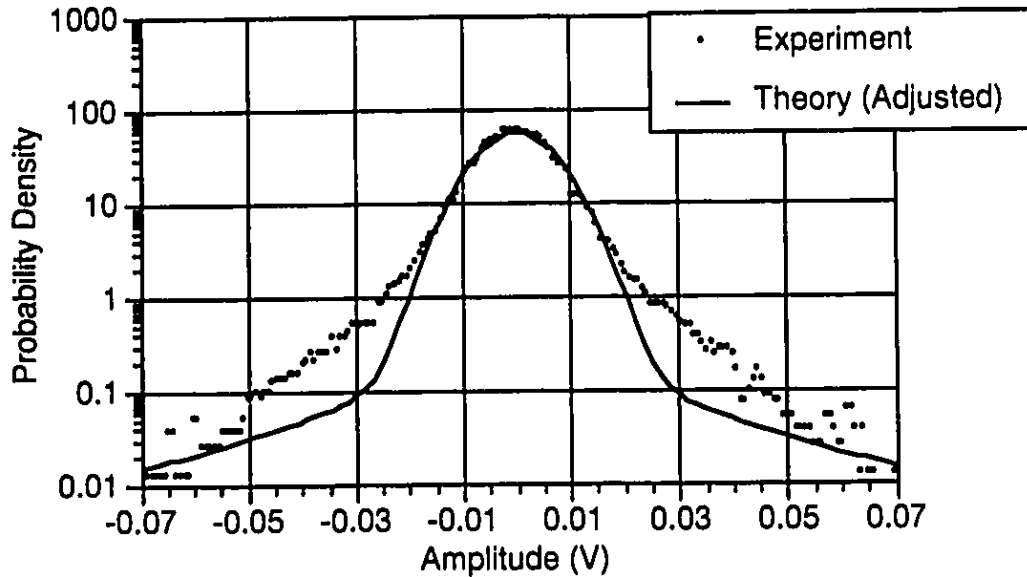


**Figure 5.28: Adjusted Theoretical and Experimental Probability Density**  
 $m = 0.062$

### **5.3 Broadening of the Main Lobe in the Amplitude Distributions of Low-Pass Filtered and Down-Converted Impulsive Noise**

It has been observed that increasing the modulation index results in broadening of the main lobe of the experimental amplitude probability density for both low-pass filtered and down-converted impulsive noise. The agreement between the main lobe region and the adjusted theoretical curves of Figure 5.9 and Figure 5.28 seems to suggest that the main lobe is strongly related to the amount of Gaussian noise in the system. It was shown in Figure 5.28 that the theoretical probability density matched the experimental density quite well when the Gaussian noise component was increased in the theoretical model. A possible explanation for this result is that the additional noise power when increasing the modulation index may not be entirely due to laser diode clipping. Nonlinearities from other components in the system such as amplifiers, connectors, and nonideal electronic components may have contributed to the additional noise power seen when increasing the modulation index. As these additional nonlinearities may not involve a hard limiting

mechanism, their contribution to the noise in the receiver may be non-impulsive. In fact, the distribution of nonlinear distortion due to sources other than laser diode clipping may be accurately predicted with a Gaussian model. To limit the scope of this thesis, the contribution of these other nonlinearities was not accounted for in the theoretical development in Chapter 3. However, it is suggested that further investigation of the amplitude probability density of non-impulsive nonlinear distortion might be useful for developing of a complete noise model that accounts for the contributions of Gaussian, nonlinear impulsive, and nonlinear non-impulsive noises.

#### 5.4 BER Impairment in an AM-VSB/64-QAM Hybrid System

In this section, the BER predicted by the theoretical model is compared to the BER of a 64-QAM signal in an experimental AM-VSB/QAM hybrid lightwave system. The implementation of the hybrid system and the BER measurements were performed by Kinh Pham, a former graduated student at TRLabs, as part of his work towards an M.Sc. thesis. The block diagram of the hybrid system in Figure 5.29 [9] shows the QAM channel being upconverted to a channel frequency of 417 MHz, frequency division multiplexed with 42 unmodulated AM channels, and down-converted and demodulated at the receiver.

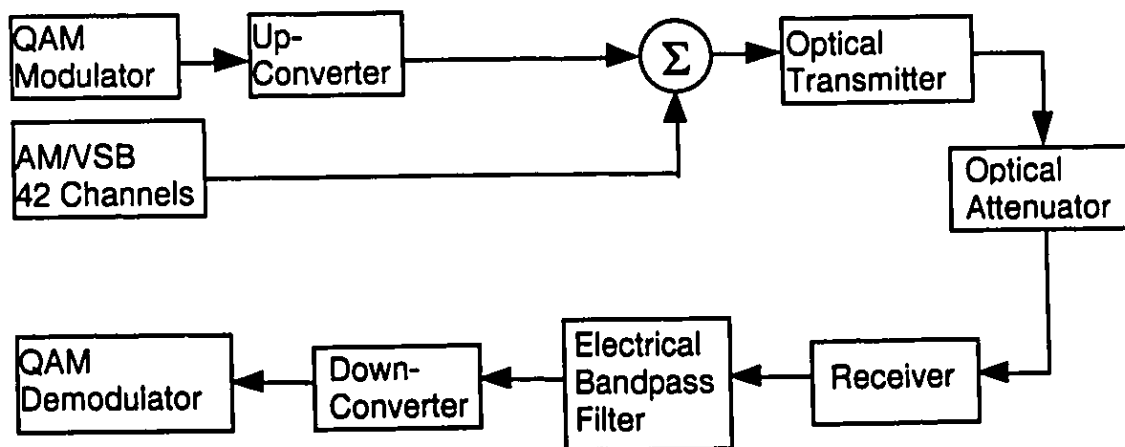


**Figure 5.29: Experimental AM-VSB/64-QAM Hybrid System**



In the experiments on the hybrid system, the BER of the QAM channel was measured as a function of QAM modulation index for different AM modulation indices. Two sets of experimental and theoretical curves corresponding to AM channel modulation indices of 0.05 and 0.06 are given in Figure 5.30. The BER curves predicted by Middleton's Class A model [62] are also included to provide a comparison. The application of Middleton's Class A model, which is a generalized analytical model for combined Gaussian and impulsive noise, was initially performed by Kinh Pham [9]. It is of relevance to note that the application of Middleton's model required a sampling of the impulsive noise at the QAM channel intermediate frequency to obtain the impulsive index, which is a parameter of the model. The curve for  $m = 0$  is also included in Figure 5.30 to show the BER limitation due to the intrinsic Gaussian noise in the system.

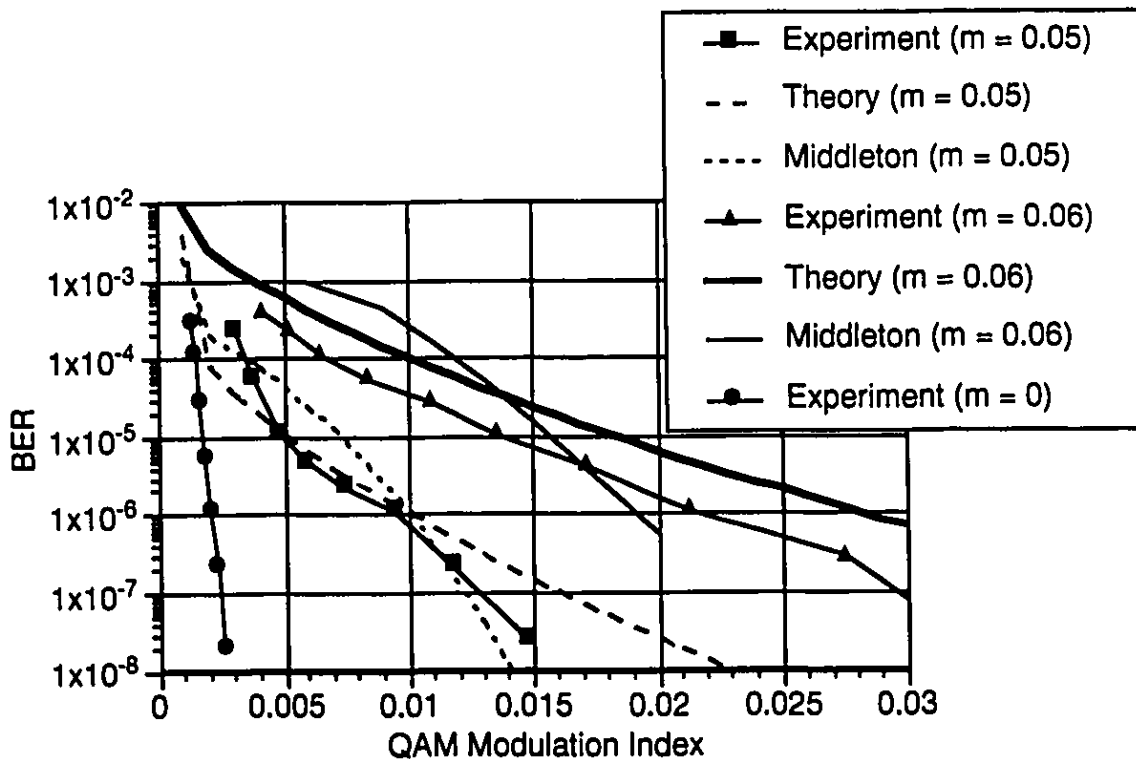


**Figure 5.30: BER vs. QAM Modulation Index in a Hybrid System**

It is observed that the penalty caused by clipping is quite severe and limits the effectiveness of increasing the QAM modulation index to improve the BER of the QAM channel. The theoretical BER predicted by the clipping-induced impulsive noise model is observed to follow the experimental results quite closely. Although Middleton's model does predict the BER to a certain extent, it appears to deviate from the experimental results as the QAM modulation index is increased. This is particularly evident in the curves for  $m = 0.06$  where the BER predicted by Middleton's model appears to be dropping significantly for QAM modulation indices above 0.02. In contrast, the BER curve predicted by the clipping-induced impulsive noise model appears to descend at the same rate as the experimental BER. The clipping-induced impulsive noise model does not follow the experimental result quite so closely for the case of  $m = 0.05$  which suggests that the model is more accurate for higher AM modulation indices. However, the clipping-induced impulsive noise model has the inherent advantage of not requiring an experimental sampling of the impulsive noise which is necessary if Middleton's model is used. This advantage makes the clipping-induced impulsive noise model an attractive tool for performing capacity studies on hybrid analog/digital systems where experimental measurements from an actual system may not be available.

Using the model for clipping-induced impulsive noise, we can also investigate the relationship between the BER of the QAM channel and the AM rms modulation index. Figure 5.31 shows the BER versus AM rms modulation index as predicted by the model for different values of QAM Signal-to-Noise (SNR) ratio. It can be seen that for 64-QAM systems with  $SNR > 30dB$ , the BER is largely dependent on the amount of AM rms modulation while, for a system with  $SNR \approx 20dB$ , this dependence is reduced due to the large Gaussian noise power.

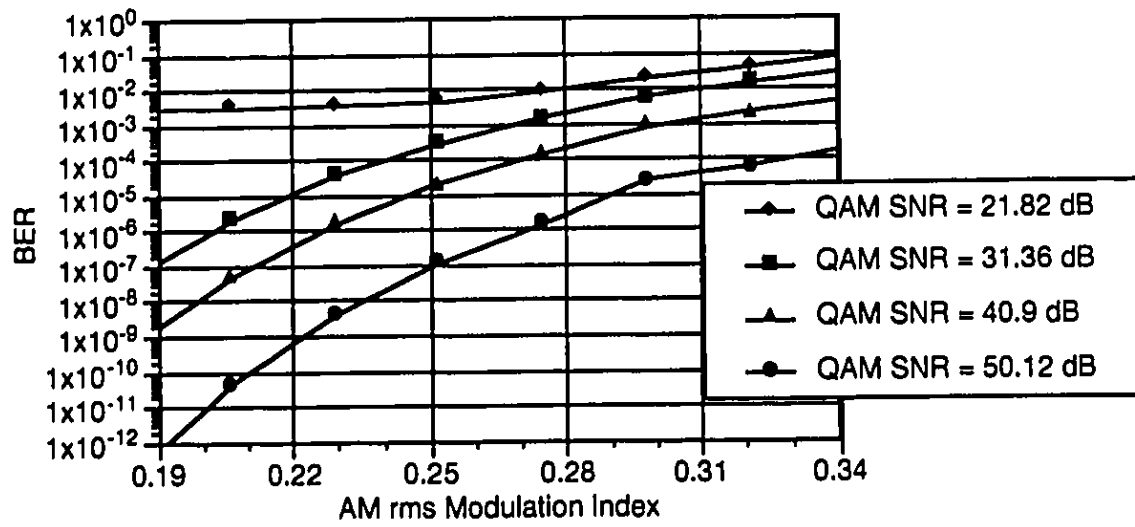


**Figure 5.31: Predicted BER for 64-QAM versus AM rms Modulation Index**

## 6. Conclusions

The purpose of this thesis has been to investigate the statistical and qualitative characteristics of clipping-induced impulsive noise in a subcarrier multiplexed lightwave system. The theoretical and experimental work performed has resulted in several conclusions on the nature of clipping-induced impulsive noise and has revealed some potential areas of future research.

### 6.1 Summary of Conclusions

Although the frequency domain analysis of clipping noise is now well established, the time domain approach presents a novel and more suitable method for characterizing the impulsive behavior of clipping noise as it appears in the receiver. In developing a clipping-induced impulsive noise model, the sequence of clips were represented by a Poisson train of parabolic pulses having random areas. To determine the time domain response of a narrowband channel, the clips were modeled as a Poisson train of impulse functions such that the noise waveform at the output of the channel selection filter consists of a sequence of impulse responses having random amplitudes and occurring at random points in time. By applying Rice's Shot Noise Model [53], a characteristic function for the filtered impulsive noise process can be derived. Using similar analysis, an expression can be obtained for the theoretical BER of an ASK or QAM channel in an analog/digital hybrid system.

Experimental measurements on low-pass filtered impulsive noise have demonstrated that the amplitude probability density of combined Gaussian and impulsive noise is close to Gaussian for small modulation indices ( $m \approx 0.02$ ) but significantly deviates from the Gaussian shape for modulation indices of 0.05 and higher. Measured threshold crossing rates have shown that excursions in the impulsive noise occur quite frequently and have large amplitudes compared to the excursions caused by the Gaussian

noise in the system. A time distribution experiment has revealed that the probability density of the time interval between consecutive impulsive noise excursions is not a smooth function but is distinctly pronounced at intervals of 167 ns, 1.5  $\mu$ s, 4  $\mu$ s, and multiples of 4  $\mu$ s. The correlation between consecutive excursions in low-pass filtered impulsive noise indicates that the clipping events of an unmodulated subcarrier multiplexed signal at the transmitter have similar statistics.

An experiment on down-converted impulsive noise has qualitatively verified the modeling of clipping-induced impulsive noise as a series of filter impulse responses. For large amplitudes, the probability density predicted by the theoretical model is close to the probability density obtained in the experiment. For small amplitudes, a Gaussian distribution is observed to predict the distribution adequately.

Finally, the theoretical model is observed to predict, within a factor of 10, the BER of a QAM channel in a AM-VSB/64-QAM hybrid system. Additional calculations with the model show that the BER is largely dependent on the amount of AM modulation for QAM SNRs above 30 dB.

## **6.2 Recommendations for Further Research**

As a consequence of the theoretical and experimental results of this project, some new ideas for further research have been spawned.

The degree of predictability of the time interval between impulses suggests that the bit error ratio of the digital channels in a hybrid system could be reduced by developing and applying an error correcting scheme that takes into account the expected time occurrence of clips. Before this approach is pursued, however, an investigation of the effect of carrier modulation on the time intervals should be performed as the experimental results were obtained with unmodulated carriers. It is anticipated that modulating the carriers will increase the degree of randomness of the time intervals, thus reducing the effectiveness of the error correcting code compared to the unmodulated case.

Considering that the QAM BER predicted by the clipping-induced impulsive noise model has been shown to be quite accurate, it is suggested that capacity studies can be performed to determine the optimal operating parameters for future analog/digital hybrid systems which must combine the requirements of high analog CNR and low digital BER. If the N-VSB format is accepted for HDTV broadcasting, the theoretical model developed in this thesis can be extended to N-VSB in order to predict the BER degradation due to clipping and Gaussian noise in the next-generation AM-VSB/HDTV hybrid lightwave systems.

## REFERENCES

- [1] C. N. Lo, H. E. Tohme, R. S. Wolff, "A Hybrid Architecture for Analog Video Broadcast and B-ISDN Services in Customer Premises Networks," *IEEE Journal on Selected Areas in Communications*, vol. 8, no. 7, pp. 1327-1339, Sept. 1990.
- [2] T. E. Darcie, "Subcarrier Multiplexing for Lightwave Networks and Video Distribution Systems," *IEEE Journal on Selected Areas in Communications*, vol. 8, no. 7, pp. 1240-1246, Sept. 1990.
- [3] C. Lin, S. Ovadia, W. T. Anderson, "Multichannel AM/QAM Video Lightwave Systems for Hybrid Fiber/Coax Distribution Networks," *IOOC 95 Technical Digest*, FC1-4, pp. 70-71.
- [4] S. S. Wagner, "Recent Progress in Fiber/Coax Local Access Networks," *OFC '95 Technical Digest*, TuK1, pp. 50-51.
- [5] D. Large, "Creating a Network for Interactivity," *IEEE Spectrum*, vol. 32, no. 4, pp. 58-63, Apr. 1995.
- [6] J. A. Chiddix, J. A. Vaughan, R. W. Wolfe, "The Use of Fiber Optics in Cable Communications Networks," *Journal of Lightwave Technology*, vol. 11, no. 1, pp. 154-166, Jan. 1993.
- [7] C. Basil, A. P. Cavallerano, M. S. Deiss, R. Keeler, J. S. Lim, W. C. Luplow, W. H. Paik, E. Petajan, R. Rast, G. Reitmeier, T. R. Smith, C. Todd, "The U.S. HDTV Standard: The Grand Alliance," *IEEE Spectrum*, vol. 32, no. 4, pp. 36-45, Apr. 1995.
- [8] K. J. Kerpez, "A Comparison of QAM and VSB for Hybrid Fiber/Coax Digital Transmission," *IEEE Transactions on Broadcasting*, vol. 41, no. 1, pp. 9-16, Mar. 1995.
- [9] K. M. Pham, Performance of 64-QAM Signals in a Hybrid AM-VSB/QAM Optical Fiber Transmission System, M.Sc. Thesis, University of Alberta, Spring 1994.
- [10] K. Maeda, H. Nakata, K. Fujito, "Analysis of BER of 16QAM Signal in AM/16QAM Hybrid Optical Transmission System," *Electronics Letters*, vol. 29, no. 7, pp. 640-642, Apr. 1993.
- [11] Q. Shi, "Performance Limits on M-QAM Transmission in Hybrid Multichannel AM/QAM Fiber Optic Systems," *IEEE Photonics Technology Letters*, vol. 5, no. 12, pp. 1452-1455, Dec. 1993.
- [12] K. M. Pham, J. Conradi, G. Cormack, B. Thomas, C. Anderson, "Performance of 64-QAM Signals in a Hybrid AM-VSB/QAM Optical Transmission System," *OFC '94 Technical Digest*, WH1, pp. 107-108.
- [13] X. Lu, G. E. Bodeep, T. E. Darcie, "Clipping-Induced Impulse Noise and Its Effect on Bit-Error Performance in AM-VSB/64QAM Hybrid Lightwave Systems," *IEEE Photonics Technology Letters*, vol. 6, no. 7, pp. 866-868, July 1994.

- [14] S. Ovadia, L. Eskildsen, J. T. Sciarabba, C. Lin, W. T. Anderson, "Bit-Error-Rate Impairment in Hybrid AM-VSB/16-QAM Multichannel Video Lightwave Transmission Systems," *IEEE Photonics Technology Letters*, vol. 6, no. 7, pp. 869-871, July 1994.
- [15] S. Ovadia, L. Eskildsen, C. Lin, W. T. Anderson, "Multiple Optical Reflections in Hybrid AM/16-QAM Multichannel Video Lightwave Transmission Systems," *IEEE Photonics Technology Letters*, vol. 6, no. 10, pp. 1261-1264, Oct. 1994.
- [16] G. R. Joyce, R. Olshansky, "The Clipping Penalty in Fiber-Based, Combined AM-VSB and Compressed-Digital-Video Transmission Systems," *IEEE Photonics Technology Letters*, vol. 6, no. 11, pp. 1368-1370, Nov. 1994.
- [17] X. Lu, G. E. Bodeep, T. E. Darcie, "Broad-Band AM-VSB/64 QAM Cable TV System over Hybrid Fiber/Coax Network," *IEEE Photonics Technology Letters*, vol. 7, no. 4, pp. 330-332, Apr. 1995.
- [18] S. Keller, H. Krimmel, G. Warne, R. Heidemann, "Hybrid Transmission of Analogue PAL and Digital 64-QAM CATV Channel," *Electronics Letters*, vol. 31, no. 11, pp. 904-905, May 1995.
- [19] Q. Shi, "Asymptotic Clipping Noise Distribution and Its Impact on M-ary QAM Transmission over Optical Fiber," *IEEE Transactions on Communications*, vol. 43, no. 6, pp. 2077-2084, June 1995.
- [20] A. Kanazawa, M. Shibutani, K. Emura, "Pre-Clipping Method to Reduce Clipping-Induced Degradation in Hybrid Analog/Digital Subcarrier-Multiplexed Optical Transmission Systems," *IEEE Photonics Technology Letters*, vol. 7, no. 9, pp. 1069-1071, Sept. 1995.
- [21] K. Pham, J. Conradi, G. Cormack, B. Thomas, C. Anderson, "Impact of Noise and Nonlinear Distortion Due to Clipping on the BER Performance of 64-QAM Signal in Hybrid AM-VSB/QAM Optical Fiber Transmission System," *Journal of Lightwave Technology*, vol. 13, no. 11, accepted for publication, Nov. 1995.
- [22] F. G. Stremler, *Introduction to Communication Systems*, 3 ed., Addison-Wesley, New York, pp. 714-718, 1990.
- [23] G. P. Agrawal, *Fiber-Optic Communication Systems*, John Wiley & Sons, New York, pp. 302-309, 1992.
- [24] L. W. Couch II, *Digital and Analog Communication Systems*, 4 ed., Macmillan, New York, pp. 318-321, 1993.
- [25] J. Lipson, L. C. Upadhyayula, S. Y. Huang, C. B. Roxlo, E. J. Flynn, P. M. Nitzsche, C. J. McGrath, G. L. Fenderson, M. S. Schaefer, "High-Fidelity Lightwave Transmission of Multiple AM-VSB NTSC Signals," *IEEE Transactions on Microwave Theory and Techniques*, vol. 38, no. 5, pp. 483-493, May 1990.
- [26] T. E. Darcie, G. E. Bodeep, "Lightwave Subcarrier CATV Transmission Systems," *IEEE Transactions on Microwave Theory and Techniques*, vol. 38, no. 5, pp. 524-533, May 1990.



- [27] G. Keiser, *Optical Fiber Communications*, 2 ed., McGraw-Hill, New York, pp. 357-369, 1991.
- [28] A. A. M. Saleh, "Fundamental Limit on Number of Channels in Subcarrier-Multiplexed Lightwave CATV System," *Electronics Letters*, vol. 25, no. 17, pp. 776-777, Jun. 1989.
- [29] D. J. G. Mestdagh, *Fundamentals of Multiaccess Optical Fiber Networks*, Artech House, Boston, pp. 295-317, 1995.
- [30] J. Stewart, *Calculus*, Brooks/Cole, Monterey, pp. 618-619, 1987.
- [31] National Cable Television Association, *NCTA Recommended Practices for Measurements on Cable Television Systems*, 2 ed., Nov. 1989.
- [32] H. Yonetani, I. Ushijima, T. Takada, K. Shima, "Transmission Characteristics of DFB Laser Modules for Analog Applications," *Journal of Lightwave Technology*, vol. 11, no. 1, pp. 147-153, Jan. 1993.
- [33] A. Takemoto, H. Watanabe, Y. Nakajima, Y. Sakakibara, S. Kakimoto, J. Yamashita, T. Hatta, Y. Miyake, "Distributed Feedback Laser Diode and Module for CATV Systems," *IEEE Journal on Selected Areas in Communications*, vol. 8, no. 7, pp. 1359-1364, Sept. 1990.
- [34] K. Petermann, *Laser Diode Modulation and Noise*, Kluwer Academic Publishers, Dordrecht, p. 34, 1988.
- [35] C. Y. Kuo, "Fundamental Nonlinear Distortions in Analog Links with Fiber Amplifiers," *Journal of Lightwave Technology*, vol. 11, no. 1, pp. 7-15, Jan. 1993.
- [36] K. Alameh, R. A. Minasian, "Optimum Optical Modulation Index of Laser Transmitters in SCM Systems," *Electronics Letters*, vol. 26, no. 16, pp. 1273-1275, Aug. 1990.
- [37] J. H. Angenent, "Simple Model for Calculation of Distortion in an Optical Analogue Subcarrier Multiplexed CATV System," *Electronics Letters*, vol. 26, no. 24, pp. 2049-2050, Nov. 1990.
- [38] K. Alameh, R. A. Minasian, "Ultimate Limits of Subcarrier Multiplexed Lightwave Transmission," *Electronics Letters*, vol. 27, no. 14, pp. 1260-1262, July 1991.
- [39] C. J. Chung, I. Jacobs, "Simulation of the Effects of Laser Clipping on the Performance of AM SCM Lightwave Systems," *IEEE Transactions Photonics Technology Letters*, vol. 3, no. 11, pp. 1034-1036, Nov. 1991.
- [40] M. R. Phillips, T. E. Darcie, "Numerical Simulation of Clipping-Induced Distortion in Analog Lightwave Systems", *IEEE Transactions Photonics Technology Letters*, vol. 3, no. 12, pp. 1153-1155, Dec. 1991.
- [41] C. J. Chung, I. Jacobs, "Practical TV Channel Capacity of Lightwave Multichannel AM SCM Systems Limited by the Threshold Nonlinearity of Laser Diodes," *IEEE Photonics Technology Letters*, vol. 4, no. 3, pp. 289-292, Mar. 1992.

- [42] N. J. Frigo, G. E. Bodeep, "Clipping Distortion in AM-VSB CATV Subcarrier Multiplexed Lightwave Systems," *IEEE Photonics Technology Letters*, vol. 4, no. 7, pp. 781-784, July 1992.
- [43] Q. Shi, R. S. Burroughs, D. Lewis, "An Alternative Model for Laser Clipping-Induced Nonlinear Distortion for Analog Lightwave CATV Systems," *IEEE Photonics Technology Letters*, vol. 4, no. 7, pp. 784-787, July 1992.
- [44] J. E. Mazo, "Asymptotic Distortion Spectrum of Clipped, DC-Biased, Gaussian Noise," *IEEE Transactions on Communications*, vol. 40, no. 8, pp. 1339-1344, Aug. 1992.
- [45] N. J. Frigo, M. R. Phillips, G. E. Bodeep, "Clipping Distortion in Lightwave CATV Systems: Models, Simulations, and Measurements," *Journal of Lightwave Technology*, vol. 11, no. 1, pp. 138-146, Jan. 1993.
- [46] N. J. Frigo, "A Model of Intermodulation Distortion in Non-Linear Multicarrier Systems," *IEEE Transactions on Communications*, vol. 42, no. 2/3/4, pp. 1216-1222, Feb./Mar./Apr. 1994.
- [47] W. Muys, M. F. R. Mortier, "Numerical Simulation of Clipping Induced Distortion in Externally Modulated Lightwave AM-SCM Systems," *IEEE Photonics Technology Letters*, vol. 6, no. 6, pp. 747-749, June 1994.
- [48] A. J. Rainal, "Laser Intensity Modulation as a Clipped Gaussian Process," *IEEE Transactions on Communications*, vol. 43, no. 2/3/4, pp. 490-494, Feb./Mar./Apr. 1995.
- [49] A. J. Rainal, "Distortion Spectrum of Laser Intensity Modulation," *IEEE Transactions on Communications*, vol. 43, no. 2/3/4, pp. 1644-1652, Feb./Mar./Apr. 1995.
- [50] J. G. Proakis, *Digital Communications*, 2 ed., McGraw-Hill, New York, Chapters 1 and 4, 1989.
- [51] S. O. Rice, "Distribution of the Duration of Fades in Radio Transmission," *Bell System Technical Journal*, vol. 37, pp. 581-635, May 1958.
- [52] S. S. Soliman, M. D. Srinath, *Continuous and Discrete Signals and Systems*, Prentice-Hall, Englewood Cliffs, pp. 52, 177, 209-216, 1990.
- [53] S. O. Rice, "Mathematical Analysis of Random Noise," *Bell System Technical Journal*, vol. 23, pp. 282-332, July 1944.
- [54] J. B. Thomas, *An Introduction to Communication Theory and Systems*, Springer-Verlag, New York, pp. 123-140, 1988.
- [55] D. Middleton, *An Introduction to Statistical Communication Theory*, McGraw-Hill, New York, p. 494, 1960.
- [56] R. E. Ziemer, "Error Probabilities Due to Additive Combinations of Gaussian and Impulsive Noise," *IEEE Transactions on Communication Technology*, vol. COM-15, pp. 471-474, June 1967.

- [57] Matrix Test Equipment Inc., *Models ASX-16, AR-12, and DTS Operating Manual*, [Unknown].
- [58] Fujitsu Limited, *FLD150F3ACH-AL Data Sheet*, 1992.
- [59] Ipitex Inc., *FiberTrunk 600 Data Sheet*, 1990.
- [60] E. Eichen, J. Schlafer, W. Rideout, J. McCabe, "Wide-Bandwidth Receiver/Photodetector Frequency Response Measurements Using Amplified Spontaneous Emission from a Semiconductor Optical Amplifier," *Journal of Lightwave Technology*, vol. 8, no. 6, pp. 912-916, June 1990.
- [61] A. O. Allen, *Probability, Statistics, and Queueing Theory*, Academic Press, New York, pp. 119-120, 1978.
- [62] D. Middleton, "Statistical-Physical Models of Electromagnetic Interference," *IEEE Transactions on Electromagnetic Compatibility*, vol. 19, no. 3, pp. 106-127, Aug. 1977.
- [63] I. Switzer, "A Harmonically Related Carrier System for Cable Television," *IEEE Transactions on Communications*, vol. COM-23, pp. 155-166, Jan. 1975

# Appendix A: CATV Channel Frequencies

NCTA Channel Designation	Channel Allocation (MHz)	Video Carrier Frequency (MHz)	Harmonically Related Carrier Frequency (MHz)
2	54-60	55.25	54
3	60-66	61.25	60
4	66-72	67.25	66
5	76-82	77.25	78
6	82-88	83.25	84
14	120-126	121.25	120
15	126-132	127.25	126
16	132-138	133.25	132
17	138-144	139.25	138
18	144-150	145.25	144
19	150-156	151.25	150
20	156-162	157.25	156
21	162-168	163.25	162
22	168-174	169.25	168
7	174-180	175.25	174
8	180-186	181.25	180
9	186-192	187.25	186
10	192-198	193.25	192
11	198-204	199.25	198
12	204-210	205.25	204
13	210-216	211.25	210
23	216-222	217.25	216
24	222-228	223.25	222
25	228-234	229.25	228
26	234-240	235.25	234
27	240-246	241.25	240
28	246-252	247.25	246
29	252-258	253.25	252
30	258-264	259.25	258
31	264-270	265.25	264

32	270-276	271.25	270
33	276-282	277.25	276
34	282-288	283.25	282
35	288-294	289.25	288
36	294-300	295.25	294
37	300-306	301.25	300
38	306-312	307.25	306
39	312-318	313.25	312
40	318-324	319.25	318
41	324-330	325.25	324
42	330-336	331.25	330
43	336-342	337.25	336

## Appendix B: Modeling the Parabolic Pulses as Impulses

We consider the frequency spectrum of a parabolic pulse as it passes through a BPF with the following transfer function:

$$H_{BPF}(\omega) = \begin{cases} 1 & , |\omega - \omega_c| \leq \Delta\omega_{BW}/2 \\ 0 & , |\omega - \omega_c| > \Delta\omega_{BW}/2 \end{cases} \quad (B.1)$$

If  $P_{in}(\omega)$  is the Fourier Transform of the input parabolic pulse, then the output transient response of the BPF is

$$\begin{aligned} P_{out}(t) &= F^{-1}[P_{in}(\omega)H_{BPF}(\omega)] = \frac{1}{2\pi} \int_{-\infty}^{\infty} P_{in}(\omega)H_{BPF}(\omega)e^{j\omega t} d\omega \\ &= \frac{1}{2\pi} \int_{-\omega_c - \frac{\Delta\omega_{BW}}{2}}^{-\omega_c + \frac{\Delta\omega_{BW}}{2}} P_{in}(\omega)H_{BPF}(\omega)e^{j\omega t} d\omega + \frac{1}{2\pi} \int_{\omega_c - \frac{\Delta\omega_{BW}}{2}}^{\omega_c + \frac{\Delta\omega_{BW}}{2}} P_{in}(\omega)H_{BPF}(\omega)e^{j\omega t} d\omega \end{aligned} \quad (B.2)$$

A narrowband approximation can be made if it is assumed  $P_{in}(\omega)$  is relatively flat across the passband of  $H_{BPF}(\omega)$ . Justification for this assumption can be found by inspecting the expected value of the clipping time duration  $\tau_p$  and considering the duration-bandwidth relationship of the Fourier Transform. From Figure 3.7, it is observed that the average duration of the parabolic pulses is in the picosecond range. It is well known that the duration of a time-limited pulse is inversely related to the frequency span of its Fourier Transform [52]. We can compare the picosecond time duration of the pulses to the reciprocal of the BPF bandwidth ( $1/\Delta f_{BW} = 1/6\text{MHz} = 167\text{ns}$ ) where the BPF represents a 6 MHz CATV channel. Because  $\tau_p$  is much smaller than  $1/\Delta f_{BW}$ , the bandwidth of the parabolic input pulses will be much larger than the filter bandwidth, and  $P_{in}(\omega)$  can be assumed not to vary significantly in the filter passband. Using the narrowband

approximation, the BPF output response to the parabolic pulses becomes

$$\begin{aligned}
 p_{out}(t) &\approx \frac{P_{in}(-\omega_c)}{2\pi} \int_{-\omega_c - \frac{\Delta\omega_{BW}}{2}}^{-\omega_c + \frac{\Delta\omega_{BW}}{2}} H(\omega) e^{j\omega t} d\omega + \frac{P_{in}(\omega_c)}{2\pi} \int_{\omega_c - \frac{\Delta\omega_{BW}}{2}}^{\omega_c + \frac{\Delta\omega_{BW}}{2}} H(\omega) e^{j\omega t} d\omega \\
 &\approx P_{in}(\omega_c) F^{-1}[H(\omega)] = P_{in}(\omega_c) \cdot h_{BPF}(t)
 \end{aligned} \quad (B.3)$$

where  $h_{BPF}(t)$  is the impulse response of the BPF. Because  $p_{in}(t)$  is a real-valued time signal,  $P_{in}(\omega)$  is even symmetric about  $\omega = 0$  such that  $P_{in}(\omega) = P_{in}(-\omega)$  in equation (B.3). Because the output response in (B.3) is a weighted impulse response, it is apparent that the use of the narrowband approximation implies that the input parabolic pulse can be treated as an impulse function.

## Appendix C: Deriving the Area Probability Density of the Parabolic Pulses

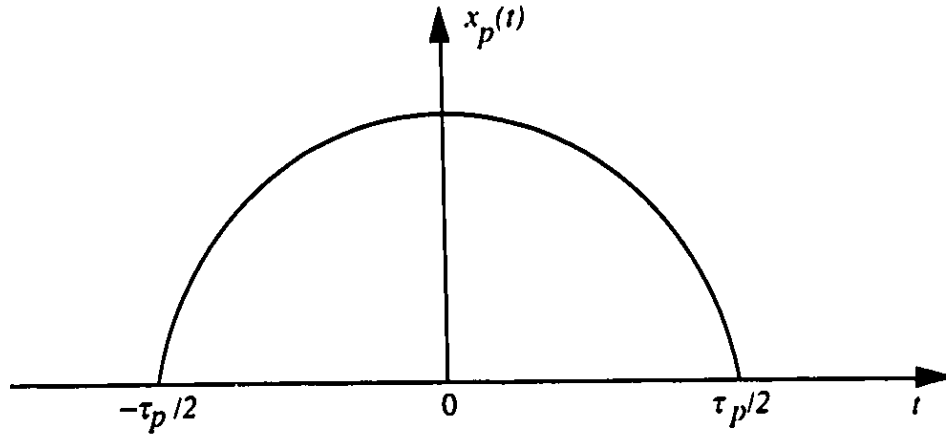


Figure C.1: Parabolic Pulse

A parabolic pulse can be defined by the function  $x_p(t)$ :

$$x_p(t) = \begin{cases} c_1 \left( -t^2 + \frac{\tau_p^2}{4} \right) & , |t| < \tau_p/2 \\ 0 & , \text{elsewhere} \end{cases} \quad (\text{C.1})$$

The area  $A$  of the parabolic pulse is obtained by integrating  $x_p(t)$  with respect to time:

$$A = \text{parabola area} = \int_{-\infty}^{\infty} x_p(t) dt = \frac{c_1}{6} \tau_p^3 = c_2 \tau_p^3 \quad (\text{C.2})$$

where  $c_2 = c_1/6$ .

If  $\tau_p$  has a probability density function given by  $p(\tau_p)$  in equation (3.14), then the



cumulative distribution function of  $A$  is [50]

$$\begin{aligned} CDF_A(A) &= p_A(c_2 \tau_p^j \leq A) = p_{\tau_p} \left( \tau_p \leq \left( \frac{A}{c_2} \right)^{1/j} \right) \\ &= \int_{-\infty}^{\left( \frac{A}{c_2} \right)^{1/j}} p_{\tau_p}(\tau_p) d\tau_p = CDF_{\tau_p} \left( \left( \frac{A}{c_2} \right)^{1/j} \right) \end{aligned} \quad (C.3)$$

where  $CDF_A$  and  $CDF_{\tau_p}$  are the cumulative distribution functions of  $A$  and  $\tau_p$ , respectively. Substituting equation (3.14) into the integral expression in (C.3), the probability density function of  $A$  is given by

$$p(A) = \frac{d}{dA}(CDF_A(A)) = \frac{1}{3c_2(A/c_2)^{2/j}} \frac{\pi (A/c_2)^{1/j}}{2 \frac{1}{\tau_p^2}} \exp \left[ -\frac{\pi}{4} \frac{1}{\tau_p^2} \left[ \frac{A}{c_2} \right]^{2/j} \right] \quad (C.4)$$

for  $A > 0$ .

The expression for  $p(A)$  can be generalized to the form of

$$p(A) = \frac{c_3}{A^{1/j}} \exp[-cA^{2/j}] \quad (C.5)$$

When the expression for  $p(A)$  in equation (C.5) is normalized to have unity area, we find that

$$c_3 = \frac{2}{3} c \quad (C.6)$$

Substituting (C.6) into (C.5), we get

$$p(A) = \frac{2}{3} \frac{c}{A^{1/j}} \exp[-cA^{2/j}] \quad (C.7)$$

The mean square value of  $A$  is given by

$$\overline{A^2} = \int_0^{\infty} \frac{2c}{3} \frac{A^2}{A^{1/3}} \exp[-cA^{2/3}] dA = \frac{6}{c^3} \quad (\text{C.8})$$

and therefore

$$c = \left( \frac{6}{\overline{A^2}} \right)^{1/3} \quad (\text{C.9})$$

## Appendix D: Approximating the Probability Density of Excursion Amplitudes with Threshold Crossing Rate Data

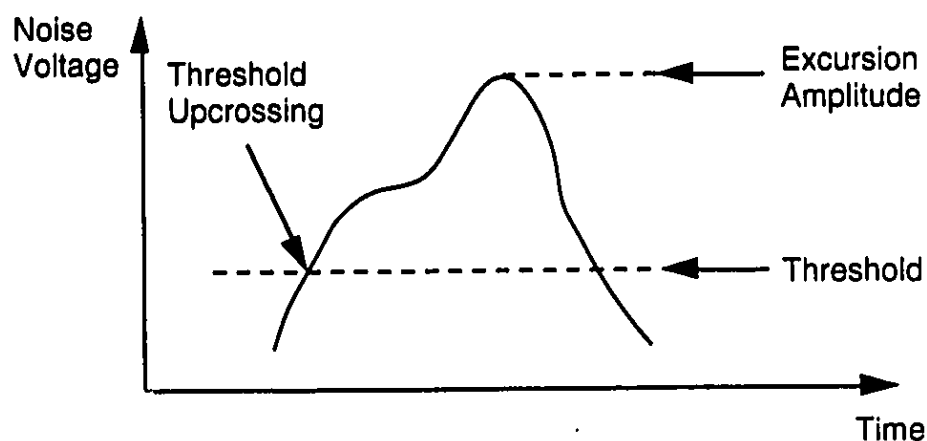


**Figure D.1: Definition of Excursion Amplitude**

The excursion amplitude is defined as the maximum voltage that the noise signal reaches between a threshold upcrossing and subsequent downcrossing as shown in Figure D.1. In deriving an approximation for the amplitude probability density, it is assumed that all excursions start at a voltage of zero, rise monotonically to a maximum voltage, and then decrease monotonically back to zero. Under this assumption, there is a one-to-one correspondence between a threshold upcrossing and an excursion. Of course, the excursions in the experimental noise waveform will not follow the assumption of monotonic behavior strictly. This is due many factors such as the oscillatory nature of the filter impulse response, the effect of additive Gaussian noise, and the superposition of multiple impulse responses. As a result, the correspondence between an upcrossing and an excursion will not always be one-to-one as illustrated by Figure D.2. In the figure, it is shown that, because the excursion does not monotonically increase to its maximum, increasing the threshold value results in a single excursion causing two threshold crossing

events. Consequently, the single excursion event is detected as two separate excursion events with two separate excursion amplitudes. This source of error should be kept in mind when considering the results obtained with the method described in this section.

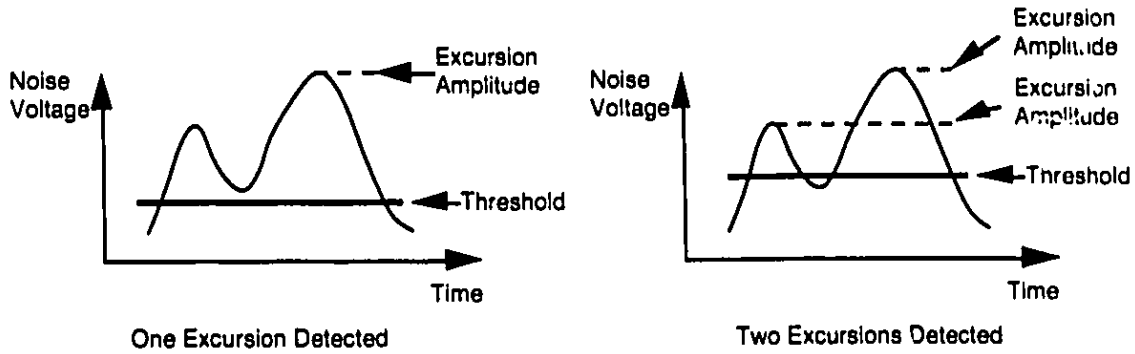


**Figure D.2: One Excursion Being Detected as Two Excursions**

The process of deriving the excursion amplitude probability density from the upcrossing rate data is illustrated in Figure D.3. In the first diagram (a), the threshold upcrossing rate (as a function of threshold voltage) is represented by the function  $f_{cross}(V_{th})$ . By subtracting  $f_{cross}(V_{th})$  from a constant function having the value of  $f_{cross}(V_{th})$  at  $V_{th} = 0$ , a new function  $f_{not-cross}(V_{th})$ , which represents the rate of excursions having amplitudes smaller than  $V_{th}$  can be obtained as shown in (b). By normalizing  $f_{not-cross}(V_{th})$  to have a value of one at  $V_{th} = infinity$ , we can obtain an approximation for the cumulative distribution of the excursion amplitude as shown by  $CDF_{amp}(V_{th})$  in (c). Finally, a representation (d) of the excursion amplitude probability density  $p_{amp}(V_{th})$  can be calculated by taking the derivative of  $CDF_{amp}(V_{th})$ .

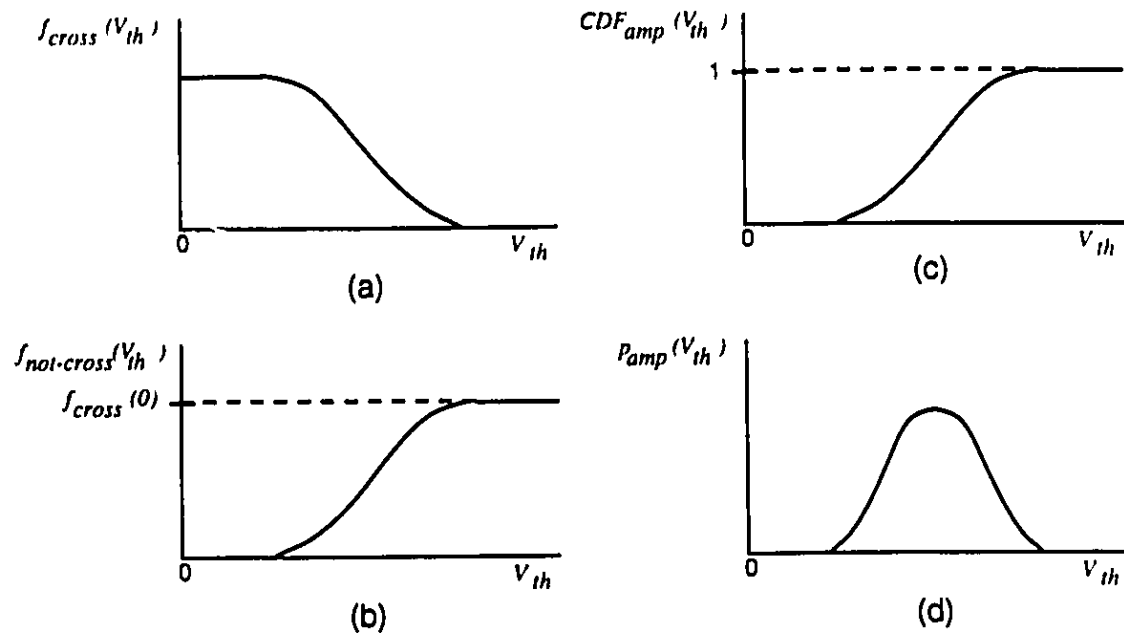


**Figure D.3: Deriving Excursion Amplitude Probability Density from Crossing Rate Data**

## Appendix E: Explanation for the Dominant 167 ns and 1.5 $\mu$ s Time Interval Between Clipping Events

The cause for the dominant 167 ns and 1.5  $\mu$ s time intervals between consecutive clipping events is rooted in the 6 MHz spacing between carriers in the NTSC frequency plan. The explanation for these frequently-occurring intervals is more easily understood using the concept of Harmonically Related Carriers.

### E.1 Harmonically Related Carriers

A Harmonically Related Carrier (HRC) system designates a plan of carrier frequencies in which the video carriers are generated by a master 6 MHz oscillator [63]. The frequency of the different HRC carriers are multiples of the 6 MHz reference frequency. For example, the carrier frequencies can be defined as

$$f_n = (n + 7) \cdot 6\text{MHz}, \quad n = 2, 3, \dots, N. \quad (\text{E.1})$$

where  $f_n$  is the carrier frequency of the  $n^{\text{th}}$  channel and  $N$  is the highest channel number. The corresponding harmonically related carrier for each NTSC channel is given in the table in Appendix A.

### E.2 The Dominant 167 ns Time Interval

The 167 ns time interval between clips is related to the 6 MHz spacing between carrier frequencies. If we consider an HRC system (Channel 2 = 54 MHz, Channel 3 = 60 MHz, Channel 4 = 66 MHz, etc.), we can see that each carrier frequency in the HRC system is evenly divisible by 6 MHz. This means that each carrier will undergo an integer number of periods in the span of  $1/6\text{MHz} = 167\text{ns}$ . Thus we can see that, in a subcarrier multiplexed HRC system, if the sum of all the carriers at a specific point in time results in a

large excursion in the SCM signal, this same excursion will occur again 167 ns later (i.e. the SCM signal is a 6 MHz periodic signal). This concept is graphically illustrated in Figure E.1 where Channels X, Y, and Z are all in-phase only at the beginning and end of the 167 ns interval. If the carriers Figure E.1 are summed to form an SCM signal, we can see that the SCM signal will only reach its maximum amplitude at the beginning and end of the 167 ns period. In fact, the time occurrences of the largest excursion, second-largest excursion, third-largest excursion, and etc. are all periodic with a frequency of 6 MHz. Thus if we set a threshold between the amplitudes of the largest and second-largest excursion, the time interval between threshold upcrossings will always be 167 ns. This will not be the case if the threshold is set below the second-largest excursion because the first-largest and second-largest excursions will both cause threshold upcrossings. This leads to the question: How does this relate to the 167 ns interval observed in the results of Chapter 5?

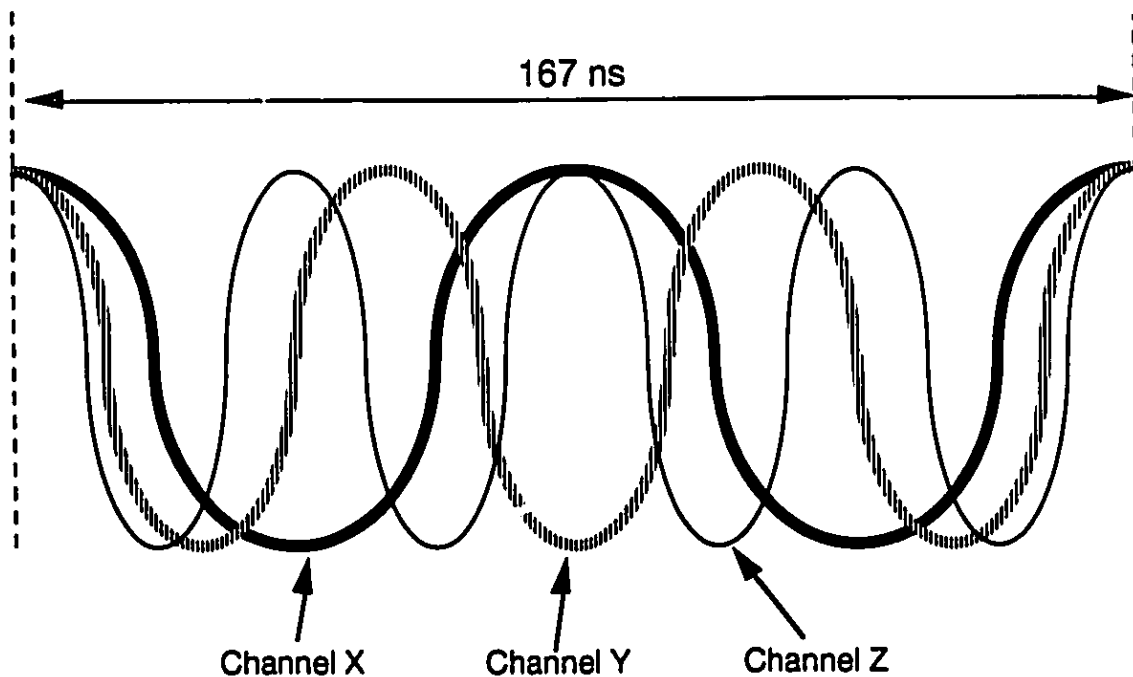


**Figure E.1: Periodic Carriers in Harmonically Related Carrier System**

The experimental results of Chapter 5 were obtained using carriers following the NTSC frequency plan. Because the NTSC carriers are not harmonically related, the unmodulated SCM signal is not periodic at 6 MHz. However, the majority of carriers are spaced 6 MHz apart, and their frequencies (except for Channels 5 and 6) are obtained by simply adding 1.25 MHz to the harmonically related equivalents. We can compare the period of the NTSC channel carrier and its harmonic equivalent as shown below. For Channel 2 the period of the HRC and NTSC carriers are, respectively,

$$t_{HRC} = \frac{1}{54\text{MHz}} = 18.52\text{ns} \quad t_{NTSC} = \frac{1}{55.25\text{MHz}} = 18.10\text{ns} \quad (\text{E.2})$$

and for Channel 43:

$$t_{HRC} = \frac{1}{336\text{MHz}} = 2.976\text{ns} \quad t_{NTSC} = \frac{1}{337.25\text{MHz}} = 2.965\text{ns} \quad (\text{E.3})$$

From equations (E.2) and (E.3), we can see that the difference in period between the NTSC carriers and their HRC equivalents is not that great. The magnitude (0.42 ns) of the difference between  $t_{HRC}$  and  $t_{NTSC}$  for Channel 2 is comparatively small to both the period of the carriers and the 167 ns period of the HRC SCM signal, and this difference is even smaller for higher frequency channels. Based on this observation, it is suggested that even though the NTSC SCM signal is not strictly periodic at 6 MHz, large excursions have a high probability of occurring about 167 ns (or close to 167 ns) apart. The fact that the carriers of an NTSC system come close to but do not exactly undergo an integer number of periods in the span of 167 ns means that the occurrence of a threshold crossing does not necessarily guarantee another threshold crossing 167 ns later. This uncertainty explains the presence of longer dominant time intervals such as 1.5  $\mu\text{s}$  and 4  $\mu\text{s}$ . However, as indicated



by the experimental results in Chapter 5, the time interval between consecutive clipping events in an NTSC system has a high probability of being 167 ns.

### E.3 The Dominant 1.5 $\mu$ s Time Interval

The dominant 1.5  $\mu$ s interval is caused by the two “oddball” carrier frequencies of Channels 5 and 6 in the NTSC frequency plan. All the NTSC carrier frequencies in Appendix A can be derived by adding 1.25 MHz to their harmonic equivalents except for the carriers of Channels 5 and 6 which are 0.75 MHz below their harmonic equivalents. Thus, Channels 5 and 6 do not contribute to the 6 MHz channel spacing argument that was used to explain the dominant 167 ns interval in the previous section. We can investigate the effect of the “oddball” frequencies in an HRC system by subtracting all of the NTSC carrier frequencies, including Channels 5 and 6, by 1.25 MHz. The resulting carrier frequencies for Channels 5 and 6 are 76 MHz and 82 MHz, respectively. We can see how they cause the dominant 1.5  $\mu$ s interval by dividing 1.5  $\mu$ s by 1) the period of the 76 MHz Channel 5 carrier; 2) the period of the 82 MHz Channel 6 carrier; and 3) 167 ns. Dividing 1.5  $\mu$ s by the period of the Channel 5 carrier, we get

$$\frac{1.5 \mu s}{1/76 MHz} = 114 \quad (E.4)$$

Dividing 1.5  $\mu$ s by the period of the Channel 6 carrier, we get

$$\frac{1.5 \mu s}{1/82 MHz} = 123 \quad (E.5)$$

and, dividing 1.5  $\mu$ s by 167 ns, we get

$$\frac{1.5 \mu s}{1/6 MHz} = 9 \quad (E.6)$$

It is observed that in (E.4) and (E.5) the division of  $1.5 \mu\text{s}$  by the carrier periods result in integer numbers which means that the Channel 5 and Channel 6 carriers undergo an integer number of cycles in  $1.5 \mu\text{s}$ . In equation (E.6), it is shown that a composite signal containing all the channel carriers except Channels 5 and 6 also undergoes an integer number of periods in  $1.5 \mu\text{s}$ . (Note that all the carrier frequencies in this composite signal are evenly divisible by 6 MHz, hence it is periodic at 6 MHz.) Thus we can argue that an unmodulated subcarrier multiplexed HRC signal containing the 76 MHz carrier of Channel 5, the 82 MHz carrier of Channel 6, and the remaining "non-oddball" channel carriers is periodic with a period of  $1.5 \mu\text{s}$ . This explains the fact that if a large excursion occurs in this signal, another one will occur  $1.5 \mu\text{s}$  later. Of course, to obtain the original NTSC carrier frequencies, we must add 1.25 MHz to the carrier frequencies in the analysis above. However, as discussed in the previous section, this adjustment does not significantly change the argument of periodicity and simply adds a degree of randomness to the expected  $1.5 \mu\text{s}$  interval between clips.

## Appendix F: Computer Program Listings

### F.1 CNR vs. Received Optical Power (Mathematica)

```
(*****)
(* noise.m *)
(* ----- *)
(*
(* This program calculates the Carrier-to-Noise Ratio (CNR) in an optical *)
(* SCM system. The noise contributions include shot noise, thermal noise, *)
(* and RIN noise. The total CNR and CNR with respect to each noise source *)
(* is tabulated as a function of received optical power in a tab-separated *)
(* data file called "CNR.Data". *)
(* *)
(*****)

(* dB conversion functions *)

dBtoRatio[x_] := 10^(x/10);
ratioToDB[x_] := 10 Log[10, x];

(* Received signal and noise parameters *)

m = 0.0288; (* Modulation index per channel *)
Resp = 1.05; (* Responsivity in A/W *)
q = 1.602 10^-19; (* Electron charge *)
RINdB = -160; (* RIN noise in dB/Hz *)
RIN = dBtoRatio[RINdB]; (* RIN noise *)
B = 4 10^6; (* Channel bandwidth in Hz *)
ith = 6 10^-12; (* Thermal noise in pA/Sqrt[Hz] *)
Pr[PrdBm_] := dBtoRatio[PrdBm]*0.001; (* Received optical power in Watts *)

(* Calculate signal power *)

signal[PrdBm_] := N[0.5 (m Resp Pr[PrdBm])^2];

(* Calculate different noise terms *)

noiseShot[PrdBm_] := N[2 q Resp Pr[PrdBm] B];
noiseRIN[PrdBm_] := N[RIN Resp^2 Pr[PrdBm]^2 B];
noiseTherm := N[ith^2 B];
noiseTot[PrdBm_] := noiseRIN[PrdBm] + noiseShot[PrdBm] + noiseTherm;

(* Calculate CNR's *)

CNRShot[PrdBm_] := N[signal[PrdBm]/noiseShot[PrdBm]];
CNRIN[PrdBm_] := N[signal[PrdBm]/noiseRIN[PrdBm]];
CNRTherm[PrdBm_] := N[signal[PrdBm]/noiseTherm];
CNRTot[PrdBm_] := N[signal[PrdBm]/noiseTot[PrdBm]];

CNRShotdB[PrdBm_] := N[ratioToDB[CNRShot[PrdBm]]];
CNRINDB[PrdBm_] := N[ratioToDB[CNRIN[PrdBm]]];
CNRThermdB[PrdBm_] := N[ratioToDB[CNRTherm[PrdBm]]];
CNRTotdB[PrdBm_] := N[ratioToDB[CNRTot[PrdBm]]];
```

```

(* Main Loop *)

outfile = OpenWrite["CNR.Data"];
For [power=10, power >= -30, power=power - 1,
    WriteString[outfile, power, "\t", CForm[CNRShotdB[power]], "\t",
    CForm[CNRIRIndB[power]], "\t",
    CForm[CNRThermdB[power]], "\t", CForm[CNRTotdB[power]], "\n"];
];
Close["CNR.Data"];

```

## F.2 Program for Calculating Experimental Noise Amplitude Probability Density (C Programming Language)

```

#include <stdio.h>
#include <stdlib.h>
#include <string.h>

#define NORMALIZE 1 /* output normalized data or raw data */
#define NUMBUCKET 256 /* number of histogram categories */

/*****
/* This programs reads in the ascii data file generated by the
/* HP54120 Oscilloscope Histogram Labview program and outputs a
/* normalized PDF derived from the histogram data. The output file
/* is a tab-seperated file with the voltage column on the left and the
/* PDF column on the right. The normalization is achieved by finding
/* the area of the histogram using Trapezoidal Rule and multiplying
/* the histogram counts by the inverse of the area.
/*
/* The arguments to this program are:
/*
/* <execname> datafile
/*
*****/

main(int argc, char *argv[])
{
    char outfilename[50], bufferString1[500], bufferString2[100], bufferString3[100];
    char junkString[100];
    float offset, range, normalizedData[NUMBUCKET];
    float sum, area, bucketWidth, xval;
    int i, rawData[NUMBUCKET];
    FILE *infile, *outfile;
    int temp;

    if (argc != 2)
    {
        printf("Wrong number of arguments!\n");
        exit(0);
    }

    infile = fopen(argv[1], "r");

    strcpy(outfilename, argv[1]);
    strcat(outfilename, ".dat");
    outfile = fopen(outfilename, "w");

```

```

/* Line #1 is just file comments */
fgets(bufferString1, 500, infile);

/* Line #2 has the number of samples */
fgets(bufferString1, 500, infile);

/* Line #3 has the time window */
fgets(bufferString1, 500, infile);

/* Line #4 has the voltage offset */
fgets(bufferString1, 500, infile);
sscanf(bufferString1, "%s %s", bufferString2, bufferString3);
offset = atof(bufferString3);

/* extra line */
fgets(bufferString1, 500, infile);

/* Line #5 has the probe attenuation */
fgets(bufferString1, 500, infile);

/* extra line */
fgets(bufferString1, 500, infile);

/* Line #6 has the voltage range */
fgets(bufferString1, 500, infile);
sscanf(bufferString1, "%s %s", bufferString2, bufferString3);
range = atof(bufferString3);

/* extra line */
fgets(bufferString1, 500, infile);

/* Read in Histogram data */
for (i=0; i < NUMBUCKET; i++)
{
    fscanf(infile, "%d %c", &rawData[i], bufferString2);
}

/* Use Trapezoidal Rule to find area of Histogram */

bucketWidth = range/NUMBUCKET;
sum = rawData[0];
for (i=1; i < (NUMBUCKET - 1); i++)
{
    sum = sum + 2.0*rawData[i];
}
sum = sum + rawData[NUMBUCKET];
area = bucketWidth*(sum/2.0);

/* Normalization Routine */
for (i=0; i < NUMBUCKET; i++)
{
    normalizedData[i] = (1/area)*rawData[i];
}

/* Output Formatted Data Routine */

```

```

for (i=0; i < NUMBUCKET; i++)
{
    xval = offset - range/2 + i*bucketWidth;
    printf("%f\t%d\t%e\n", xval, rawData[i], normalizedData[i]);
    fprintf(outfile, "%f\t", xval);
    if (NORMALIZE)
        fprintf(outfile, "%e\n", normalizedData[i]);
    else
        fprintf(outfile, "%d\n", rawData[i]);
}

fclose(infile);
fclose(outfile);
}

```

### F.3 Program for Calculating the Experimental Probability Density of Excursion Amplitudes (Matlab)

```

% genImpulseAmpPDF.m
% -----
%
% This program generates the probability density of excursion amplitudes
% based on the threshold upcrossing rate data.
%
% Load in upcrossing rate data
load CrossRateModIndex6.dat;
inputArray = CrossRateModIndex6;
arraySize = size(inputArray,1);

% Separate the data into vectors containing threshold values and
% corresponding rates
threshold = inputArray(1:arraySize,1);
rate      = inputArray(1:arraySize,2);
threshold = flipud (threshold);
rate      = flipud (rate);

% Generate excursion amplitude probability density
tempVector = rate(1)*ones(arraySize,1) - rate; % generate cumulative distrbn
pdf = diff(tempVector) ./ diff(threshold); % generate prob distrbn from
cumulative
threshold = (threshold(1:(arraySize-1)) + threshold(2:arraySize))/2; % adjust
threshold axis

% Normalize the probability density to have an area of one
integral = trapz(threshold,pdf);
pdf = pdf/integral;

% Plot
semilogy(threshold,pdf);

% Write to output file
outfile = fopen('impulseAmpPDFModIndex6.dat','w');
for i=1:(arraySize-1)
    fprintf(outfile, '%d\t%e\n', threshold(i), pdf(i));
end
fclose(outfile);

```

## F.4 Theoretical Probability Density of Area of Impulses in Error Process (Matlab)

```
% theoryImpulseAmpPDF.m
% -----
%
% This program calculates the probability density of the area of
% the impulses in the error process based on Mazo's theory.
%

% Set constant c2 and generate xaxis
c2 = 9*10^26;
xVector = (0:0.1:3);

% Calculate probability densities for 0.05 and 0.06
% mod index per channel
AMmodIndex = 0.05; % mod index per channel
NN = 42; % number of channels
mu=sqrt((NN*AMmodIndex^2)/2); % rms mod index
rho = 1/(2*mu^2);
fb = 337.25*10^6; % highest frequency AM channel
fa = 55.25*10^6; % lowest frequency AM channel
rate = ((fb^3 - fa^3)/(3*(fb - fa)))^0.5 * exp(-rho); % clip rate
Tave = erfc(sqrt(rho))/(2*rate); % average clip duration
pdf1 = areapdf(xVector,c2,Tave); % generate prob density

AMmodIndex = 0.062; % mod index per channel
NN = 42; % number of channels
mu=sqrt((NN*AMmodIndex^2)/2); % rms mod index
rho = 1/(2*mu^2);
fb = 337.25*10^6; % highest frequency AM channel
fa = 55.25*10^6; % lowest frequency AM channel
rate = ((fb^3 - fa^3)/(3*(fb - fa)))^0.5 * exp(-rho); % clip rate
Tave = erfc(sqrt(rho))/(2*rate); % average clip duration
pdf2 = areapdf(xVector,c2,Tave); % generate prob density

pdf = [pdf1' pdf2'];

% Plot
semilogy(xVector,pdf);

% Write data to a files
outfile1 = fopen('theoryImpulseAmpPDFMI5.dat','w');
for i=1:length(pdf1)
    fprintf(outfile1, '%e\t%d\n', xVector(i), pdf1(i));
end
fclose(outfile1);

outfile2 = fopen('theoryImpulseAmpPDFMI6.dat','w');
for i=1:length(pdf2)
    fprintf(outfile2, '%e\t%d\n', xVector(i), pdf2(i));
end
fclose(outfile2);

function z = areapdf(x,c,tbar)
% Impulse Area PDF
% Impulse Area PDF
% Calculates the value of the PDF at the locations in x. The PDF
```

% is based on Mazo's theory of parabolic clips with time duration  
 % following a Rayleigh distribution.

```
z = ( pi ./ (6*c^(2/3)*x.^(1/3)*tbar^2) ) .* exp(-pi * (x/c).^(2/3)/(4*tbar^2));
```

## F.5 Theoretical Probability Density of Down-Converted Impulsive Noise (Mathematica)

```
(*****)
(* shotRectApprox.m *)
(* ----- *)
(*
(* This program determines the probability density of down-converted
(* Gaussian + clipping-induced impulsive noise. The baseband filter
(* impulse response is approximated with a rectangular pulse having a
(* duration of 1/(channel bandwidth).
(*
(*
(*****)

(* dB Conversion functions *)

dBtoRatio[x_] := 10^(x/10);
ratioToDB[x_] := 10 Log[10, x];

(* Set system parameters *)

NN = 42; (* Number of channels *)
AMmodIndex = 0.062; (* Mod index per channel *)
mu = N[Sqrt[(NN AMmodIndex^2)/2]]; (* Total rms modulation index *)
fb = 337.25 10^6; (* Highest frequency AM channel *)
fa = 55.25 10^6; (* Lowest frequency AM channel *)

(* Calculate Mazo's theoretical rate of clipping *)

rate = ((fb^3 - fa^3)/(3(fb - fa)))^0.5 Exp[-1/(2 mu^2)];

(* Set the channel bandwidth and determine its inverse *)

fc = 15 10^6; (* channel bandwidth in Hz *)
Tc = N[1/fc];

(* Set the impulsive noise power, Gaussian noise power, and calculate the clipping
index *)

varI = N[(0.007671)^2]; (* variance of impulsive noise in V^2 *)
varG = N[(0.0037876)^2]; (* variance of Gaussian noise in V^2 *)
varTot = N[varI + varG]; (* variance of total noise in V^2 *)
clippingIndex = N[Tc rate];
Print["varI: ", varI, " varG: ", varG, " clippingIndex: ", clippingIndex, " rate: ",
rate];
Print[" "];
```



```

(* ***** *)
(* Deriving the PDF *)
(* ----- *)
(*
(* This routine determines the pdf of shot noise combined with Gaussian
(* noise by sampling the characteristic function and taking the Inverse
(* Fast Fourier Transform (IFFT).
(*
(* Variables:
(*
(* n - number of points to use in the IFFT
(* maxV - maximum value of v for sampling the characteristic function M(jv)
(* sampledM - the list of M(jv) sample points to be IFFT'd; the first half
(* of the list is made by sampling M(jv) from v=0 to v=maxV, the
(* second half is made by imposing the condition that the real
(* part of the total list must be symmetric and the imaginary
(* part of the total list must be anti-symmetric (for a real pdf)
(* deltaV - interval size of the M(jv) samples
(* deltaI - the corresponding interval size of the pdf samples obtained
(* from the IFFT
(*
(* ***** *)

pulseEnergy = 1.0*Tc;
meanSquareA = N[(2*varI)/(rate*pulseEnergy)];
c3 = N[(6/meanSquareA)^(1/3)];
integral[v_] := Which[v == 0, 1, True,
(2*c3^(3/2)*E^((2*c3^3)/(27*v^2))*(3/Pi)^(1/2)*(v^(-2))^(1/2)*
BesselK[1/6, (2*c3^3)/(27*v^2)])/9];

(* Parameters for sampling the characteristic function *)

n = 2^11;
maxV = 2 10^3;
deltaV = maxV/(n/2);
deltaI = (2 Pi)/(n deltaV);
Print["n = ",n , " deltaV = ",N[deltaV], " maxV = ",maxV ];
Print[" "];
Print[" "];

(* Sample the characteristic function *)

sampledM = {};
sampledMG = {};
vAxis = {};
pdfAxis = {};
For [i=0, i <= n/2, i++,
v = i*deltaV;
theIntegral = integral[v];
sampledM = Append[sampledM, N[Exp[-(v^2 varG)/2] (1 - clippingIndex +
clippingIndex*theIntegral)]];
sampledMG = Append[sampledMG, N[Exp[-(v^2 varTot)/2]]];
vAxis = Append[vAxis, N[v]];
pdfAxis = Append[pdfAxis, N[i*deltaI]];
Print[" i: ",i," v: ",N[v], " M: ",
N[Exp[-(v^2 varG)/2] (1 - clippingIndex + clippingIndex*theIntegral)]];
Print[" "];
];

(* The rest of sampledM is calculated so that the final list is real-symmetric and
imag-antisymmetric *)

```

```

sampledM[{(n/2 + 1)}] = Re[sampledM[{(n/2 + 1)}]];
sampledMG[{(n/2 + 1)}] = Re[sampledMG[{(n/2 + 1)}]];

For [i= (n/2), i >= 2, i = i - 1,
  sampledM = Append[sampledM, Conjugate[sampledM[{i}]]];
  sampledMG = Append[sampledMG, Conjugate[sampledMG[{i}]]];
  vAxis = Append[vAxis, -vAxis[{i}]];
  pdfAxis = Append[pdfAxis, -pdfAxis[{i}]];
];

(* IFFT *)

Print["IFFTing..."];
pdf = N[({(2*maxV)/(2*Pi)) (1/Sqrt[n]) InverseFourier[sampledM]];
pdfG = N[({(2*maxV)/(2*Pi)) (1/Sqrt[n]) InverseFourier[sampledMG]];

(* Rearrange arrays *)

combinedPdf = {pdfAxis, Re[pdf]};
combinedPdf = Transpose[combinedPdf];
combinedPdfG = {pdfAxis, Re[pdfG]};
combinedPdfG = Transpose[combinedPdfG];

(* Save data to a file in tab-separated format *)

outfile1 = OpenWrite["DC8SteveAmpPDFModIndex6.dat"];
shortPdf=Join[Take[combinedPdf,-100], Take[combinedPdf,100]];
For [i=1, i<= Length[shortPdf], i++,
  WriteString[outfile1, CForm[shortPdf[{i,1}]], "\t",CForm[shortPdf[{i,2}]], "\n"];
]
Close["DC8SteveAmpPDFModIndex6.dat"];

outfile2 = OpenWrite["DC8GaussAmpPDFModIndex6.dat"];
shortPdf=Join[Take[combinedPdfG,-100], Take[combinedPdfG,100]];
For [i=1, i<= Length[shortPdf], i++,
  WriteString[outfile2, CForm[shortPdf[{i,1}]], "\t",CForm[shortPdf[{i,2}]], "\n"];
]
Close["DC8GaussAmpPDFModIndex6.dat"];

```

## F.6 BER vs QAM Modulation Index (Mathematica)

```

(*****
(* gam2.m *)
(* ----- *)
(*
(* This program calculates the BER vs. QAM mod index for a QAM channel
(* in a hybrid AM-VSB/QAM lightwave system.
(*
(*
(*****

(* Set some system parameters *)

AMmodIndex = 0.06; (*AM mod index per channel*)
NN=42; (*Number of channels*)
mu=N[Sqrt[(NN AMmodIndex^2)/2]]; (*Total rms modulation index*)
Resp= 0.94; (*Responsivity*)
Po= -1; (*Received optical power in dBm*)

```

```

Pr = (10^(Po/10))*0.001;          (*Received optical power in Watts*)

(* Set the symbol rate and calculate the symbol period *)
symbolRate = 4.5833 10^6;
timeTs = N[1/symbolRate];
timeT = 0.5 timeTs;

(* Calculate clipping rate and clipping index *)
fb = 337.25 10^6;                  (* Highest frequency AM channel *)
fa = 55.25 10^6;                  (* Lowest frequency AM channel *)
rate = ((fb^3 - fa^3)/(3(fb - fa)))^0.5 Exp[-1/(2 mu^2)]; (* Rate of clipping *)
clippingIndex = N[timeTs rate];

(* Specify impulsive and Gaussian noise powers *)
(* Note: The impulsive noise power was calculated using the *)
(* nonlinear distortion model in reference [38] (Alameh and *)
(* Minisian). The Gaussian noise power was obtained from Kinh *)
(* Pham's experimental data. *)
varI = N[3.093 10^-15];            (* impulsive noise power in A^2 *)
varG = N[1.834 10^-15];            (* Gaussian noise power in A^2 *)
Print["varI: ", varI, " varG: ", varG, " clippingIndex: ", clippingIndex, " rate: ",
rate];

(* QAM parameters *)
M = 64;
Pave[QAMmodIndex_] := (QAMmodIndex^2 (Resp Pr)^2)/2; (* Ave signal power *)
dminOver2[QAMmodIndex_] := N[Sqrt[Pave[QAMmodIndex] 2.333]/(Sqrt[M] - 1)]; (* Limit
for integration *)

(*****)
(* Calculating the noise probability density *)
(* ----- *)
(*
(* This section of the program determines the pdf of shot noise combined
(* with Gaussian noise by sampling the characteristic function and taking
(* the Inverse Fast Fourier Transform (IFFT).
(*
(* Variables:
(*
(* n - number of points to use in the IFFT
(* maxV - maximum value of v for sampling the characteristic function M(jv)
(* sampledM - the list of M(jv) sample points to be IFFT'd; the first half
(* of the list is made by sampling M(jv) from v=0 to v=maxV, the
(* second half is made by imposing the condition that the real
(* part of the total list must be symetric and the imaginary
(* part of the total list must be anti-symetric (for a real pdf)
(* deltaV - interval size of the M(jv) samples
(* deltaI - the corresponding interval size of the pdf samples obtained
(* from the IFFT
(*
(*****)

(* Calculate mean square of impulse area and define integral in characteristic func *)
h[t_] := Which[N[Abs[t]] <= N[timeT], 1, True, 0]; (* Paseband shot noise waveform *)

```

```

pulseEnergy = N[Integrate[h[t]^2, {t, -timeT, timeT}]]; Print["pulseEnergy:
", pulseEnergy]; (*Pulse Energy*)
Print[" "];
meanSquareA = N[(2*varI)/(rate*pulseEnergy)]; (* Mean square value of impulse area *)
c3 = N[(6/meanSquareA)^(1/3)];
integral[v_] := Which[v == 0, 1, True,
(2*c3^(3/2)*E^((2*c3^3)/(27*v^2))*(3/Pi)^(1/2)*(v^(-2))^(1/2)*
BesselK[1/6, (2*c3^3)/(27*v^2))]/9];

(* Parameters for sampling the characteristic function *)

n = 2^13;
maxV = 5 10^8;
deltaV = maxV/(n/2);
deltaI = (2 Pi)/(n deltaV);
Print["n = ", n, " deltaV = ", N[deltaV], " maxV = ", maxV ];
Print["varI: ", varI, " varG: ", varG];
Print[" "];
Print[" "];

(* Sample the characteristic function *)

sampledM = {};
vAxis = {};
pdfAxis = {};
For [i=0, i <= n/2, i++,
v = i*deltaV;
theIntegral = integral[v];
sampledM = Append[sampledM, N[Exp[-(v^2 varG)/2] (1 - clippingIndex +
clippingIndex*theIntegral)]];
vAxis = Append[vAxis, N[v]];
pdfAxis = Append[pdfAxis, N[i*deltaI]];
Print[" i: ", i, " v: ", N[v], " M: ",
N[Exp[-(v^2 varG)/2] (1 - clippingIndex + clippingIndex*theIntegral)]];
Print[" "];
];

(* The rest of sampledM is calculated so that the final list is real-symetric and
imag-antisymetric *)

sampledM[(n/2 + 1)] = Re[sampledM[(n/2 + 1)]];

For [i= (n/2), i >= 2, i = i - 1,
sampledM = Append[sampledM, Conjugate[sampledM[[i]]]];
vAxis = Append[vAxis, -vAxis[[i]]];
pdfAxis = Append[pdfAxis, -pdfAxis[[i]]];
];

(* IFFT *)

Print["IFFTing..."];
pdf = N[(2*maxV)/(2*Pi)) (1/Sqrt[n]) InverseFourier[sampledM];

(* Make matrix with x-axis and corresponding y-axis values *)

combinedPdf = {pdfAxis, Re[pdf]};
combinedPdf = Transpose[combinedPdf];
combinedPdfT = Transpose[combinedPdf];

```

```
(* Routine for calculating BER *)
```

```
BERLai[QAMmodindex_] := (
  start = Round[N[dminOver2[QAMmodindex]/deltaI]];
  stop = Length[combinedPdf]/2;
  (* find area in interval [start,stop] using trapezoidal rule *)
  tail = (deltaI/2) * Apply[Plus, {Take[combinedPdfT[[2]], {start, stop - 1}]
    + Take[combinedPdfT[[2]], {start + 1, stop}]}];
  Return[(4/Log[2,M]) (1 - 1/Sqrt[M]) tail];
);
```

```
(* Calculate BER vs. QAM mod index and save to a file *)
```

```
outfile = OpenWrite["AMmod6-Lail.dat"];
```

```
For [QAMmodIndex = 0.001, QAMmodIndex <= 0.0301, QAMmodIndex = QAMmodIndex + 0.001,
  BER = BERLai[QAMmodIndex];
  WriteString[outfile,CForm[QAMmodIndex], " \t",CForm[N[BER]], "\n"];
  Print[CForm[QAMmodIndex], " ",CForm[N[BER]]];
];
```

```
Close["AMmod6-Lail.dat"];
```

## Appendix G: Threshold Detector Design

This section contains the block diagram and detailed circuit schematics of the Threshold Detector that was designed and built at TRLabs to analyze low-pass filtered impulsive noise. As shown in the block diagram, the major blocks of the Threshold Detector are placed on two separate circuit boards: the analog board and the digital board. The major blocks include the amplitude limiter, comparator circuit, edge detector, counter controller, counter, output data multiplexer, and reset logic. The RF input, comparator output, and threshold level monitor are accessed via BNC connections on the front panel of the Threshold Detector. The digital inputs and outputs to the digital board are accessed through a 50-pin D-sub connector on the front panel and are TTL compatible. The operation of the circuits on the digital board at 50 MHz was achieved with FAST TTL ICs from National Semiconductor.

In the amplitude limiter circuit, two voltage-regulating Zener diodes are used with two high-speed Schottky diodes to limit the voltage at the comparator input to above -4.4 V and below 4.4 V. A 1  $\mu$ F capacitor is used to block the DC content of the input RF signal. In the comparator circuit, the AD588 Precision Voltage Reference is used with a 10 K $\Omega$  potentiometer dial to supply an adjustable and stable threshold voltage to the AD9696 high-speed comparator. The comparator output is buffered and sent to the output of the Threshold Detector. The comparator output is also sent to the edge detector on the digital board. The edge detector uses three D-type flip-flops in a master/slave configuration to asynchronously detect a falling edge in the inverted output signal from the comparator. When a falling edge occurs, the edge detector generates a pulse one clock period wide (20 ns) that is synchronized to the 50 MHz system clock. The pulse from the edge detector indicates to the counter controller when to start or stop the counter depending on the current state of the controller. The state diagram for the counter controller is shown below:

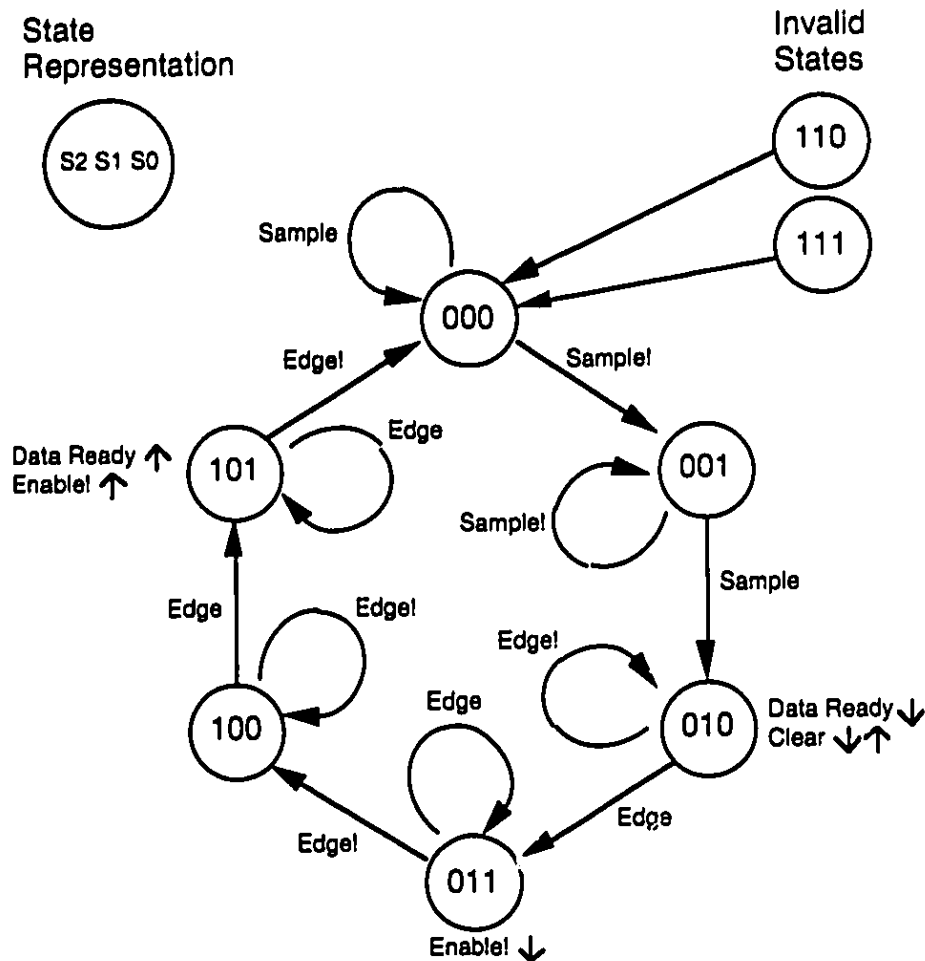
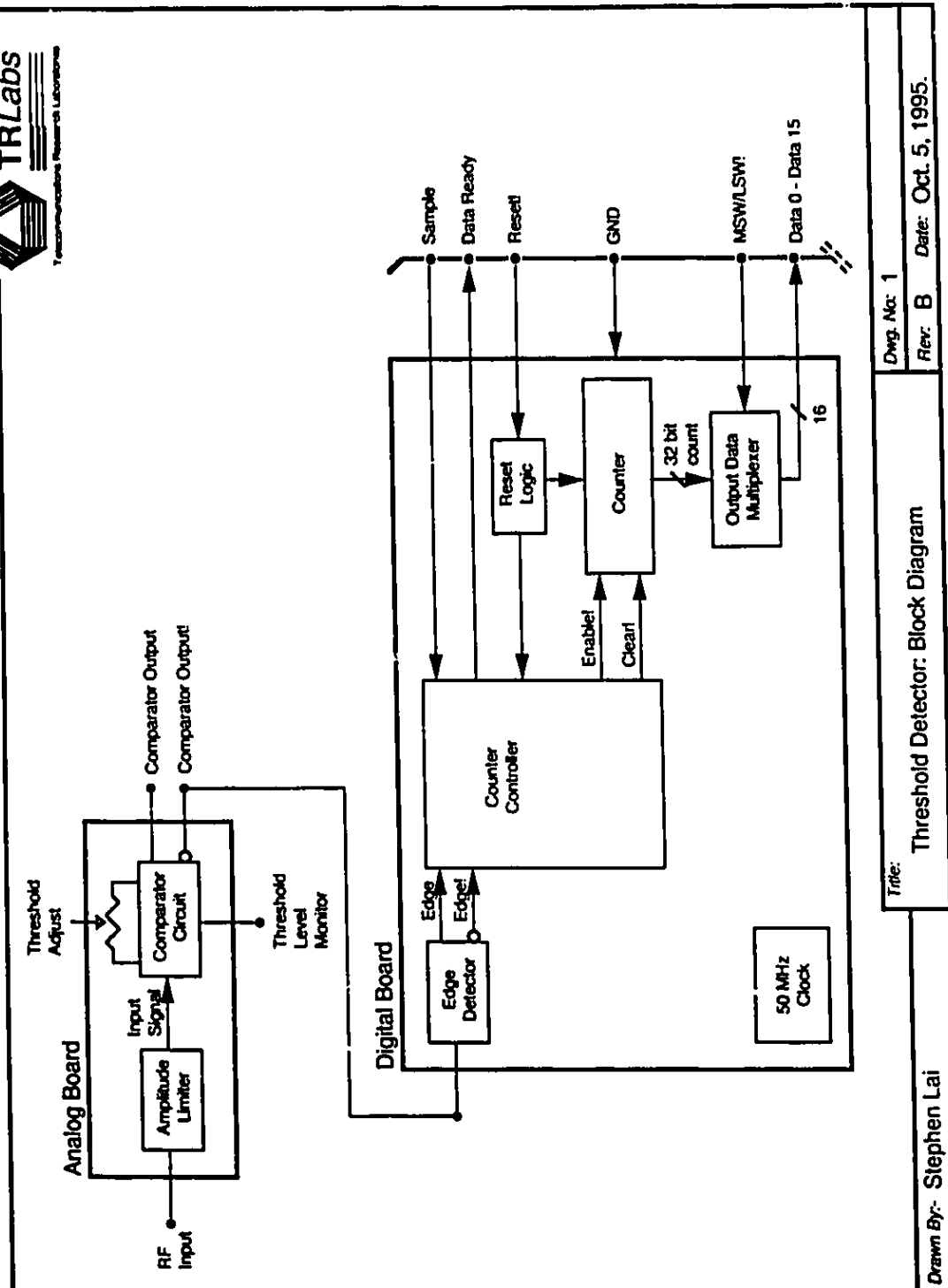


**Figure G.1: Counter Controller State Diagram**

In the state diagram, “Sample” is the TTL input used to request a time interval sample. “Edge” is the falling edge indication from the edge detector. The “Enable!” signal activates the counter and “Clear” resets the count to zero. The “Data Ready” output indicates that a time interval sample is ready. The 32-bit 50 MHz counter is implemented with four 8-bit counter ICs connected in a ripple-carry configuration. The 32-bit parallel output of the counter is accessed with the output data multiplexer which allows the either the upper or lower 16 bits of the counter to read. The MSW/LSW! input controls whether the upper or lower 16 bits are presented at the output. In the reset logic, provision is made for resetting

the digital board circuitry with either the manual reset push-button on the front panel or by setting the Reset! input to a low logic level.





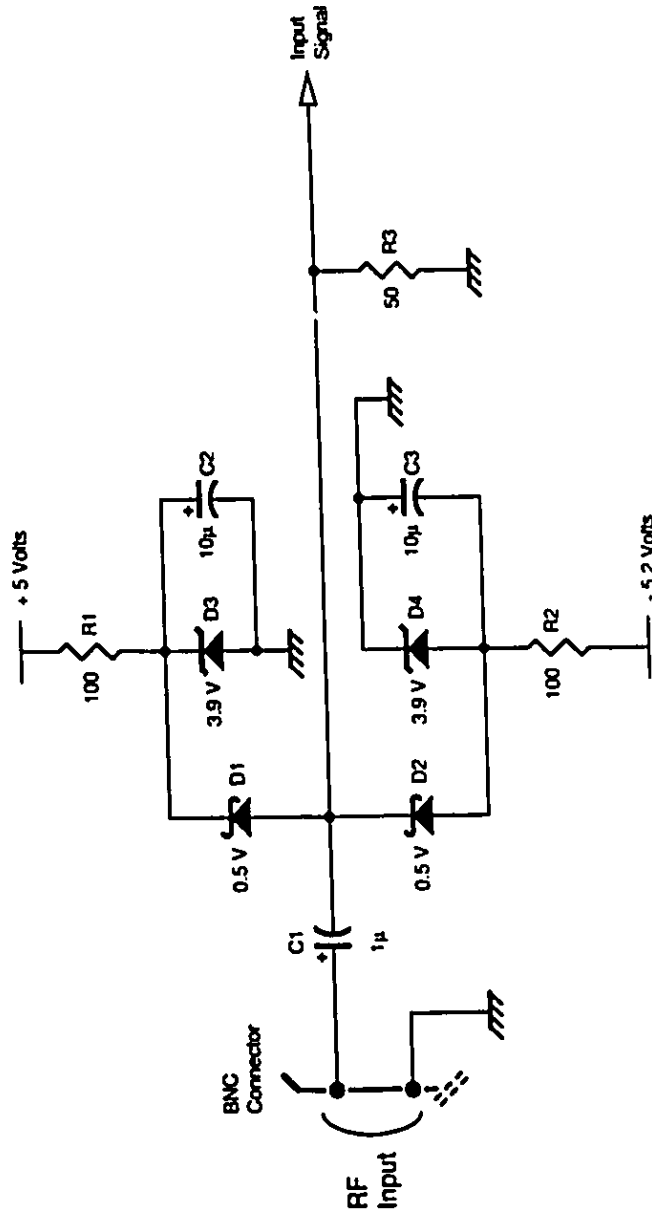
Dwg. No: 1

Rev: B Date: Oct. 5, 1995.

Title:

Threshold Detector: Block Diagram

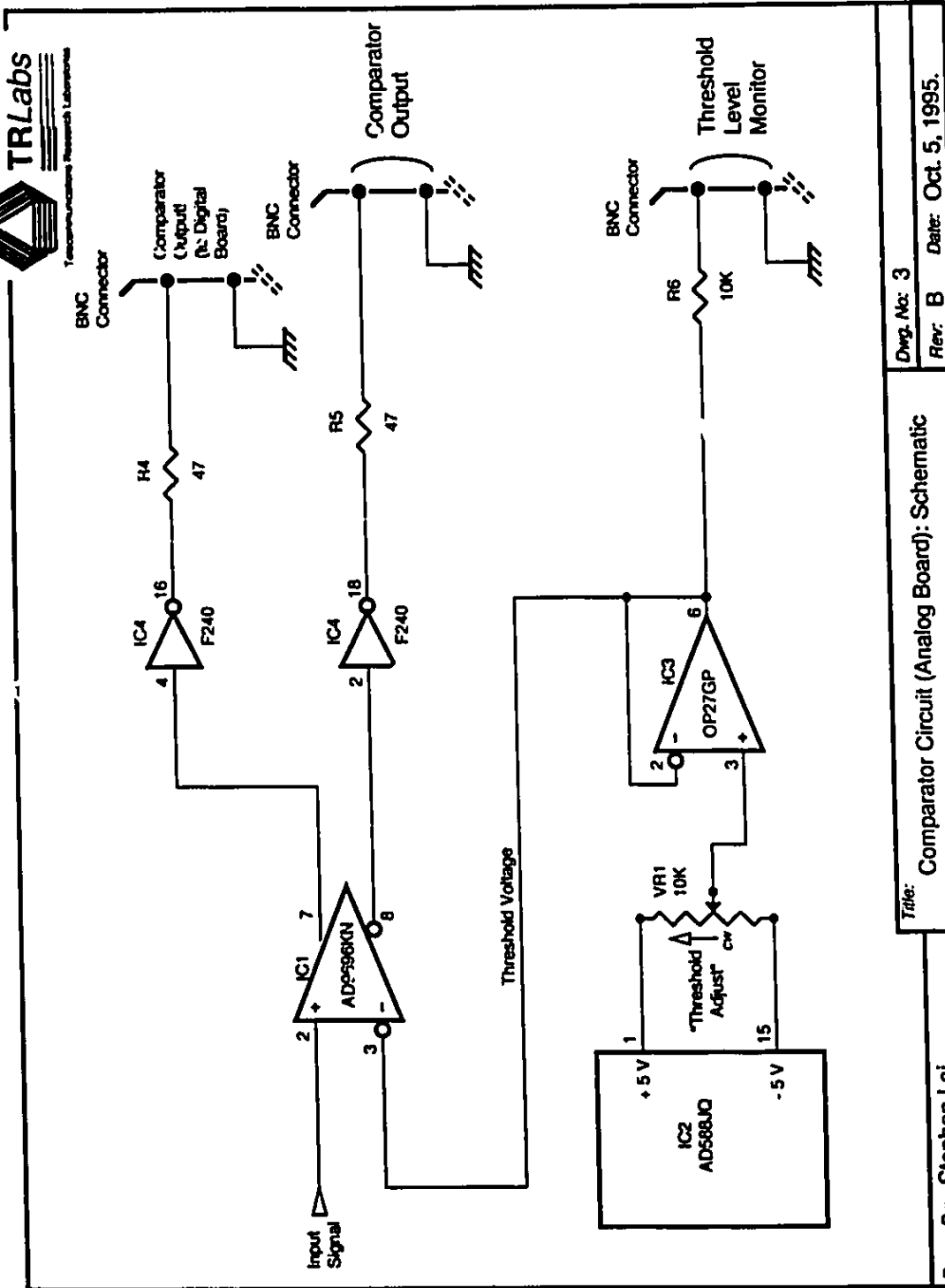
Drawn By:- Stephen Lai



Dwg. No: 2  
 Rev: B Date: Oct. 5, 1995.

Title: Amplitude Limiter (Analog Board): Schematic

Drawn By: Stephen Lai



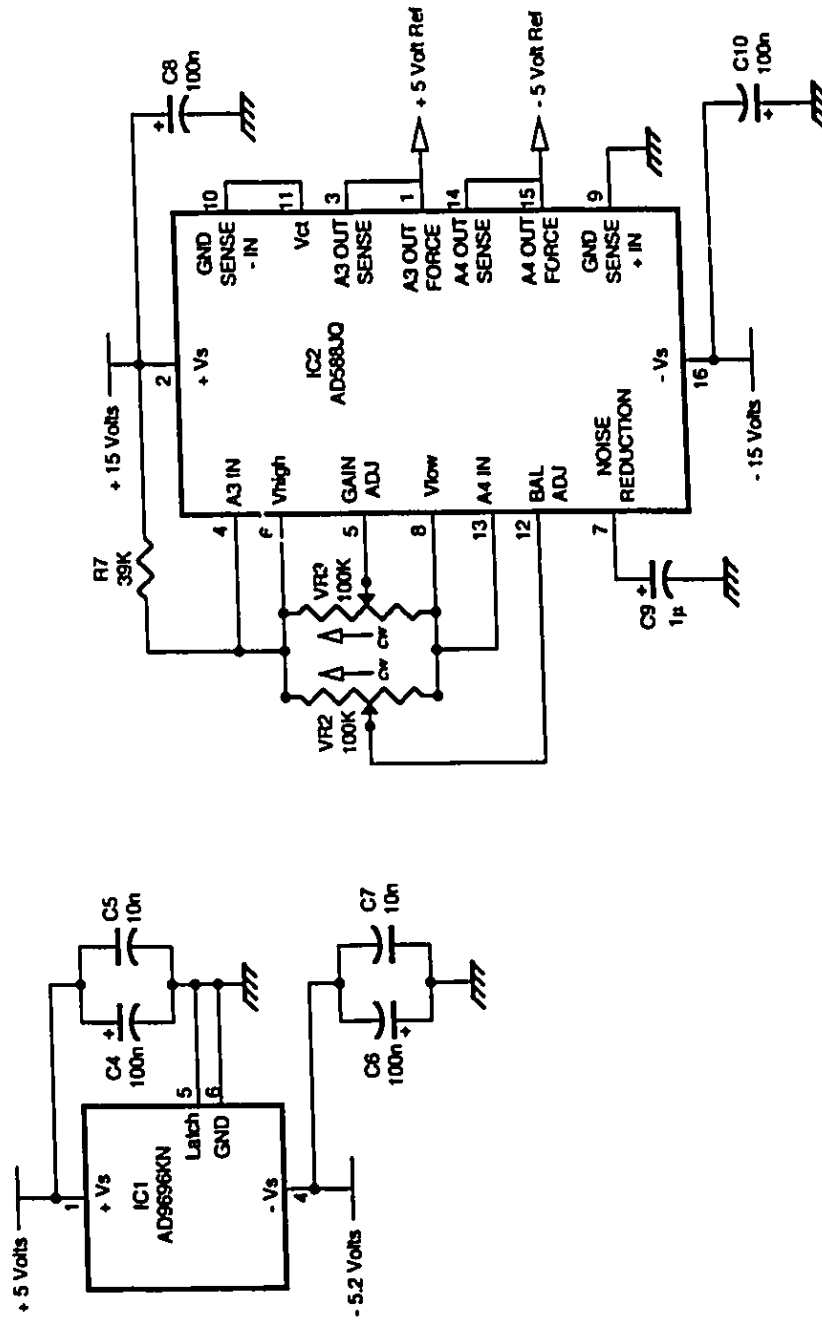
Dwg. No: 3

Rev: B

Date: Oct. 5, 1995.

Title: Comparator Circuit (Analog Board): Schematic

Drawn By: Stephen Lai



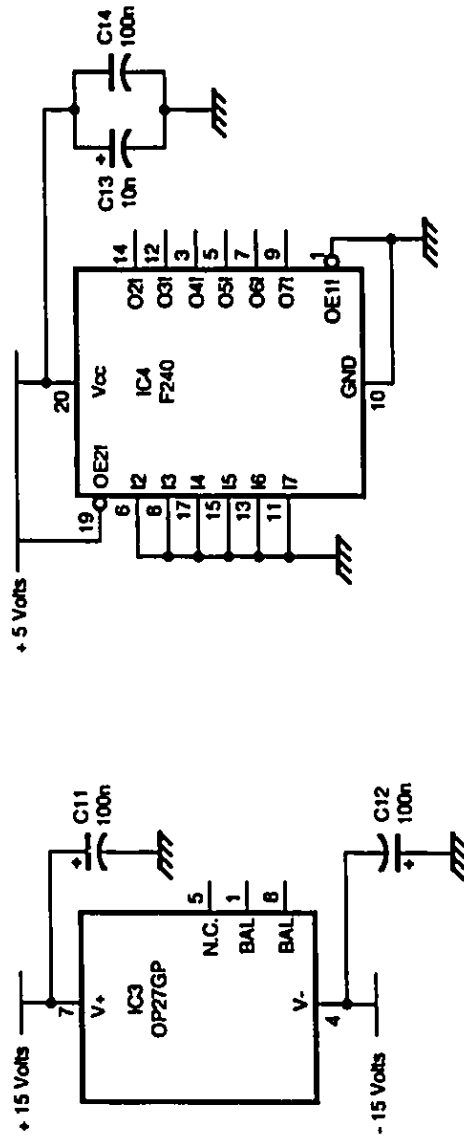
Drawn By: Stephen Lai

Title: Power and Misc 1 (Analog Board): Schematic

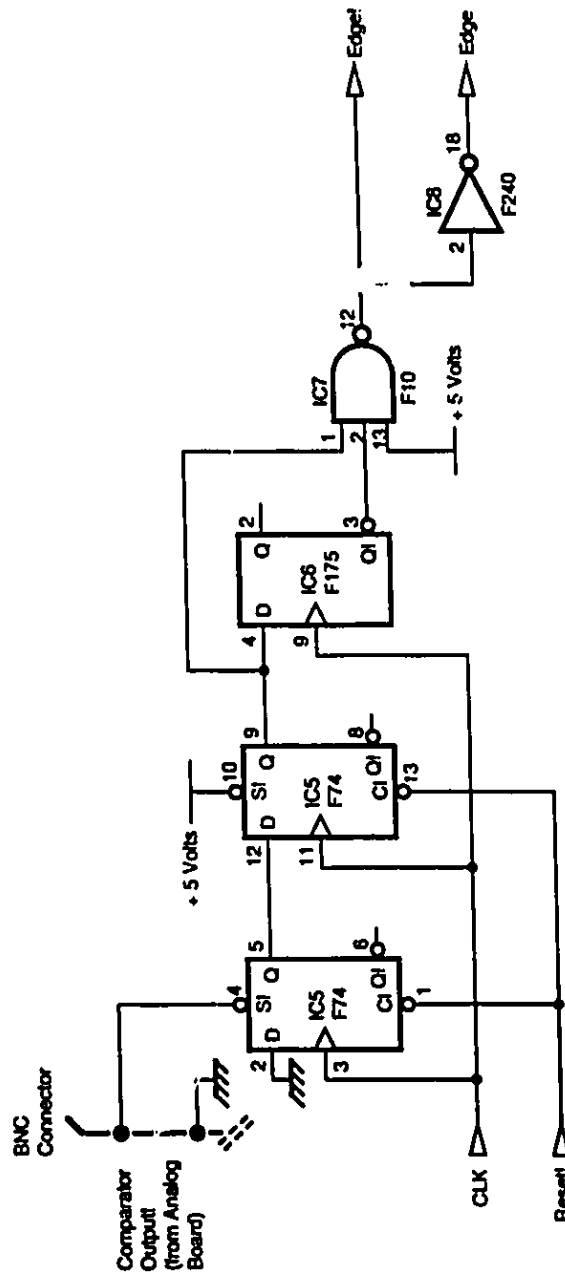
Rev: B

Date: Oct. 5, 1995.

Design No: 4



Drawn By: Stephen Lai	Title: Power and Misc 2 (Analog Board): Schematic	
	Dwg. No: 5	Rev: B
		Date: Oct. 5, 1995.

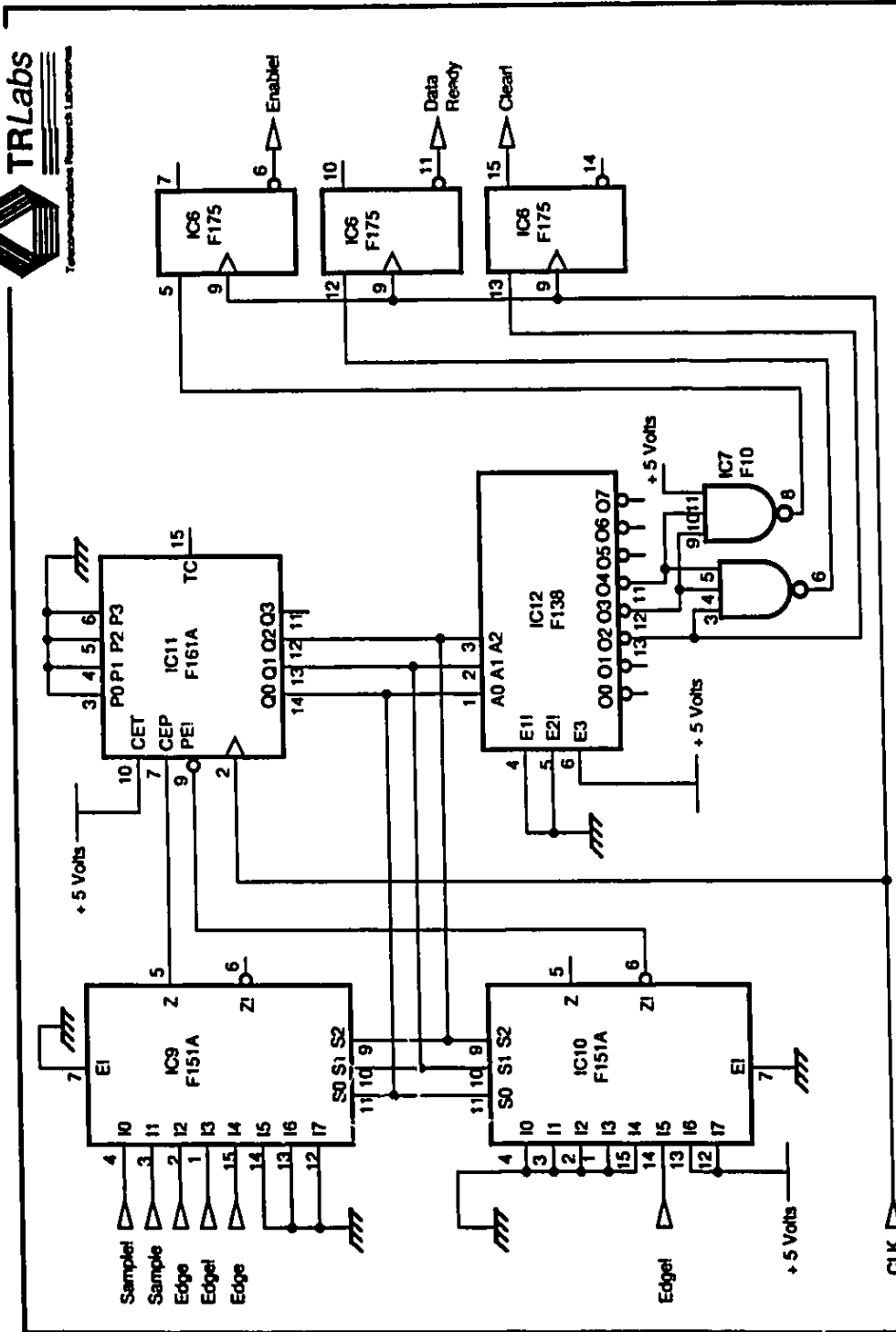


Dwg. No: 6

Rev: B Date: Oct. 5, 1995.

Title: Edge Detector (Digital Board): Schematic

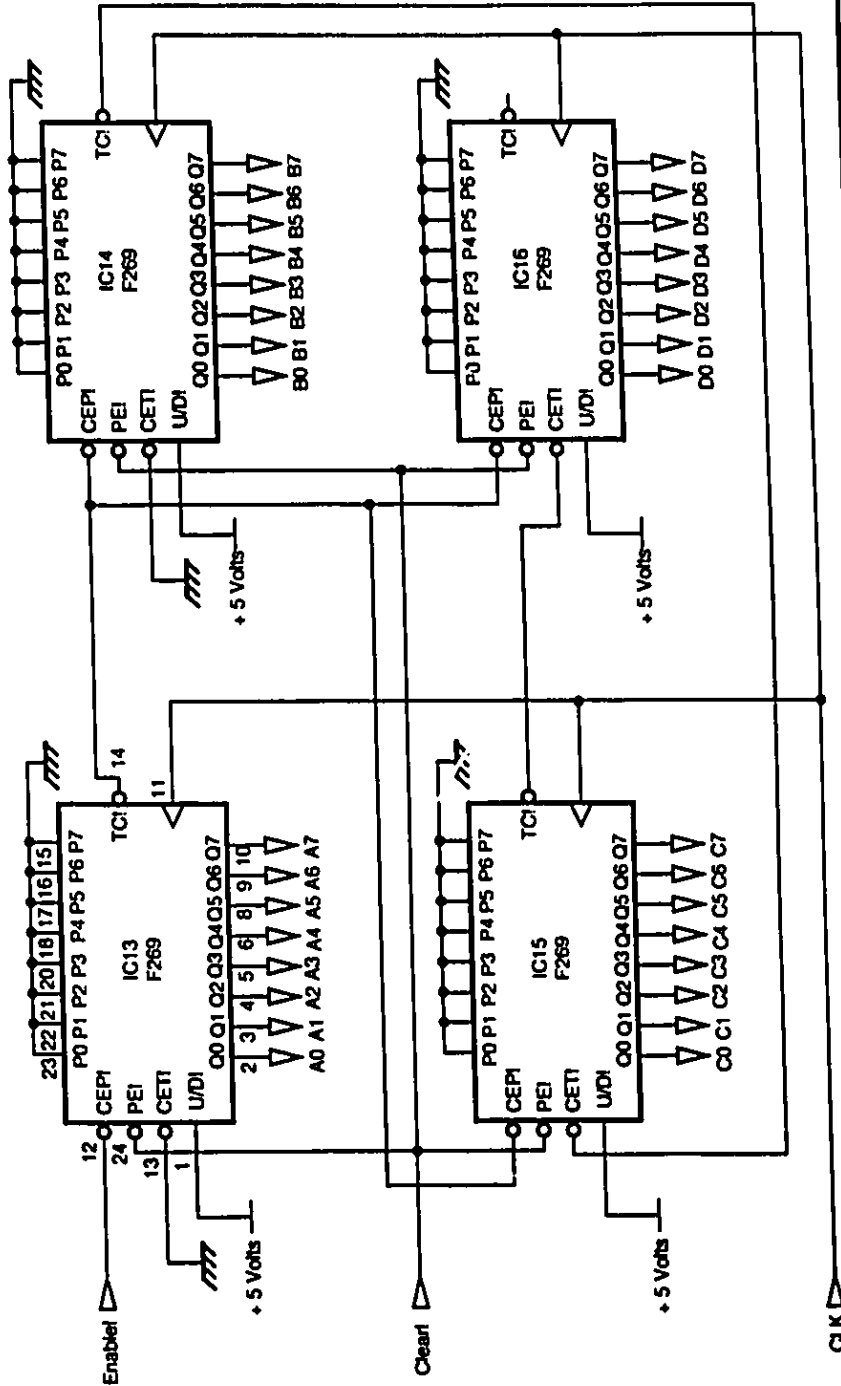
Drawn By: Stephen Lai



Dwg. No: 7  
Rev: B Date: Oct. 5, 1995.

Title: Counter Controller (Digital Board): Schematic

Drawn By: Stephen Lai

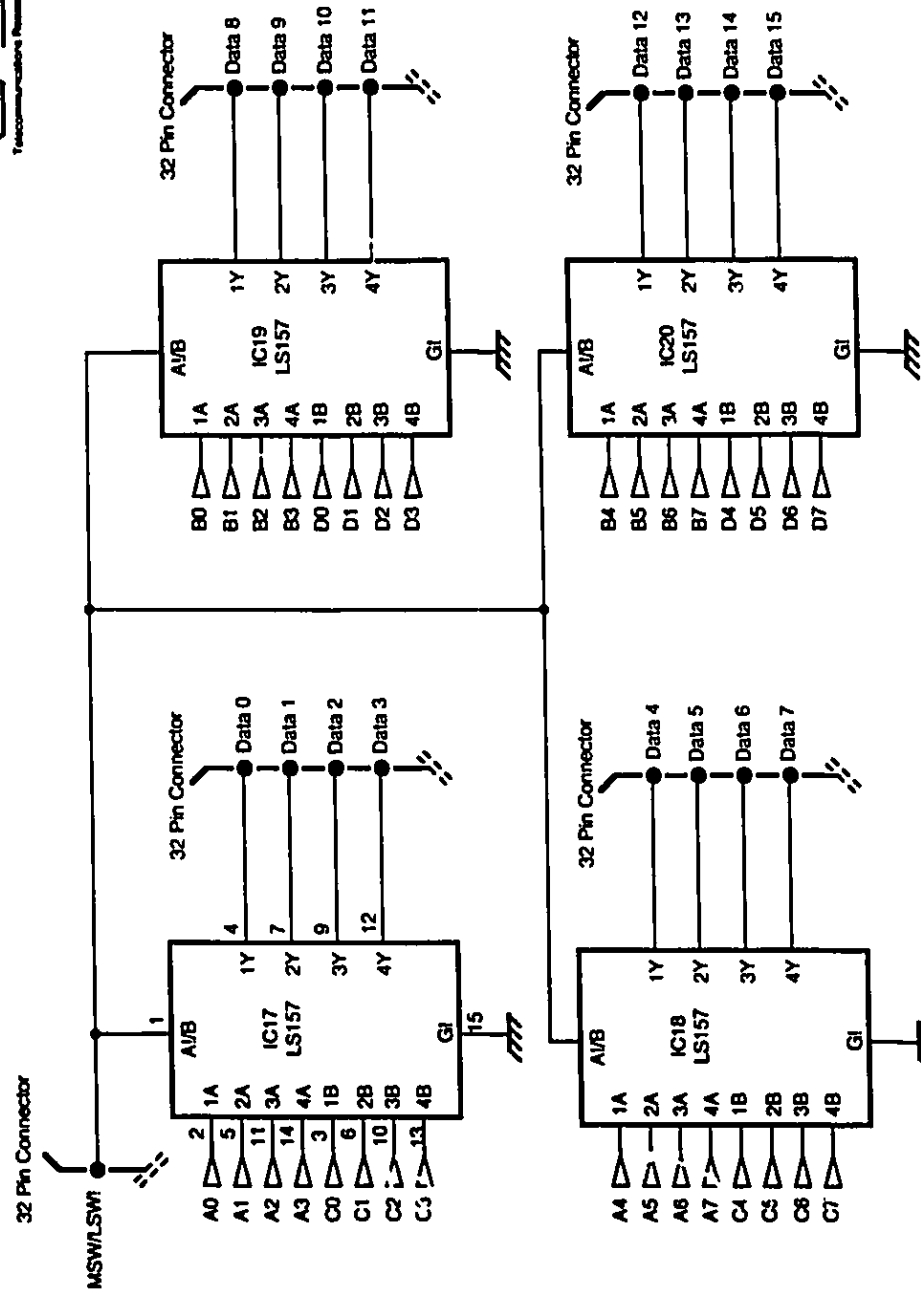


Dwg. No: 8  
Rev: B Date: Oct 5, 1995.

Title: Counter (Digital Board): Schematic

Drawn By: Stephen Lai





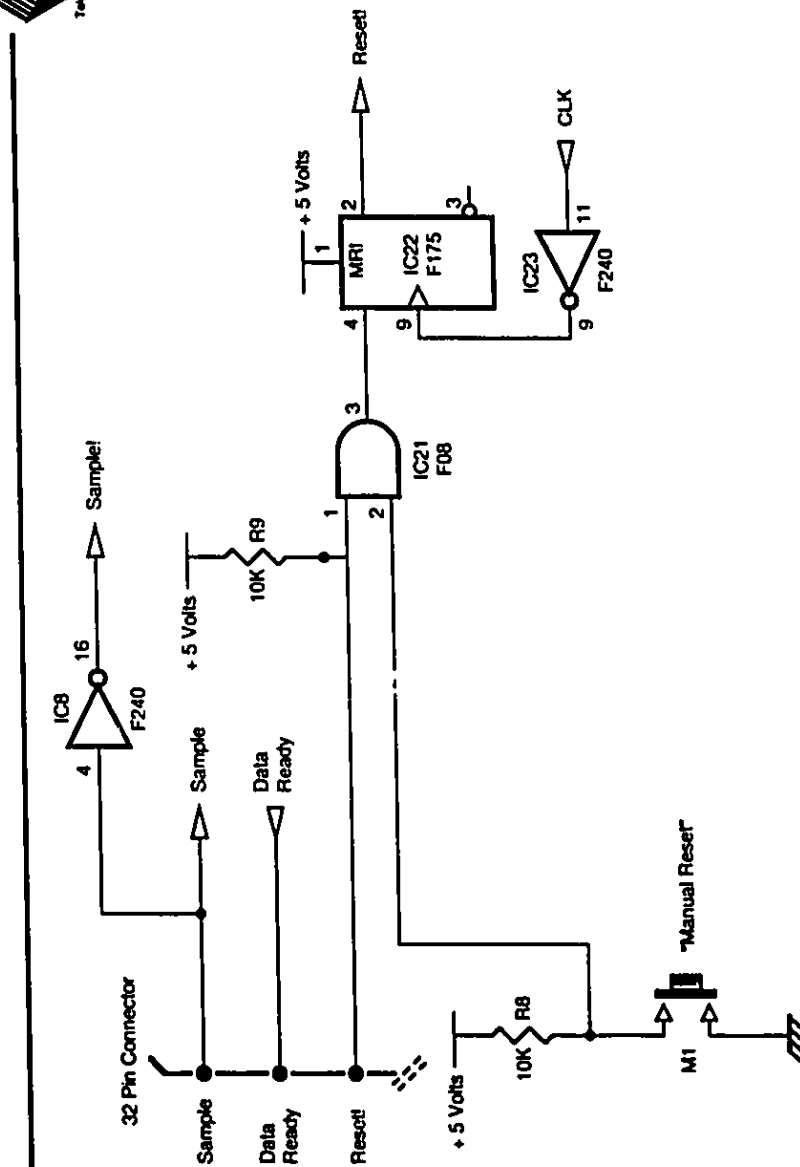
Dwg. No: 9

Rev: B

Date: Oct. 5, 1995.

Title: Output Data Multiplexer (Digital Board): Schematic

Drawn By: Stephen Lai



Dwg. No: 10

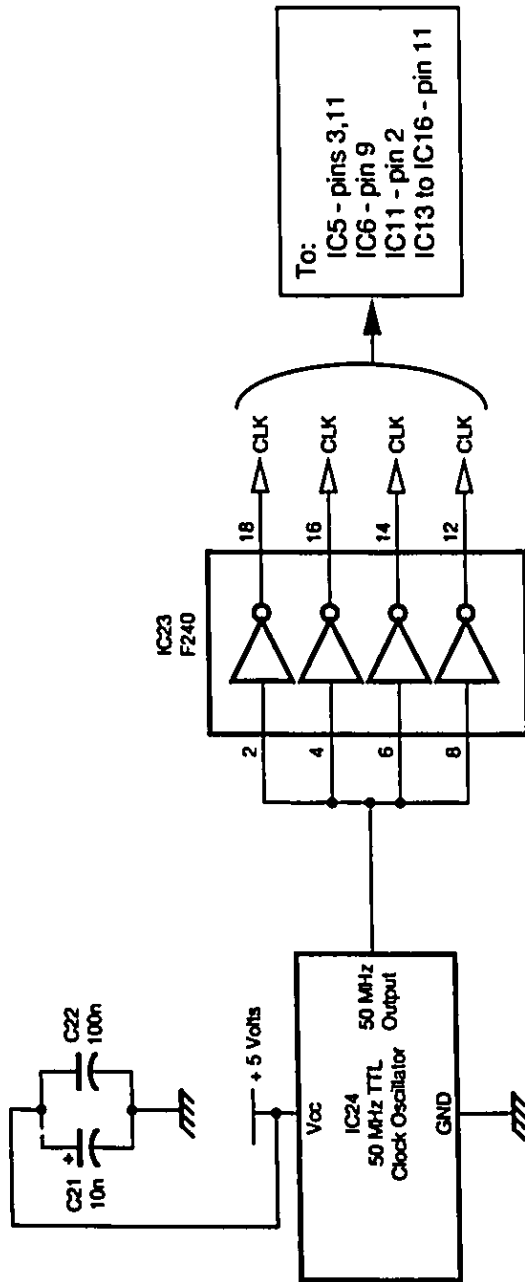
Rev. B

Date: Oct. 5, 1995.

Title:

Reset Logic and Misc (Digital Board).Schematic

Drawn By: Stephen Lai



Dwg. No: 11  
 Rev: B Date: Oct. 5, 1995.

Title: Clock Logic (Digital Board): Schematic

Drawn By: Stephen Lai

